UNIVERSITY OF CALIFORNIA SAN DIEGO

Investigating Glioblastoma Microenvironment and Cellular Interactions with 3D Bioprinted Tumor Models

A Dissertation submitted in partial satisfaction of the requirements
for the degree Doctor of Philosophy

in

Nanoengineering

by

Min Tang

Committee in charge:

Professor Shaochen Chen, Chair
Professor Nicole Steinmetz, Co-Chair
Professor Nisarg Shah
Professor Yingxiao Wang

2022

The Dissertation of Min Tang is approved, and it is acceptable in quality and form for publication on microfilm and electronically.

University of California San Diego

2022

DEDICATION

This Dissertation is dedicated to my parents

汤德平先生

何雯女士

who have given me invaluable love, support, and educational opportunities,

and my whole family, friends, mentors, and trainees,

who have accompanied me through this journey.

TABLE OF CONTENTS

LIST OF FIGURES

LIST OF TABLES

ACKNOWLEDGEMENTS

Chapter 1, in part, is adapted from the published article, “Biomaterials and 3D Bioprinting Strategies to Model Glioblastoma and the Blood–Brain Barrier”, M. Tang, J. Rich, S. Chen. *Advanced Materials*, 2020. The dissertation author was the primary investigator and author of this paper.

We thank our funding sources: CA253615 and EB021857 (to S.C.), CA197718, CA154130, CA169117, CA171652, NS087913, NS089272, and NS103434 (to J.N.R.). The authors thank Jiayi Wang for assistance on the digital illustration of tissue microenvironments.

Chapter 2, in full, is a reprint of the published article, “Rapid 3D bioprinting of glioblastoma model mimicking native biophysical heterogeneity”, Min Tang, Shashi Kant Tiwari, Kriti Agrawal, Matthew Tan, Jason Dang, Trevor Tam, Jing Tian, Xueyi Wan, Jacob Schimelman, Shangting You, Qinghui Xia, Tariq M Rana, Shaochen Chen. *Small*, 2021. The dissertation author was the primary investigator and author of this paper.

We thank members of the Chen and Rana lab for helpful discussions and advices. M.Tang, S.K.T., K.A., M.Tan, J.D. contributed to the conceptualization; M.Tang, S.K.T, T.T., J.T., and X.W. performed the experiments; M.Tang, S.T., and K.A. analyzed data; J.S. performed material synthesis and characterization; S.Y. and Q.X. contributed to the printer and software optimization. M.Tang wrote the manuscript with help from S.K.T. and K.A.. T.R. and S.C. participated in the overall experimental design, data analyses, interpretation, manuscript writing, and obtained funding for the project. We thank Hanqing Liu for helpful suggestions on RNAseq analysis. This publication includes data generated at the UC San Diego IGM Genomics Center utilizing an Illumina NovaSeq 6000 that was purchased with funding from a National Institutes of Health SIG grant (#S10 OD026929). Confocal images were taken at the UCSD School of Medicine

Microscopy Core, which is supported by a NINDS P30 grant (NS047101). This work was supported in part by grants from the National Institutes of Health (EB021857, CA253615, CA177322, DA039562, DA046171, and NS118250) and National Science Foundation (1937653). This material is based upon work supported by the National Science Foundation Graduate Research Fellowship Program under Grant No. DGE-1650112.

Chapter 3, in full, is a reprint of the published article, "Three-dimensional bioprinted glioblastoma microenvironments model cellular dependencies and immune interactions", Min Tang, Qi Xie, Ryan C Gimple, Zheng Zhong, Trevor Tam, Jing Tian, Reilly L Kidwell, Qiulian Wu, Briana C Prager, Zhixin Qiu, Aaron Yu, Zhe Zhu, Pinar Mesci, Hui Jing, Jacob Schimelman, Pengrui Wang, Derrick Lee, Michael H Lorenzini, Deobrat Dixit, Linjie Zhao, Shruti Bhargava, Tyler E Miller, Xueyi Wan, Jing Tang, Bingjie Sun, Benjamin F Cravatt, Alysson R Muotri, Shaochen Chen, Jeremy N Rich. *Cell Research*, 2020. The dissertation author was the primary investigator and author of this paper.

This work was supported by grants provided by National Institutes of Health: CA217065 (R.C.G); CA217066 (B.C.P.); DK099810 and DK114785 (B.F.K); CA197718, CA154130, CA169117, CA171652, NS087913, NS089272, NS103434 (J.N.R); CA243296 (D.L.); R01EB021857, R21AR074763, R33HD090662 (S.C.), and National Science Foundation: 1644967, 1937653 (S.C.). Dr. Muotri is supported by grants from the California Institute for Regenerative Medicine (CIRM) DISC2-09649, the National Institutes of Health through the R01MH108528, R01MH094753, R01MH109885, R01MH100175, R56MH109587, an SFARI grant #345469, and a NARSAD Independent Investigator award. We thank the UCSD School of Medicine Microscopy Core, which is supported by a NINDS P30 grant (NS047101), for use of their confocal microscopes. This material is based upon work supported by the National Science

Foundation Graduate Research Fellowship Program under Grant No. DGE-1650112 (J.S.). Any opinions, findings, and conclusions or recommendations expressed in this material are those of the author(s) and do not necessarily reflect the views of the National Science Foundation. Portions of individual panels were prepared in part using images from Servier Medical Art by Servier (https://smart.servier.com/), which is licenced under a Creative Commons Attribution 3.0 Unported License (https://creativecommons.org/licenses/by/3.0/).

Chapter 4, in part is currently being prepared for submission for publication. The dissertation author was the primary investigator and author of this paper.

Chapter 5, in part, is adapted from the published article, "Biomaterials and 3D Bioprinting Strategies to Model Glioblastoma and the Blood–Brain Barrier", M. Tang, J. Rich, S. Chen. *Advanced Materials*, 2020. The dissertation author was the primary investigator and author of this paper.

We thank our funding sources: CA253615 and EB021857 (to S.C.), CA197718, CA154130, CA169117, CA171652, NS087913, NS089272, and NS103434 (to J.N.R.). The authors thank Jiayi Wang for assistance on the digital illustration of tissue microenvironments.

VITA

2015 Bachelor of Science in Biomedical Engineering, Washington University in St. Louis

2016 Master of Science in Biomedical Engineering, Columbia University

2022 Doctor of Philosophy in Nanoengineering, University of California San Diego

PUBLICATIONS

Books

1. **M. Tang**, D. Berry, K. Miller, X. Ma and S. Chen. CHAPTER 2 Bioprinting of Biomimetic Tissue Models for Disease Modeling and Drug Screening. *3D bioprinting and nanotechnology in tissue engineering and regenerative medicine* (Academic Press, London San Diego, CA Cambridge, MA Oxford, Second edition., 2022).

Journal Publications

2. Y. Xiang, K. Miller, J. Guan, W. Kiratitanaporn, **M. Tang**, S. Chen, 3D bioprinting of complex tissues in vitro: state-of-the-art and future perspectives. *Arch Toxicol*. **96**, 691–710 (2022).

3. Z. Zhong, X. Deng, P. Wang, C. Yu, W. Kiratitanaporn, X. Wu, J. Schimelman, **M. Tang**, A. Balayan, E. Yao, J. Tian, L. Chen, K. Zhang, S. Chen, Rapid bioprinting of conjunctival stem cell micro-constructs for subconjunctival ocular injection. *Biomaterials*. **267**, 120462 (2021).

4. Z. Zhong, A. Balayan, J. Tian, Y. Xiang, H. H. Hwang, X. Wu, X. Deng, J. Schimelman, Y. Sun, C. Ma, A. Dos Santos, S. You, **M. Tang**, E. Yao, X. Shi, N. F. Steinmetz, S. X. Deng, S. Chen, Bioprinting of dual ECM scaffolds encapsulating limbal stem/progenitor cells in active and quiescent statuses. *Biofabrication*. **13** (2021).

5. Z. Xia, **M. Tang**, J. Ma, H. Zhang, R. C. Gimple, B. C. Prager, H. Tang, C. Sun, F. Liu, P. Lin, Y. Mei, R. Du, J. N. Rich, Q. Xie, Epitranscriptomic editing of the RNA N6-methyladenosine modification by dCasRx conjugated methyltransferase and demethylase. *Nucleic Acids Research*. **49**, 7361–7374 (2021).

6. **M. Tang**, S. K. Tiwari, K. Agrawal, M. Tan, J. Dang, T. Tam, J. Tian, X. Wan, J. Schimelman, S. You, Q. Xia, T. M. Rana, S. Chen, Rapid 3D Bioprinting of Glioblastoma Model Mimicking Native Biophysical Heterogeneity. *Small*, 2006050 (2021).

7. J. Guan, S. You, Y. Xiang, J. Schimelman, J. Alido, X. Ma, **M. Tang**, S. Chen, Compensating the cell-induced light scattering effect in light-based bioprinting using deep learning. *Biofabrication*. **14** (2021).

8. J. Zhou, H. Qian, J. Zhao, **M. Tang**, Q. Wu, M. Lei, H. Luo, S. Wen, S. Chen, Z. Liu, Two-dimensional optical spatial differentiation and high-contrast imaging. *National Science Review*, nwaa176 (2020).

9. C. Yu, K. L. Miller, J. Schimelman, P. Wang, W. Zhu, X. Ma, **M. Tang**, S. You, D. Lakshmipathy, F. He, S. Chen, A sequential 3D bioprinting and orthogonal bioconjugation approach for precision tissue engineering. *Biomaterials*. **258**, 120294 (2020).

10. **M. Tang**, Q. Xie, R. C. Gimple, Z. Zhong, T. Tam, J. Tian, R. L. Kidwell, Q. Wu, B. C. Prager, Z. Qiu, A. Yu, Z. Zhu, P. Mesci, H. Jing, J. Schimelman, P. Wang, D. Lee, M. H. Lorenzini, D. Dixit, L. Zhao, S. Bhargava, T. E. Miller, X. Wan, J. Tang, B. Sun, B. F. Cravatt, A. R. Muotri, S. Chen, J. N. Rich, Three-dimensional bioprinted glioblastoma microenvironments model cellular dependencies and immune interactions. *Cell Res*, 1–21 (2020).

11. **M. Tang**, J. N. Rich, S. Chen, Biomaterials and 3D Bioprinting Strategies to Model Glioblastoma and the Blood–Brain Barrier. *Adv. Mater.*, 2004776 (2020).

12. X. Ma, S. Dewan, J. Liu, **M. Tang**, K. L. Miller, C. Yu, N. Lawrence, A. D. McCulloch, S. Chen, 3D printed micro-scale force gauge arrays to improve human cardiac tissue maturation and enable high throughput drug testing. *Acta Biomater*. **95**, 319–327 (2019).

13. X. Ma, J. Liu, W. Zhu, **M. Tang**, N. Lawrence, C. Yu, M. Gou, S. Chen, 3D bioprinting of functional tissue models for personalized drug screening and in vitro disease modeling. *Advanced Drug Delivery Reviews*. **132**, 235–251 (2018).

14. Z. Chen, **M. Tang**, D. Huang, W. Jiang, M. Li, H. Ji, J. Park, B. Xu, L. J. Atchison, G. A. Truskey, K. W. Leong, Real-time observation of leukocyte–endothelium interactions in tissue-engineered blood vessel. *Lab Chip*. **18**, 2047–2054 (2018).

15. **M. Tang**, Y. Zhou, R. Zhang, L. V. Wang, Noninvasive photoacoustic microscopy of methemoglobin *in vivo*. *J. Biomed. Opt*. **20**, 036007 (2015).

ABSTRACT OF THE DISSERTATION

Investigating Glioblastoma Microenvironment and Cellular Interactions with 3D Bioprinted Tumor Models

by

Min Tang

Doctor of Philosophy in Nanoengineering

University of California San Diego, 2022

Professor Shaochen Chen, Chair
Professor Nicole Steinmetz, Co-Chair

Glioblastoma (GBM) is the most common and fatal adult primary brain cancer. Maximal safe surgical resection followed by concurrent chemotherapy and radiotherapy results in a five-year survival rate less than 7% for patients afflicted with GBM, and therapeutic advances to treat glioblastoma remain stagnant. *In vivo*, complex cell-matrix and cellular interactions among tumor cells, stromal cells, and the extracellular matrix (ECM) lead to a dynamic and heterogeneous GBM tumor ecosystem, characterized by significant immune infiltration and immunosuppression. Traditional model systems such as 2D cell culture or animal models either lack sufficient complexity to mimic the pathophysiological GBM microenvironment or face challenges with engraftment, lack of normal immune interactions, and low throughput nature of animal

experiments. The discrepancies between drug evaluation results from pre-clinical models and actual clinical outcomes have also led to failure of many compounds in clinical trials.

In this dissertation, ECM and cellular aspects of GBM are independently investigated using 3D models generated with a light-based 3D bioprinting technique and brain tumor-relevant biomaterials, revealing important criteria for fabricating biomimetic GBM models. The models serve as scalable and physiologic platforms to interrogate the role of different factors, including matrix properties and cellular crosstalk, in various tumor progression events, such as tumor migration, functional dependencies, drug responses, and immunologic interactions within a species-matched condition. In addition, a computational method based on machine learning algorithms is developed to predict drug sensitivity of monocyte or microglia infiltrated GBM tissues to small molecule probes and reveal features that contribute to the outcome of the prediction. The integration of computational tool with more clinically relevant tumor models could be a promising solution to investigate the disease mechanisms and accelerate the drug development for GBM.

CHAPTER 1 Introduction

1.1 Background and Motivations

Glioblastoma (GBM) is the most common and aggressive adult primary brain cancer, accounting for 14.6% of all malignant central nervous system (CNS) tumors.[1] The five-year relative survival is 6.8% for patients in the United States, ranking lowest among all primary malignant CNS tumors.[1] Despite tremendous efforts in the past decades, little advance in the outcome for patients afflicted with GBM has been achieved. Standard-of-care GBM treatment involves maximally safe surgical resection, followed by concurrent chemoradiation with the oral methylator, temozolomide (TMZ), and then adjuvant TMZ. Complete surgical removal using hemicraniectomies was previously attempted but failed to achieve cure due to the diffuse invasion of tumor cells into the brain and the necessity to preserve essential brain function. GBM cells invade into the brain parenchyma in different modes, including as single cells, and act as reservoirs for recurrence. Extensive molecular profiling of GBM has identified distinct transcriptional subtypes that reflect heterogenous tumor genetics and epigenetics. Complex cellular and cell-matrix interactions among tumor cells, stromal cells, and the extracellular matrix (ECM) within the TME result in a dynamic and immunosuppressive GBM tumor ecosystem highly resistant to existing treatments. Universal relapse, high intratumoral and intertumoral heterogeneity, and resistance of recurrent GBM to therapies lead to poor prognoses and a dismal median survival time of patients less than 70 years old of 14.6 months.[2] The bottleneck in current GBM therapeutic development indicates limitations of current modeling modalities and supports development of more reliable model systems to help elucidate the pathways involved in different subtypes and provide more informative preclinical drug evaluations that will accelerate the drug development process.

GBM modeling requires the recapitulation of not only the dynamic, multi-component TME, but also the brain's unique anatomical and biochemical features that play critical roles in GBM pathogenesis and treatment response. Traditional modeling modalities have limited capacity to reconstruct important aspects of the GBM, such as relevant tumor-stromal interactions and TME heterogeneity related to tumor development, drug penetration, and treatment efficacy. Patient-derived xenografts (PDXs) retain many transcriptomic and genomic signatures of the donor tumors and provide ECM-rich microenvironments conducive to cell growth.[3] However, generating PDX requires the use of immunodeficient animals, which prevents investigation of relevant immune responses, such as the interactions between GBM cells and tumor-associated microglia and macrophages (TAMs). TAMs account for about one-third of the tumor mass in recurrent GBM and modulate various cancer activities such as tumor cell migration, invasion, and drug resistance.[3,4] Development of PDXs is also time-consuming and relatively low throughput, requiring a timespan not ideal for diseases like GBM that have fast progression. *In vitro* models that recapitulate native tumor-stromal interactions and cell-ECM interactions of GBM in a reproducible, efficient, and high-throughput manner may serve as better alternatives to *in vivo* models. 2D cell cultures are the most common and accessible *in vitro* modeling methods, but they lack the proper dimensionality and the cell-ECM interactions critical to GBM development. 2D culture conditions also induce irreversible alterations to gene expression, cell morphologies, and cellular activities of the cultured cells, reducing their similarity to primary tumors.[3] Organoids are 3D *in vitro* models with improved biomimicry compared to other *in vitro* culture methods. GBM organoids better maintain the cellular heterogeneity and the gene expression of primary tumors, and the tumor cells within organoids display enhanced hypoxic state and stemness compared to their counterparts 2D cultures.[5,6] Organoid fabrication protocols have been developed, but the

variability among organoids and the limited control of cellular organization within organoids due to the self-assembly process limit their broader applications.[5–7] Traditional *in vitro* modeling methods are still limited in terms of recapitulating the highly heterogeneous GBM microenvironment or physiologically relevant BBB barrier properties in a reproducible and scalable fashion.

Advanced biofabrication technologies can produce customized 3D tissue models with good flexibility, reproducibility, and scalability, addressing many limitations of other modeling modalities. Biofabrication technologies can be categorized based on whether cellular components are seeded onto constructs after device fabrication or encapsulated in the biomaterials during the fabrication process. The cell-encapsulating approach enables better control of the number and the position of deposited cells and molecules than the cell-seeding approach, resulting in better reproducibility.[8,9] Cells encapsulated in hydrogels encounter ECM cues from all directions, resembling their physiologic states, while seeded cells receive ECM cues mainly from the side in contact with hydrogels. Many technologies are capable of fabricating acellular scaffolds or devices with high resolution and throughput, such as electrospinning, fused deposition modelling, and selective laser sintering, among others, but are not commonly used for cell encapsulation purposes.[10] 3D Bioprinting has emerged to advance the field of cancer and tissue modeling due to its ability to encapsulate cells in biomaterials with good viability and to precisely control tissue architecture and matrix properties.[8,11,12] 3D bioprinting enables creation of reproducible and personalized models, making it especially suitable for modeling diseases like GBM that have high intratumoral and interpatient heterogeneity.[13] Applications of bioprinting technology are not limited to living tissues, but also acellular scaffolds, microfluidic devices, and implantable constructs.

1.2 3D Bioprinting Strategies

3D bioprinting is an additive manufacturing technology capable of fabricating user-defined 3D objects based on computer-aided design (CAD) models. CAD models can be reconstructed from clinical images, such as magnetic resonance imaging (MRI) scans or computed tomography (CT) scans or designed with CAD software to present specific geometries for individual applications. 3D models are sectioned into a series of 2D cross-sectional slices with predetermined layer thickness to be implemented by the bioprinters. The 3D bioprinting process generates well-defined structures in all three dimensions, and its high resolution, reproducibility, flexibility, and customizability, make it a powerful tool for a wide range of biological applications. For successful modeling of biological samples, these strategies must permit good cell viability and allow tissues to develop functionality after printing.[14] Biomimicry of bioprinted models requires the use of property-matching biomaterials and the incorporation of relevant cell types and other molecules. The major bioprinting methods include inkjet-based, extrusion-based, and light-assisted bioprinting processes.[8,15,16] Advantages, limitations, and important features of the bioprinting methods are summarized in **Table 1.1**. Regardless of the type of bioprinting methods and biomaterials, successful construction of cell-encapsulated tissues and disease models, biological platforms for screening or delivery of drugs, and acellular scaffolds have been realized.[8,17]

Table 1.1 3D bioprinting strategies.

Type	**Inkjet-based**	**Extrusion-based**	**Light-assisted**	**Light-assisted**	**Light-assisted**
Subtype	Thermal, piezoelectric, electrostatic	Pneumatic, mechanical (piston-driven, screw-driven)	Scanning-based (LAB, TPP)	Projection-based (DLP)	Projection-based (volumetric)
Fabrication process	Serial: point-by-point	Serial: line-by-line	Serial: point-by-point	Parallel: layer-by-layer	Parallel: rotational
Advantages	Fast printing speed, high resolution, high throughput, low cost	Broad biomaterial selection, scale-up potential, high cell densities, low cost	Very high resolution, compatible with biomaterials in different phases	High resolution, very high speed, good interface integrity, broad biomaterial selection, scale-up potential	Concurrent printing of real 3D structures, scalable to large constructs
Limitations	Poor interface integrity, low cell densities, limited to low viscosity biomaterials	Limited interface integrity, resolution limited by nozzle diameter	High cost, limited biomaterial selection, limited scalability, low throughput	Requires photosensitive biomaterials	Limited resolution, cell density may be limited due to light scattering
Typical resolution	10 μm	100 μm (with cell), 5 μm (acellular)	1 μm	2 μm	mm scale
Bioink viscosity	Low: 3.5 to 12 mPa×s	Wide range: 30 to 6×10^7 mPa×s	Medium: 1 to 300 mPa×s	-	High viscosity fluids: 90,000 mPa×s, or solids
Cell density	Low :10^6 cells/ml	High	High: 10^8 cells/ml	High	-
Print speed	Fast	Medium	Medium	Fast	Fast
References	[8,16,18]	[8,16,19]	[8,16,20]	[11,21]	[22]

1.2.1 Inkjet-Based 3D Bioprinting

Inkjet-based bioprinting forms 3D constructs by depositing volume-controlled droplets of bioinks from a nozzle. Inkjet bioprinting uses thermal, piezoelectric, or electrostatic mechanisms to deposit droplets onto receiving substrates (**Figure 1.1a**).[23] In thermal inkjet bioprinting, air bubbles generated by localized heating eject droplets from the nozzle. Instant heating does not

substantially impact cell viability. Piezoelectric and electrostatic approaches utilize the pressure generated from a piezoelectric actuator or the deflection of a pressure plate, respectively, to eject droplets.[23] Inkjet bioprinting offers simplicity, low cost, fast printing speed, and high resolution without sacrificing cell viability.[24] However, the cell density needs to be kept below 10^6 cells ml^{-1} for this printing modality to mitigate the shear stress that may reduce cell viability during dispensing.[19] Striking a balance between target resolution, material viscosity, nozzle size, and dispensing speed is critical for this printing method. Using nozzles with a smaller diameter can lead to a better resolution, but also increases the possibility of clogging if the material viscosity is not appropriate. Biomaterials with low viscosity, below 12 mPa-s, are compatible with inkjet printing.[8] Using inkjet bioprinting, a wide range of biological applications has been demonstrated, including cancer models,[25] stem cell research,[14] tissue engineering,[26] single-cell studies,[27] cell array patterning,[28] and controlled release of molecules.[29] Inkjet bioprinting can also achieve high throughput by inclusion of multiple nozzles, making it desirable for screening applications.[30,31]

1.2.2 Extrusion-Based 3D Bioprinting

Extrusion-based bioprinting relies on a continuous deposition of material filaments through a nozzle. The continuous process enables it to generate constructs with an overall better interface integrity compared to inkjet bioprinting. Two main dispensing mechanisms of the extrusion-based bioprinting are pneumatic-based and mechanical-based; the latter includes piston-driven and screw-driven methods (Figure 1.1b).[8,19] During printing, either the stage or the bioink-filled dispensing nozzle is motorized to create 3D structures in a layer-by-layer fashion. Pneumatic dispensing is directly controlled by changes in the pressure, making it highly flexible; meanwhile, the delay in pressure change can reduce its precision in spatial control of deposited bioinks. The mechanical dispensing approach is generally better in spatial control due to the real-time impact

on the material flow, while the screw-driven system is especially suitable for highly viscous materials. Versatility of extrusion-based bioprinting makes it compatible with a broad selection of

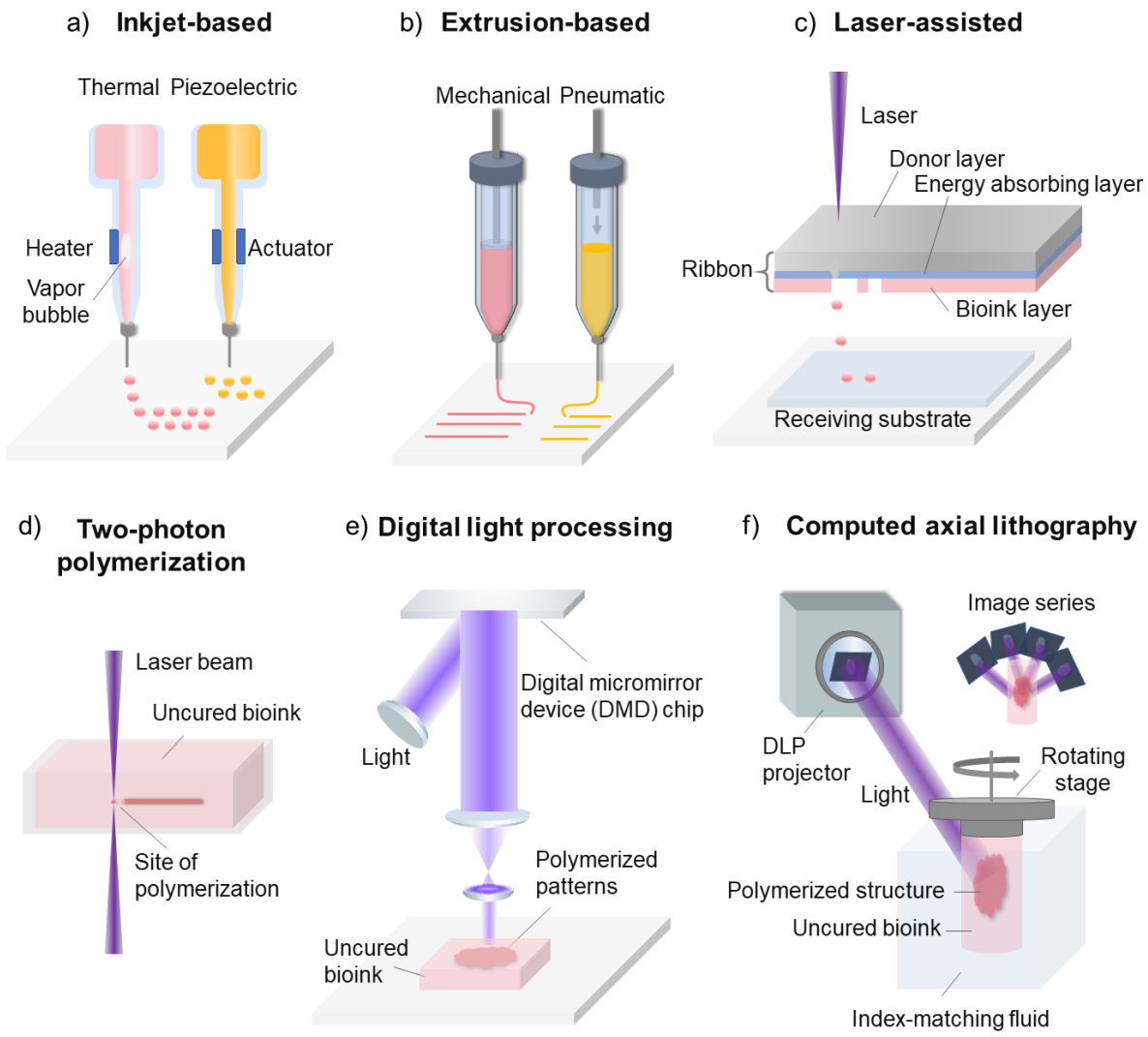

Figure 1.1 Schematic illustrations of common 3D bioprinting strategies.

biomaterials, with viscosity ranging from 30 mPa-s to 6×10^7 mPa-s. This printing modality also allows encapsulation of cells at a relatively high density, or even in the form of spheroids.[32,33] Despite the shear stress that occurs within the nozzle, extrusion-based bioprinting methods permit favorable cell viability in printed constructs.[8] Resolution of extrusion-based bioprinting is limited by a few factors, including nozzle diameter, gelation kinetics, and properties and composition of

bioinks. While high resolution of 5 μm can be achieved for acellular scaffolds, [34] cell encapsulated samples often have compromised resolution, generally over 100 μm, [35] as a tradeoff to scale-up potential and high encapsulation capacity.[8,9] Nevertheless, extrusion-based bioprinting is the most widely used bioprinting strategy for tissue engineering applications, given its ability to generate samples with physiologically relevant dimension, mechanical properties, and cell density.[17,18]

1.2.3 Light-Assisted 3D Bioprinting

Light-assisted bioprinting uses photon energy to induce photo-polymerization of bioinks to form 3D structures. Light-assisted strategies have high resolution and precise control of the architectures in all three dimensions. Without the high sheer pressures that occur in inkjet or extrusion bioprinting, higher cell viabilities can be achieved, even for sensitive cell types, including stem cells, using light assisted bioprinting approaches. Lght-assisted bioprinting can be categorized based on fabrication processes: scanning-based and projection-based. Scanning-based strategies usually require serial movement along all three axes. First, 2D features on one layer are formed through scanning of the laser beam within the bioinks or on a donor film. The laser beam then moves along the third axis, usually the z-axis, to build up a 3D structure. Projection-based bioprinting polymerizes an entire layer at a time. Features on one plane are formed with a single projection of patterned light, so the motor movement is often only necessary along the third axis during printing. Thus, projection-based strategies generally render higher throughput and faster printing speed than scanning-based strategies.[21] Commonly used light-assisted approaches for biological applications include: (1) scanning-based strategies, such as the laser-assisted bioprinting (LAB) and the two-photon polymerization (TPP)-based bioprinting; and (2) projection-based strategies, mainly digital light processing (DLP)-based bioprinting.[21,22,36–39]

A laser-assisted bioprinter is composed of a pulsed laser source, a receiving substrate, and a ribbon consisting of a bioink layer and a metal laser-absorbing layer usually made of gold or titanium (Figure 1.1c).[36] During the printing process, the laser pulse induces vapor bubbles on the donor layer and, in turn, ejects droplets of bioink onto the receiving substrate parallel to the ribbon. Micron-scale structures with high cell density have been printed, and a variety of materials is compatible with this strategy.[36,37] TPP is a laser-based direct-writing strategy that uses an ultrafast laser beam (e.g. femtosecond pulse) to trace and polymerize the cross-sectional features of 3D structures layer-by-layer. TPP polymerizes bioinks by the simultaneous absorption of two photons from a near-infrared femtosecond pulsed laser (Figure 1.1d). The resolution of TPP is not limited by the diffraction limit of the light source, so submicron scale features can be achieved.[40] Fine features of 1 μm or smaller have been printed with Poly(ethylene glycol) diacrylate (PEGDA) using TPP.[38] The relatively high resolution makes it suitable for fine patterning of biomaterials and single cell studies, with the trade-off of a slower bioprinting speed and limitation in scalability. DLP bioprinting is a rapid projection-based stereolithography, which can fabricate millimeter- or centimeter-scale constructs within seconds to minutes.[21] DLP printers are usually equipped with a digital micromirror device (DMD) chip, a motorized stage or bioprinting probe, a set of optical paths, and a computer to synchronize the movement of the stage or the probe to corresponding patterns (Figure 1.1e). The DMD chip consists of millions of micromirrors that can be independently switched on or off to display the user-defined patterns with micron-scale features. Photocurable bioinks are polymerized only at the positions where light is projected from the DMD chip, permitting a highly defined architecture with a resolution of 2 μm.[11] Functional tissue constructs integrating multiple cell types and various ECM materials have been produced with this bioprinting strategy. High cell viability has been achieved, including stem cell-derived cells.[12,41]

DLP bioprinting allows precise control over material properties, such as the elastic modulus and the amount of biochemical cues, which are important aspects for biological studies.[42] Many biomaterials have been used with DLP bioprinting, including HA, gelatin, decellularized ECM, silk fibroin, poly(ethylene glycol) (PEG), PEGDA, and polyurethane (PU), whereas some require modifications to obtain photosensitivity.[11,12,43,44] Broad biological applications of DLP include controlled release of growth factors,[45] nerve regeneration,[46] high throughput drug testing,[41] and tissue and disease modeling.[12,41,42,47,48] A DLP-based volumetric 3D bioprinting strategy, named computed axial lithography (CAL), enables fabrication of an entire 3D structure through one complete rotation of bioinks with synchronized pattern projections (Figure 1.1f).[22] The strategy relies on the back-projection algorism of the CT reconstruction. This implementation enables improved geometric flexibility than prior attempts using field interference, allowing it to print complex non-symmetric 3D structures. Materials of high viscosity up to 90,000 mPa-s were used to avoid the necessity of supporting materials. This strategy offers many distinct advantages, such as the ability to print around an existing object and the scalability such that a centimeter-scale structure can be fabricated within a minute.

1.3 GBM microenvironments

Hierarchical information of native tissues is provided in this section: the building block of native tissues, i.e. the ECM and cellular components; the assembly and organization of the basic building blocks; and the collective biophysical or biochemical properties of the microenvironment from assembly.

1.3.1 ECM compositions and properties

ECM modulates numerous brain functions and GBM initiation, progression, and invasion. ECM provides structural support to tissues, physically interacts with cells and other ECM components, and transduces signals upon binding through integrins and cell surface receptors.

Table 1.2 Major ECMs in GBM and brain parenchyma.

ECM	Class	Structure	Size	Primary crosstalk	Expression in GBM	Primary functions	
HA	GAG	Linear polysaccharide with no protein core	>1,000 kDa in normal brain	Integrins, CD44, RHAMM, lectican, GHAP	Increased, low molecular weight forms present	GBM progression and invasion; structural and biochemical support to brain	[49–52]
TSP-1	MCP	Homotrimer with three type 1 repeats	420 kDa	Heparin, α5β1 integrin, HSPG, fibronectin, laminin	Decreased	GBM cell adhesion, migration, invasion; MMP inhibition; angiogenesis inhibition	[50]
TN-C	MCP	Oligomer with six monomers linked by disulfide bonds	180-250 kDa (each monomer)	Lectican, HSPG, fibronectin, α5β1/αvβ6 integrins, CAM, phosphacan	Increased	Angiogenesis; ECM stiffness; immune suppression; EMT; GBM migration	[50, 53–56]
TN-R	MCP	Present in monomeric, dimeric, or trimeric forms	160 or 180 kDa (each monomer)	Lectican, fibronectin	Decreased	Brain plasticity regulation; synaptic activity stablization	[53, 57, 58]
SPARC	MCP	Trimer	32 kDa	Collagen, vitronectin	Increased	Cell de-adhesion; tissue remodeling; angiogenesis; EMT	[50, 55, 59]
Osteopontin	MCP	Phosphorylated protein	60kDa	CD44, integrin, heparin	Increased	Angiogenesis; GSC stemness; tumor growth and invasion	[60]

Table 1.2 Major ECMs in GBM and brain parenchyma (continued).

ECM	Class	Structure	Size	Primary crosstalk	Expression in GBM	Primary functions	
Lectican	CSPG	(See subclass)	95-400 kDa	HA, TN-R, fibulin-2	(See subclass)	(See subclass)	[57, 61, 62]
	Subclass	**Structure**			**Expression in GBM**	**Primary functions**	
	Aggrecan	G1, G2, and G3 domains with a center domain for CS/KS chains			-	Brain plasticity regulation	[63]
	Versican	Two subdomains GAGα and GAGβ, and a central domain binds CS chains. Isoform V0 carries both; V1 with only GAGβ; V2 with only GAGα; V3 lacks both.			V0/V1 increase V2 decrease	Cell adhesion and migration; drug resistance	[51, 55]
	Brevican	N- and C-terminal domains and a center domain for CS chains.			Significantly increased	GBM growth and progression	[64, 65]
	Neurocan	N- and C-terminal domains and a center domain binds up to 7 CS chains.			-	Inhibition of neurite outgrowth	[63]

The brain ECM accounts for about 17% - 20% of the total brain volume,[66] and is composed of primarily HA, proteoglycans (e.g. the lectican family), and glycoproteins (e.g. tenascin proteins, secreted protein acidic and rich in cysteine (SPARC), and thrombospondin-1 (TSP-1)).[50,61,62,67,68] Brain parenchyma ECM components are present in the GBM stroma, but with distinct expression patterns. Other ECM components in the GBM stroma include vitronectin, osteopontin, and vascular ECM components due to active angiogenesis in GBM. Major ECM components in the brain parenchyma and GBM (**Table 1.2**) are dispalyed with their structural properties, crosstalk with other ECM components or cell surface receptors, expression patterns in the GBM stroma, and primary functions in regulating brain activities or GBM progression. Changes in the amount or the composition of ECM occur with many CNS diseases, but the specific interactions and how they regulate the brain microenvironment on the molecular level remain an area of active investigation.

Mechanical properties, such as the stiffness of the tissue, are associated with ECM composition and organization. Constructing 3D models will improve our understanding of ECMs in more realistic settings, enabling identification of novel mechanisms underlying specific interactions that drive neoplastic transformation, as variables can be precisely controlled and isolated *in vitro*.

1.3.1.1 Brain ECM

HA, a negatively charged glycosaminoglycan (GAG) without a protein core, is the most abundant ECM component in the brain.[50,51] Its negative charge attracts cations and leads to osmotic influx of water, which, in addition to its hydrophilicity, results in a high water retention capacity. High HA levels in the brain parenchyma and the lack of fibrillar proteins, such as type-I collagen, make the brain a very soft organ with remarkable plasticity. The normal brain parenchyma has an elastic modulus around 0.1-1 kPa.[69,70] In healthy brain, HA is usually present in its high molecular weight form, ranging from 1,000 kDa to 8,000 kDa.[52] HA binds non-covalently to other ECM components, including the lectican family proteoglycans. Proteoglycans are composed of a core protein with different GAG side chains. Lecticans are a family of chondroitin sulfate proteoglycans (CSPGs), which include versicans, aggrecans, neurocans, and brevicans. Other CNS CSPGs include phosphacan and neuroglial antigen 2.[57] Expression of neurocans and brevicans is mostly restricted to CNS, while versicans and aggrecans are more ubiquitously expressed in other parts of the body. Versicans have several isoforms; the V2 versican isoform is the predominant CSPG in the healthy adult brain. Lecticans are considered organizers of the CNS ECM because they can form ternary complexes with HA and tenascin-R (TN-R), known as the perineuronal net of the CNS. Tenascin-C (TN-C) and TN-R are two tenascin glycoproteins found in the CNS, produced by oligodendrocytes and astrocytes, respectively.[53] Tenascins belong to a family of matricellular proteins that are non-structural ECM proteins capable of modulating cell functions and cell-ECM

interactions by binding to both cell surface receptors and structural ECM components. Two other important matricellular proteins in the CNS are SPARC and TSP-1. TSP-1 binds to CD36 on endothelial cell surface to inhibit angiogenesis.[71]

1.3.1.2 GBM ECM

The unique ECM of GBM, also predominantly composed of HA, contributes to the extensive invasion of GBMs within the CNS and constrains the very rare metastatic spread outside of the CNS.[50,72,73] HA content correlates with GBM malignancy. High and low molecular weight HA are found at elevated levels in GBM stroma, with low molecular weight HA involved in angiogenesis, tumor progression, and migration.[52] HA receptors, CD44 and RHAMM, and integrins on the tumor cell surface facilitate cell adhesion to and migration along the ECM.[50,73] Binding of tumor cells to ECM regulates the cell motility and the protease production, facilitating remodeling of the local ECM. Low molecular weight HA and HA fragments are involved in immune regulation by transducing signals through the toll-like receptors (TLR), such as TLR4, on macrophages, inducing M2-like phenotypes.[74] Expression patterns of many proteoglycans are altered in the GBM stroma. Brevicans, also known as brain-enriched hyaluronic acid binding proteins, are elevated in GBM stroma and involved in GBM growth and progression.[55,64] The V2 versican isoform is downregulated in the GBM stroma, whereas V0/V1 isoforms interact with transforming growth factor-β2 (TGF-β2) to promote tumor progression.[75] Upregulated levels of TN-C and SPARC in the pericellular ECM within the GBM stroma suggest potential roles in angiogenesis. TN-C overexpressed by tumor cells is also involved in TAM activation and correlates with GBM stiffness.[54] The expression of TN-R diminishes in higher grade gliomas, but its role remains unclear.[58] TSP-1, known to be anti-angiogenic, is downregulated in the GBM stroma, consistent with the hypervascularity in the GBM TME.[50] Osteopontin is a matricellular

phosphoglycoprotein capable of promoting tumor progression and metastasis by interacting with CD44 and integrins. Overexpression of osteopontin in the GBM microenvironment induces M2 phenotypes in TAMs, maintains the stemness of GSCs, induces angiogenesis, and enhances tumor cell migration.[54,60] Fibronectin and vitronectin, which are components of the BM, are also overexpressed in GBM, reported to regulate tumor cell adhesion, cohesion, and invasion, and activate microglia.[76,77] Overall, changes in ECM composition and expression levels create positive feedback with GBM growth and invasion, resulting in fast tumor progression and poor prognosis.

The constant remodeling of ECM within the tumor stroma, the invasive edges, and the non-tumoral brain parenchyma of the GBM patient leads to detectable changes in mechanical properties of the microenvironment. Stiffness of tumor stroma ranges from 11.4kPa to 26 kPa, and the non-tumoral brain regions of GBM patient have a stiffness of 7.3±2.1 kPa, much stiffer than that of the healthy brain.[78–81]

1.3.2 Cellular compositions and functions

Cellular composition, function, and interactions with other cells in the GBM microenvironment have been extensively studied and reviewed.[82–84] Key information is provided here to introduce the essential cellular components and their roles.

The GBM TME heterogeneous cell populations (**Figure 1.2**). Major non-neoplatic stromal cells within the GBM TME include TAMs, microglia, astrocytes, neurons, mesenchymal stem cells (MSCs), and perivascular cells. In the necrotic region of GBM, up to 30-50% of the tumor mass is composed of TAMs with an M2 pro-tumor phenotype.[85] The M2 phenotype is anti-inflammatory, creating an immunosuppressive TME that promotes tumor growth. Macrophages derived from circulating monocytes are recruited to the GBM site due to compromised BBBs and perturbations in brain homeostasis, whereas microglia are CNS resident immune cells that become activated in response to tumor-derived cues.

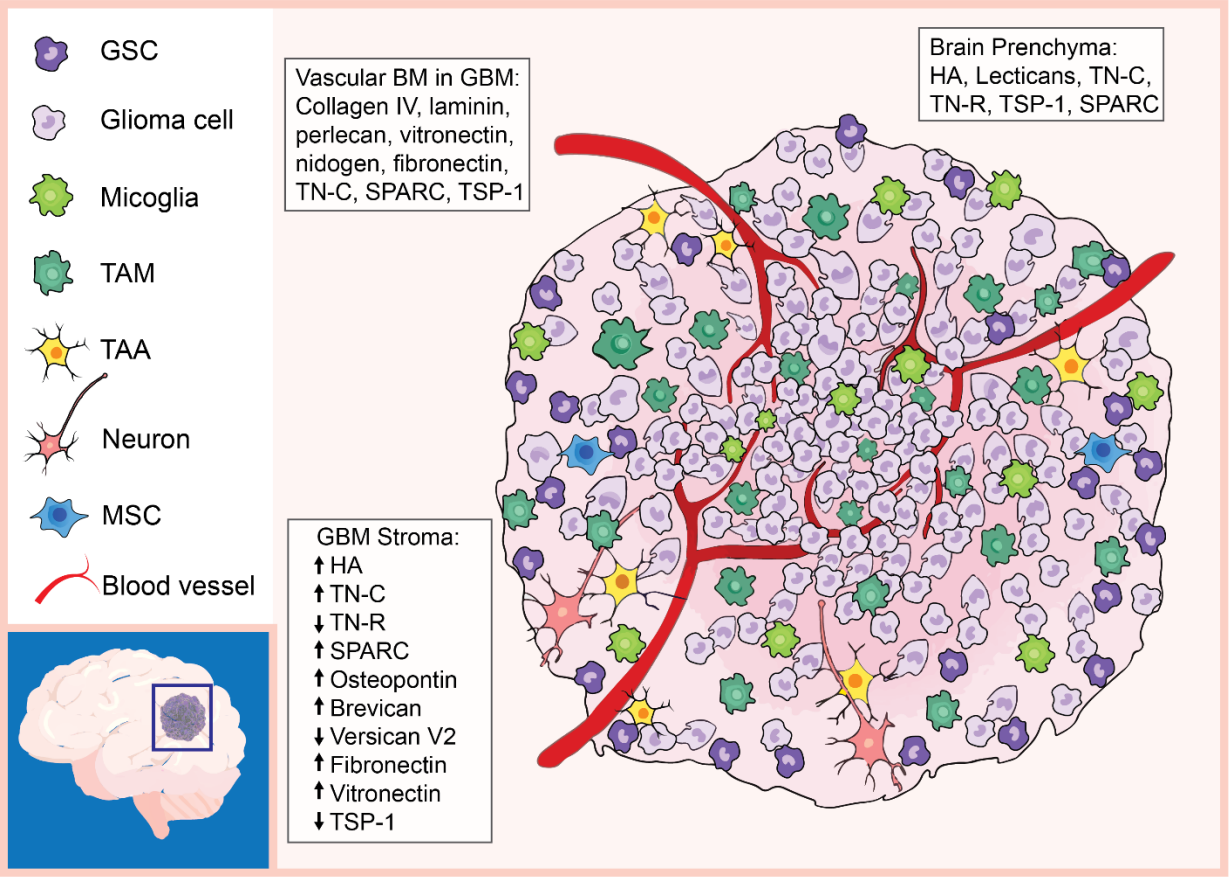

GSC: glioblastoma stem cell. TAM: tumor-associated macrophage. TAA: tumor-associated astrocyte. MSC: mesenchymal stem cell. BM: basement membrane. HA: hyaluronic acid. TN-C: tenascin-C. TN-R: tenascin-R. TSP-1: thrombospondin-1. SPARC: secreted protein acidic and rich in cysteine. GBM: glioblastoma.

Figure 1.2 Cellular and ECM compositions of brain parenchyma and GBM microenvironments.

These immune components promote tumor invasiveness through upregulation of matrix metalloproteases (MMPs), such as MMP-2 and MMP-9.[86] Astrocytes can be recruited and activated by tumor cells through multiple modes of communication, including extracellular vesicles and efflux transporters. Tumor-associated, reactive astrocytes promote the invasion of CD133-positive glioblastoma stem cells (GSCs) and secrete anti-inflammatory cytokines, such as TGFβ, that suppress anti-tumor immune respones, resulting in an overall immunosuppressive GBM microenvironment.[87,88] Glutamatergic synaptic communications between tumor cells and neurons promote GBM growth and invasion, and other neuronal effects on GBM have been attributed to autocrine signaling and paracrine signaling.[89] MSCs are also important stromal

components in the GSC niche that can promote a mesenchymal tumor transcriptional state and mediate tumor proliferation through interlukin-6 and exosomes containing miRNA-1587.[90,91]

Neoplastic tumor cells are not homogeneous populations; single cell -omics studies confirm multiple cellular states, including stem cell-like GSCs, which promote tumor initiation, therapeutic resistance, and regrowth after therapy.[92,93] GBM cells diffusively invade into the brain parenchyma, precluding complete surgical removal. Adhesion molecules, including CD44 and receptor for hyaluronan mediated motility (RHAMM), are expressed on the cell surface of GBM cells, augmenting adhesion and migration along brain ECM rich in HA.[72] Neoplastic cells remodel the local ECM to assist invasion through secretion of multiple proteases, such as MMPs and plasminogen activators (PAs).[50] GBM rarely metastasize outside the CNS, suggesting that neoplastic cells have adapted to the distinct CNS microenvironment.

1.4 Relevant biomaterials for modeling GBM

Biomimetic 3D models require biomaterials with good biocompatibility and tissue-specific properties, including appropriate biophysical/biochemical properties and degradation kinetics.[8] Biomaterials form structural networks that foster cell adhesion, proliferation, and migration, and provide specific spatiotemporal cues to modulate cell behaviors. Here we discuss biomaterials in the order of their relevance to the brain microenvironment and appropriateness for 3D modeling and 3D bioprinting (**Table 1.3**). Two primary categories of biomaterials include: (1) natural materials that are constituents of the native tissue ECM, and (2) synthetic materials with good biocompatibility. Natural materials are innately biocompatible and bioactive, possessing biochemical and biophysical features that result in exceptional biomimicry, and can be remodeled or cleared through natural degradation mechanisms. Alternatively, synthetic materials have defined chemical structures and tunable properties, but lack the innate bioactivity or physiologic

degradation mechanisms. However, synthetic materials can be modified to incorporate adhesive peptides or cleavable linkers to mimic the functional or structural properties of the native ECM.[54] It is common for 3D modeling to combine several biomaterials to take advantage of the collective properties of each individual component.

For clarity, biomaterials suitable for bioprinting processes will henceforth be referred to as bioinks. Developing bioinks with good printability and biomimicry is critical to 3D bioprinting applications. The printability of bioinks include various aspects, such as viscosity, thermo-sensitivity, and photosensitivity, depending on the specific bioprinting modality. Additionally, rheological properties, crosslinking mechanisms and kinetics, and post-printing mechanical properties, such as the elastic modulus and the swelling ratio, are important parameters of the bioinks.[19] To enhance biomimicry, bioinks are often integrated with cells, growth factors, cytokines, and other molecules to accommodate specific biological applications.

Table 1.3 Brain-relevant natural and synthetic biomaterials.

Material	Type	Crosslinking mechanisms	Common modifications	Composite with other biomaterials	Brain-relevant elastic modulus	Ref.
HA	Natural polysaccharide	Photo-crosslinking, shear thinning	Methacrylic anhydride, glycidyl methacrylate, thiol, RGD peptide	Collagen, gelatin, GelMA, chitosan, laminin, fibrin, PEG, PU	11 Pa to 3.5 kPa	[12,72,94–101]
Gelatin	Natural protein	Thermal, photo-crosslinking, enzymatic	Methacrylate	HA, PU, collagen, PEGDA, fibrin, alginate, chitosan, fibrinogen	0.49 – 12.8 kPa	[102–108]
dECM	Natural mixture	Relies on composite material	-	Collagen	78.09 ± 29.22 Pa	[109]
Collagen	Natural protein	Thermal, Photo-crosslinking	Methacrylate	HA, GelMA, fibrin, agarose, riboflavin	0.9 – 3.6 kPa	[100,110–112]
Matrigel	Natural mixture	Thermal	-	PEG, gelatin, alginate, agarose	0.4 kPa	[113–116]
Fibrin	Natural protein	Enzymatic	-	HA, collagen, laminin	0.058 – 4 kPa	[99,117,118]
Silk fibroin	Natural protein	Photo-crosslinking, Thermal	Methacrylate	Collagen, gelatin	17.1 ± 7.8 kPa	[44,119]
Gellan gum	Natural protein	Calcium ions, photo-crosslinking	RGD peptide, methacrylate	GelMA	6.4 – 17.2 kPa	[120,121]
PNIPAAm	Synthetic polymer	Thermal	-	PEG	1.4 – 3.8 kPa	[122,123]
PU	Synthetic polymer	Thermal, Photo-crosslinking	-	HA, gelatin	0.6 – 8.1 kPa	[106,124]
PEG	Synthetic polymer	Photo-crosslinking, click chemistry	Methacrylate, thiol, diacrylate, RGD peptide	HA, GelMA, PNIPAAm, laminin	1 – 26 kPa	[79]
SAP	Synthetic peptide	Self-assembly	-	-	0.3 – 5.3 kPa	[125,126]

1.4.1. Natural biomaterials and their derivatives

1.4.1.1. HA

HA is a negatively charged, linear polysaccharide composed of alternating D-glucuronic acid and N-acetyl-D-glucosamine, synthesized at cell plasma membranes of neurons and glial cells.[127] Due to the predominance of HA in the brain and GBM stroma and its critical role in regulating diverse physiological and pathological processes through interaction with cells and other ECM components, HA-based hydrogels are the most relevant matrix materials for modeling brain tissues and brain tumors. HA hydrogels have nanoporous structures and a range of elastic modulus recapitulating the brain and the GBM stroma.[95] HA has been combined with various biomaterials, including type I collagen,[97] gelatin methacrylate (GelMA),[72] chitosan,[98] laminin, fibrin,[99] and PEG[79] to fabricate 3D GBM models. HA demonstrates size-dependent regulatory behaviors, so the range of molecular weight of HA should be considered when designing specific models. HA with over 1,000 kDa is appropriate for modeling the healthy brain tissue, while HA with lower molecular weight has been observed in GBM stroma and affects GBM progression and migration. By fixing the poroelastic properties of a series of HA-GelMA hydrogels, lower molecular weight HAs (10 kDa and 60 kDa) result in higher invasiveness compared to higher molecular weight HA (500 kDa). The molecular weights of HA did not affect the elastic modulus of HA-GelMA hydrogels; all groups were measured around 3 kPa.[72] Scaffolds made of HA, laminin, and fibrin support human neural precursor cells (NPCs) growth and vascular formation.[99]

Chemical modifications to generate HA derivatives appropriate for 3D modeling or 3D bioprinting have been previously reviewed.[95] Modifications generally target the carboxylate group on the D-glucuronic acid moiety, the N-acetyl group on the N-acetyl-D-glucosamine moiety, and the hydroxyl groups on both moieties. HA-derivatives form hydrogels through radical polymerization. For example, HA functionalized with glycidyl methacrylate or methacrylic

anhydride on the C-6 hydroxyl group of the N-acetyl-D-glucosamine to form GMHA or methacrylated HA (MeHA) can be photopolymerized to form hydrogel in the presence of photo-initiators, such as lithium phenyl-2,4,6-trimethylbenzoylphosphinate (LAP).[95] GMHA and MeHA are suitable bioinks for light-assisted bioprinting due to their rapid photo-polymerization ability. Liver tissues and GBM models have been bioprinted using GMHA-based hydrogel mixture.[4,12] MeHA has also been functionalized with Arg-Gly-Asp (RGD) peptides to facilitate cell adhesion to the 3D matrix.[94] Another method to form HA-based hydrogel is through addition and condensation reactions. HA thiol derivatives spontaneously crosslink through disulfide bond formation in air without initiators, making it a good bioink candidate for extrusion or inkjet bioprinting.[96] Aldehyde-, dihydrazide-, and haloacetate-modified HA form biocompatible hydrogels through addition and condensation reactions.

1.4.1.2. Gelatin

Gelatin is a partial hydrolysis product of collagen. Gelatin and its derivatives are widely used in 3D tissue modeling due to their inherent bioactive features including integrin binding RGD sequences and MMP digestion sites. Coculture of perivascular niche (PVN) cells and GBM cells in a 3D gelatin matrix demonstrated elevated levels of angiogenesis and ECM remodeling compared to tumor cells or PVN cells cultured alone.[103] Due to good rheological properties and thermally responsive characteristics, gelatin-based materials are popular bioinks used in extrusion-based bioprinting.[128] Encapsulation of hepatocytes has been achieved with gelatin hydrogel, and the 3D-printed tissue remains viable and functional over two months of culture.[108] Gelatin can also be combined with synthetic materials, such as PU, to improve its printability in terms of longer bioprinting window and higher resolution. A gelatin-PU matrix allowed high viability and proliferation of MSCs.[106] GelMA is a versatile derivative of gelatin also popular for 3D

bioprinting. GelMA is developed by modifying the lysine and hydroxyl groups with methacrylamide and methacrylate side groups, rendering the prepolymer GelMA bioink photo-polymerizable in the presence of photo-initiators under UV exposure.[104] GelMA preserves the biological features of gelatin and enables tunable mechanical properties of 3D matrices. GelMA can serve as the base matrix material to facilitate investigation of other functional ECM such as HA in brain-related studies. The effects of biochemical cues from HA on tumor growth have been investigated by mixing gelatin-based matrix with different amounts of soluble or immobilized HA.[107] The expression of angiogenic markers and hypoxia markers demonstrate biphasic peaks when HA concentration falls between 0.3% and 0.5%.[105] GelMA-based hydrogels can generate gradients of HA, crosslinking density, and GBM cell density.[105] Spatially gradated matrix reveals that tumor cell proliferation and pro-angiogenic expressions correlate with the local crosslinking density and tumor cell density, whereas the local MMP2 expression inversely correlated with the cell density. GelMA has also been combined with PEGDA to generate cardiac patch for the treatment of myocardial infarction.[129]

1.4.1.3. Collagen

Collagen is a ubiquitous ECM component in most body tissues. Although the brain is virtually absent of the fibrillar collagen type I, the vascular basement membrane is abundant with collagen type IV and some collagen type V. Thus, collagen-derived biomaterials are appropriate for modeling the BBB. Nonetheless, various GBM studies have exploited collagen biomaterials due to their well-studied gelation mechanism, including pH-based and temperature-based, abundance of cell binding sites, and tunable mechanical properties to match tissue-specific requirements. GBM cells adopt different morphologies in 3D matrices by collagen types: round in type IV and spindle-like in type I/III.[100] Collagen is commonly combined with other biomaterials,

including HA, agarose, and synthetic materials, for tissue modeling. In a hybrid matrix with HA, only collagen type IV, not type III, supports GBM cell proliferation.[101] Pure collagen solutions have relatively slow gelation process and low viscosity.[130] Increasing the concentration of collagen or including riboflavin in the pre-polymer solution improves bioprinting accuracy.[110,111] Inclusion of riboflavin increases the storage modulus of collagen bioinks, improving printability. Gelation of collagen-based bioinks is usually thermally controlled or pH-driven, and collagen-based bioprinting has been used in tissue engineering applications, including heart regeneration and liver modeling.[130–132] The hydrogel elastic modulus can be tailored between 0.9 kPa and 3.6 kPa, which is suitable for brain tissues.[110]

1.4.1.4. Decellularized ECM (dECM)

DECM is obtained by removing all cellular components of a tissue while preserving most of the tissue-specific and patient/host-specific ECM structures and components, retaining native ECM cues conducive to cell growth.[42] The analysis of GBM patient brain tissue-derived dECM has demonstrated that GAGs, HA, collagen IV, laminin, and fibronectin are not significantly disturbed after processing, thus appropriate as an *in vitro* modeling biomaterial.[109] Patient brain dECM has been mixed with collagen to achieve better gelation through extrusion-based biopriting. Compared to cells in the collagen control, disseminated single cells have heterogeneous and rounded morphologies in the patient dECM-based matrix. Moreover, GBM cells in dECM-based matrix express increased level of matrix remodeling protein MMP9 and HA-related genes, including Hyal1, Hyal2, HAS2, and CD44.[109] While the slow gelation kinetics of dECM-based hydrogels often necessitate the integration of dECM bioinks with other biomaterial to improve printability, recent studies have induced thermal gelation of the dECM bioinks alone.[133–135] Bioinks based on dECM have been developed for various tissues, such as cartilage, heart, adipose,

liver, and tumors, and demonstrate good printability on extrusion-based and DLP-based bioprinters.[42,134–137] However, dECM is usually derived from an individual's tissue and contains a variety of natural proteins and polysaccharides, so variation is inevitable and control over specific variables is challenging. Despite the limitations, dECM with its potential in GBM modeling for individual patients, remains an exceptional choice of biomaterial for precision medicine applications.

1.4.1.5. Matrigel

Matrigel is a thermally curable mixture of ECM components derived from murine Engelbreth-Holm-Swarm sarcoma, composed of about 60% laminin, 30% collagen type IV, 8% nidogen, and other growth factors and proteoglycans. Its similarity to the vascular ECM composition makes it especially suitable for BBB modeling.[49] As a result, Matrigel is broadly used for vascular formation and related studies *in vitro*. GBM organoids have also been developed in Matrigel, with cells within the organoid displaying hypoxic gradients and heterogeneity in stemness and proliferation.[5] However, the majority of proteins in Matrigel are present in low amounts in the brain (excluding the BBB) or GBM, making it a suboptimal choice for GBM modeling, even though many studies have demonstrated good GBM cell viability and proliferation in the matrix. Limitations of Matrigel include its animal origin, batch variation that reduce experimental reproducibility, and limited control over the physiochemical properties of the formed 3D matrix. Matrigel also has limited printability due to its relatively poor mechanical properties and lack of photo-sensitivity, and thus it is often combined with other biomaterials, such as agarose, alginate, and gelatin, to fabricate scaffolds or tissue models using 3D bioprinting technologies.[114–116]

1.4.1.6. Fibrin

Fibrin is formed by crosslinking of fibrinogen and thrombin. Mechanical properties of fibrin hydrogels depend mainly on the concentration of fibrinogen and to the lesser extent on the thrombin. Stiffness ranging from 0.058 kPa to 4 kPa, a relevant range for brain applications, can be achieved with a fibrin matrix.[117] Co-culture models of GBM spheroids and endothelial cells in a fibrin matrix have been used to test anti-angiogenic compounds.[118] Vascular endothelial growth factor (VEGF)-loaded fibrin hydrogels support neural stem cell growth and migration compared to fibrin matrix with no VEGF or VEGF-loaded collagen hydrogel, demonstrating beneficial properties of fibrin matrices to embed growth factors for extended culture time.[112] Similarly, improved cell proliferation and prolonged persistence have been observed for cytotoxic human MSCs cultured in fibrin matrices, enabling MSC-based GBM therapy to suppress post-surgical recurrence.[138] Fibrin-based bioinks are popular with extrusion-based bioprinting. Fibrin bioinks have been mixed with gelatin, alginate, or HA to improve its mechanical and biochemical properties, and have generated various tissue models including GBM models, cardiac tissues, and dentin-pulp complex.[139–141]

1.4.1.7. Others

Other natural biomaterials that are not native in the brain but with good biocompatibility and printability have also been explored for CNS studies. Silk fibroin (SF) have been used for neural network formation and gellan gum for multilayer neural circuit formation.[119,120] The range of stiffness of the SF hydrogels and GG hydrogels is appropriate for modeling the GBM stroma. A human GBM cell line exhibited distinct responses in two types of SF hydrogels – enhanced viability and proliferation in the random coil type and induced apoptosis in the crystalline type.[142] SF hydrogels with tunable mechanical properties and post-printing degradation rates can also be adapted to different bioprinting applications.[143] Other non-network-forming ECM components

present in the native tumor stroma or the BBB may be incorporated into 3D matrices with the above-mentioned hydrogel-forming biomaterials to improve the material biomimicry in future studies.

1.4.2 Synthetic Biomaterials

Despite a non-biological origin, synthetic biomaterials can be readily modified to have mechanically and biochemically robust properties and degradation kinetics for biological modeling. By functionalizing with cell adhesion peptides and MMP-cleavable sequences, or mixing with other natural biomaterials, synthetic biomaterials-based hydrogels can create microenvironments with comparable properties to native ones. Models based on synthetic biomaterials generally have good scalability and reproducibility due to their synthetic nature. In addition to cell-encapsulating models, synthetic materials are suitable for fabricating cell culture scaffolds, microfluidic devices, or implantable devices. GBM cells cultured on polystyrene scaffolds have generated more clinically relevant drug efficacy predictions for TMZ, erlotinib, and bevacizumab than traditional 2D cultures.[144]

1.4.2.1. Synthetic polymers

Poly(N-isopropylacrylamide) (PNIPAAm), PEG, and PU are synthetic biomaterials that have been used for GBM studies. PNIPAAm and its composite materials are thermo-responsive hydrogels and demonstrate good printability on extrusion-based bioprinters.[145] PNIPAAm embedded with gold nanorods can be printed with multiphoton lithography to achieve a nano-scale resolution and post-printing dynamic modulations.[146] Primary GSCs cultured in a PNIPAAm-PEG matrix retain stemness over long-term culture and can be easily retrieved and re-encapsulated by adjusting the temperature of the hydrogel.[122] The hydrogel can expand GSCs into large numbers necessary for screening purposes. PEG is a popular biomaterial for 3D tissue modeling due to its good biocompatibility, inert biochemical properties, and tunable mechanical properties.[43] PEG

and its deriviatives can be readily modified with bioactive components to enhance its biomimicry and printbility as bioinks.[147–149] PEG hydrogels mixed with fixed concentration of HA and functionalized by RGD peptides and MMP degradation crosslinkers, have been used to investigate the stiffness impacts on GBM progression.[79] GBM cells cultured in a stiff PEG hydrogel (26 kPa) form denser tumor spheroids compared to the cells in a softer structure (1 kPa). PEGDA is a derivative of PEG that have demonstrated broad applications in 3D bioprinting due to its biocompatibility and photo-polymerizability.[46] PEGDA has been used to form microwells for the *in vitro* culture of glioblastoma cells or co-culture of glioblastoma cells with endothelial cells for high throughput drug screening.[150,151] PU hydrogels are thermo-responsive and biodegradable. Neural stem cells embedded in a water-based PU hydrogesl through 3D bioprinting have demonstrated excellent growth and differentiation potential.[124]

1.4.2.2. Self-assembled peptides

Self-assembled peptide (SAP)-based hydrogels are crosslinked by physical or chemical bonding of the peptides, forming organized nanofibrous β-sheets resembling the native ECM structures.[152] Peptides are chains of amino acids that possess innate biological properties. Fibrous SAP hydrogels have tunable mechanical properties and controllable stimuli-responsive gelation processes (e.g. enzymatic triggering), making them promising bioinks for extrusion-based bioprinting.[126,153] Proof-of-concept extrusion-based printing of fluorecent SAP hydrogels demonstrate good mechanical stability and low erosion rate in solutions.[154] The injectability of SAP and its ability to adapt to irregular shapes also makes it a good candidate for CNS regenerations, such as BBB repair or brain tissue repair after GBM surgery. A peptide RADA16-SVVYGLR-forming hydrogel with a stiffness between 0.326 kPa and 5.336 kPa injected into the brain of a zebrafish brain injury model induces both angiogenesis and neurogenesis.[125]

1.5 Research Objectives

Although current advances in additive manufacturing, material science, and biology such as single cell sequencing provide many essential tools and information needed to fabricate constructs with the living cells in vitro, there remain substantial challenges with modeling the complex and highly heterogeneous tissue microenvironment. The objectives of this thesis are investigating and modeling the ECM properties and cellular microenvironment of the GBM and using the developed 3D-bioprinted GBM models to investigate cellular interactions, transformations, and drug susceptibilities.

Acknowledgements

Chapter 1, in part, is adapted from the published article, "Biomaterials and 3D Bioprinting Strategies to Model Glioblastoma and the Blood–Brain Barrier", M. Tang, J. Rich, S. Chen. *Advanced Materials*, 2020. The dissertation author was the primary investigator and author of this paper.

We thank our funding sources: CA253615 and EB021857 (to S.C.), CA197718, CA154130, CA169117, CA171652, NS087913, NS089272, and NS103434 (to J.N.R.). The authors thank Jiayi Wang for assistance on the digital illustration of tissue microenvironments.

References

1. Ostrom, Q. T. *et al.* CBTRUS Statistical Report: Primary Brain and Other Central Nervous System Tumors Diagnosed in the United States in 2012-2016. *Neuro-oncology* **21**, v1–v100 (2019).

2. Koshy, M. *et al.* Improved survival time trends for glioblastoma using the SEER 17 population-based registries. *J Neurooncol* **107**, 207–212 (2012).

3. Hidalgo, M. *et al.* Patient-Derived Xenograft Models: An Emerging Platform for Translational Cancer Research. *Cancer Discovery* **4**, 998–1013 (2014).

4. Tang, M. *et al.* Three-dimensional bioprinted glioblastoma microenvironments model cellular dependencies and immune interactions. *Cell Res* 1–21 (2020) doi:10.1038/s41422-020-0338-1.

5. Hubert, C. G. *et al.* A Three-Dimensional Organoid Culture System Derived from Human Glioblastomas Recapitulates the Hypoxic Gradients and Cancer Stem Cell Heterogeneity of Tumors Found In Vivo. *Cancer Res.* **76**, 2465–2477 (2016).

6. Jacob, F. *et al.* A Patient-Derived Glioblastoma Organoid Model and Biobank Recapitulates Inter- and Intra-tumoral Heterogeneity. *Cell* **180**, 188-204.e22 (2020).

7. Ruck, T., Bittner, S. & Meuth, S. G. Blood-brain barrier modeling: challenges and perspectives. *Neural Regen Res* **10**, 889–891 (2015).

8. Murphy, S. V. & Atala, A. 3D bioprinting of tissues and organs. *Nature Biotechnology* **32**, 773–785 (2014).

9. Malda, J. *et al.* 25th Anniversary Article: Engineering Hydrogels for Biofabrication. *Advanced Materials* **25**, 5011–5028 (2013).

10. Gebinoga, M. *et al.* Multi-photon structuring of native polymers: A case study for structuring natural proteins. *Engineering in Life Sciences* **13**, 368–375 (2013).

11. Zhu, W. *et al.* Direct 3D bioprinting of prevascularized tissue constructs with complex microarchitecture. *Biomaterials* **124**, 106–115 (2017).

12. Ma, X. *et al.* Deterministically patterned biomimetic human iPSC-derived hepatic model via rapid 3D bioprinting. *Proc. Natl. Acad. Sci. U.S.A.* **113**, 2206–2211 (2016).

13. Hosseinzadeh, R. *et al.* A Drug-Eluting 3D-Printed Mesh (GlioMesh) for Management of Glioblastoma. *Advanced Therapeutics* **2**, 1900113 (2019).

14. Tasoglu, S. & Demirci, U. Bioprinting for stem cell research. *Trends in Biotechnology* **31**, 10–19 (2013).

15. Boland, T., Xu, T., Damon, B. & Cui, X. Application of inkjet printing to tissue engineering. *Biotechnology Journal* **1**, 910–917 (2006).

16. Derakhshanfar, S. *et al.* 3D bioprinting for biomedical devices and tissue engineering: A review of recent trends and advances. *Bioact Mater* **3**, 144–156 (2018).

17. Ma, X. *et al.* 3D bioprinting of functional tissue models for personalized drug screening and in vitro disease modeling. *Advanced Drug Delivery Reviews* **132**, 235–251 (2018).

18. Pereira, R. F. & Bártolo, P. J. 3D bioprinting of photocrosslinkable hydrogel constructs. *Journal of Applied Polymer Science* **132**, (2015).

19. Hölzl, K. *et al.* Bioink properties before, during and after 3D bioprinting. *Biofabrication* **8**, 032002 (2016).

20. Miri, A. K. *et al.* Bioprinters for Organs-On-Chips. *Biofabrication* **11**, 042002 (2019).

21. Raman, R. & Bashir, R. Chapter 6 - Stereolithographic 3D Bioprinting for Biomedical Applications. in *Essentials of 3D Biofabrication and Translation* (eds. Atala, A. & Yoo, J. J.) 89–121 (Academic Press, 2015). doi:10.1016/B978-0-12-800972-7.00006-2.

22. Kelly, B. E. *et al.* Volumetric additive manufacturing via tomographic reconstruction. *Science* **363**, 1075–1079 (2019).

23. Gudapati, H., Dey, M. & Ozbolat, I. A comprehensive review on droplet-based bioprinting: Past, present and future. *Biomaterials* **102**, 20–42 (2016).

24. Xu, T., Jin, J., Gregory, C., Hickman, J. J. & Boland, T. Inkjet printing of viable mammalian cells. *Biomaterials* **26**, 93–99 (2005).

25. Park, T.-M. *et al.* Fabrication of In Vitro Cancer Microtissue Array on Fibroblast-Layered Nanofibrous Membrane by Inkjet Printing. *Int J Mol Sci* **18**, (2017).

26. Xu, T. *et al.* Complex heterogeneous tissue constructs containing multiple cell types prepared by inkjet printing technology. *Biomaterials* **34**, 130–139 (2013).

27. Sun, Y., Song, W., Sun, X. & Zhang, S. Inkjet-Printing Patterned Chip on Sticky Superhydrophobic Surface for High-Efficiency Single-Cell Array Trapping and Real-Time Observation of Cellular Apoptosis. *ACS Appl. Mater. Interfaces* **10**, 31054–31060 (2018).

28. Roth, E. A. *et al.* Inkjet printing for high-throughput cell patterning. *Biomaterials* **25**, 3707–3715 (2004).

29. Cooper, G. M. *et al.* Inkjet-Based Biopatterning of Bone Morphogenetic Protein-2 to Spatially Control Calvarial Bone Formation. *Tissue Engineering Part A* **16**, 1749–1759 (2010).

30. Xu, F. *et al.* A three-dimensional in vitro ovarian cancer coculture model using a high-throughput cell patterning platform. *Biotechnology Journal* **6**, 204–212 (2011).

31. Suntivich, R., Drachuk, I., Calabrese, R., Kaplan, D. L. & Tsukruk, V. V. Inkjet Printing of Silk Nest Arrays for Cell Hosting. *Biomacromolecules* **15**, 1428–1435 (2014).

32. Mironov, V. *et al.* Organ printing: tissue spheroids as building blocks. *Biomaterials* **30**, 2164–2174 (2009).

33. Chang, C. C., Boland, E. D., Williams, S. K. & Hoying, J. B. Direct-write bioprinting three-dimensional biohybrid systems for future regenerative therapies. *J. Biomed. Mater. Res.* **98B**, 160–170 (2011).

34. De Coppi, P. *et al.* Isolation of amniotic stem cell lines with potential for therapy. *Nat. Biotechnol.* **25**, 100–106 (2007).

35. Ozbolat, I. T. & Hospodiuk, M. Current advances and future perspectives in extrusion-based bioprinting. *Biomaterials* **76**, 321–343 (2016).

36. Guillotin, B. *et al.* Laser assisted bioprinting of engineered tissue with high cell density and microscale organization. *Biomaterials* **31**, 7250–7256 (2010).

37. Barron, J. A., Ringeisen, B. R., Kim, H., Spargo, B. J. & Chrisey, D. B. Application of laser printing to mammalian cells. *Thin Solid Films* **453–454**, 383–387 (2004).

38. Hribar, K. C., Soman, P., Warner, J., Chung, P. & Chen, S. Light-assisted direct-write of 3D functional biomaterials. *Lab Chip* **14**, 268–275 (2013).

39. Knowlton, S., Onal, S., Yu, C. H., Zhao, J. J. & Tasoglu, S. Bioprinting for cancer research. *Trends in Biotechnology* **33**, 504–513 (2015).

40. Zhang, W. & Chen, S. Femtosecond laser nanofabrication of hydrogel biomaterial. *MRS Bulletin* **36**, 1028–1033 (2011).

41. Ma, X. *et al.* 3D printed micro-scale force gauge arrays to improve human cardiac tissue maturation and enable high throughput drug testing. *Acta Biomater* **95**, 319–327 (2019).

42. Ma, X. *et al.* Rapid 3D bioprinting of decellularized extracellular matrix with regionally varied mechanical properties and biomimetic microarchitecture. *Biomaterials* **185**, 310–321 (2018).

43. Soman, P. *et al.* Cancer cell migration within 3D layer-by-layer microfabricated photocrosslinked PEG scaffolds with tunable stiffness. *Biomaterials* **33**, 7064–7070 (2012).

44. Kim, S. H. *et al.* Precisely printable and biocompatible silk fibroin bioink for digital light processing 3D printing. *Nat Commun* **9**, 1620 (2018).

45. Wang, P. *et al.* Controlled Growth Factor Release in 3D-Printed Hydrogels. *Adv. Healthcare Mater.* 1900977 (2019) doi:10.1002/adhm.201900977.

46. Koffler, J. *et al.* Biomimetic 3D-printed scaffolds for spinal cord injury repair. *Nat Med* **25**, 263–269 (2019).

47. Qu, X. *et al.* Relative impact of uniaxial alignment vs. form-induced stress on differentiation of human adipose derived stem cells. *Biomaterials* **34**, 9812–9818 (2013).

48. Huang, T. Q., Qu, X., Liu, J. & Chen, S. 3D printing of biomimetic microstructures for cancer cell migration. *Biomed Microdevices* **16**, 127–132 (2014).

49. Xiao, W., Sohrabi, A. & Seidlits, S. K. Integrating the glioblastoma microenvironment into engineered experimental models. *Future Science OA* **3**, FSO189 (2017).

50. Bellail, A. C., Hunter, S. B., Brat, D. J., Tan, C. & Van Meir, E. G. Microregional extracellular matrix heterogeneity in brain modulates glioma cell invasion. *Int. J. Biochem. Cell Biol.* **36**, 1046–1069 (2004).

51. Bignami, A., Hosley, M. & Dahl, D. Hyaluronic acid and hyaluronic acid-binding proteins in brain extracellular matrix. *Anat Embryol* **188**, (1993).

52. Cowman, M. K., Lee, H.-G., Schwertfeger, K. L., McCarthy, J. B. & Turley, E. A. The Content and Size of Hyaluronan in Biological Fluids and Tissues. *Front Immunol* **6**, (2015).

53. Faissner, A. The tenascin gene family in axon growth and guidance. *Cell Tissue Res* **290**, 331–341 (1997).

54. Wolf, K. J., Chen, J., Coombes, J. D., Aghi, M. K. & Kumar, S. Dissecting and rebuilding the glioblastoma microenvironment with engineered materials. *Nat Rev Mater* **4**, 651–668 (2019).

55. Theocharis, A. D., Skandalis, S. S., Gialeli, C. & Karamanos, N. K. Extracellular matrix structure. *Advanced Drug Delivery Reviews* **97**, 4–27 (2016).

56. Pas, J. *et al.* Analysis of structure and function of tenascin-C. *The International Journal of Biochemistry & Cell Biology* **38**, 1594–1602 (2006).

57. Lau, L. W., Cua, R., Keough, M. B., Haylock-Jacobs, S. & Yong, V. W. Pathophysiology of the brain extracellular matrix: a new target for remyelination. *Nature Reviews Neuroscience* **14**, 722–729 (2013).

58. Brösicke, N. & Faissner, A. Role of tenascins in the ECM of gliomas. *Cell Adhesion & Migration* **9**, 131–140 (2015).

59. Brekken, R. A. & Sage, E. H. SPARC, a matricellular protein: at the crossroads of cell-matrix communication. *Matrix Biol.* **19**, 816–827 (2001).

60. Shevde, L. A. & Samant, R. S. Role of osteopontin in the pathophysiology of cancer. *Matrix Biology* **37**, 131–141 (2014).

61. Yamaguchi, Y. Lecticans: organizers of the brain extracellular matrix: *CMLS, Cell. Mol. Life Sci.* **57**, 276–289 (2000).

62. Jones, C. L., Liu, J. & Xu, D. Structure, Biosynthesis, and Function of Glycosaminoglycans. in *Comprehensive Natural Products II* 407–427 (Elsevier, 2010). doi:10.1016/B978-008045382-8.00132-5.

63. Iozzo, R. V. & Schaefer, L. Proteoglycan form and function: A comprehensive nomenclature of proteoglycans. *Matrix Biology* **42**, 11–55 (2015).

64. Dwyer, C. A., Bi, W. L., Viapiano, M. S. & Matthews, R. T. Brevican knockdown reduces late-stage glioma tumor aggressiveness. *J Neurooncol* **120**, 63–72 (2014).

65. Jaworski, D. M., Kelly, G. M., Piepmeier, J. M. & Hockfield, S. BEHAB (brain enriched hyaluronan binding) is expressed in surgical samples of glioma and in intracranial grafts of invasive glioma cell lines. *Cancer Res.* **56**, 2293–2298 (1996).

66. Cragg, B. Brain extracellular space fixed for electron microscopy. *Neuroscience Letters* **15**, 301–306 (1979).

67. Bonneh-Barkay, D. & Wiley, C. A. Brain Extracellular Matrix in Neurodegeneration. *Brain Pathology* **19**, 573–585 (2009).

68. Eroglu, C. The role of astrocyte-secreted matricellular proteins in central nervous system development and function. *J. Cell Commun. Signal.* **3**, 167–176 (2009).

69. Engler, A. J., Sen, S., Sweeney, H. L. & Discher, D. E. Matrix Elasticity Directs Stem Cell Lineage Specification. *Cell* **126**, 677–689 (2006).

70. Wang, T.-W. & Spector, M. Development of hyaluronic acid-based scaffolds for brain tissue engineering. *Acta Biomaterialia* **5**, 2371–2384 (2009).

71. Dawson, D. W. *et al.* CD36 Mediates the In Vitro Inhibitory Effects of Thrombospondin-1 on Endothelial Cells. *J Cell Biol* **138**, 707–717 (1997).

72. Chen, J.-W. E. *et al.* Influence of Hyaluronic Acid Transitions in Tumor Microenvironment on Glioblastoma Malignancy and Invasive Behavior. *Front. Mater.* **5**, (2018).

73. Gilg, A. G. *et al.* Targeting hyaluronan interactions in malignant gliomas and their drug-resistant multipotent progenitors. *Clin. Cancer Res.* **14**, 1804–1813 (2008).

74. Zhang, B. *et al.* INT-HA induces M2-like macrophage differentiation of human monocytes via TLR4-miR-935 pathway. *Cancer Immunol. Immunother.* **68**, 189–200 (2019).

75. Arslan, F. *et al.* The role of versican isoforms V0/V1 in glioma migration mediated by transforming growth factor-β2. *Br J Cancer* **96**, 1560–1568 (2007).

76. Gladson, C. L. & Cheresh, D. A. Glioblastoma expression of vitronectin and the alpha v beta 3 integrin. Adhesion mechanism for transformed glial cells. *J. Clin. Invest.* **88**, 1924–1932 (1991).

77. Serres, E. *et al.* Fibronectin expression in glioblastomas promotes cell cohesion, collective invasion of basement membrane in vitro and orthotopic tumor growth in mice. *Oncogene* **33**, 3451–3462 (2014).

78. Polacheck, W. J., Zervantonakis, I. K. & Kamm, R. D. Tumor cell migration in complex microenvironments. *Cell. Mol. Life Sci.* **70**, 1335–1356 (2013).

79. Wang, C., Tong, X. & Yang, F. Bioengineered 3D Brain Tumor Model To Elucidate the Effects of Matrix Stiffness on Glioblastoma Cell Behavior Using PEG-Based Hydrogels. *Mol. Pharmaceutics* **11**, 2115–2125 (2014).

80. Chauvet, D. *et al.* In Vivo Measurement of Brain Tumor Elasticity Using Intraoperative Shear Wave Elastography. *Ultraschall in Med* **37**, 584–590 (2015).

81. Netti, P. A., Baxter, L. T., Boucher, Y., Skalak, R. & Jain, R. K. Time-dependent behavior of interstitial fluid pressure in solid tumors: implications for drug delivery. *Cancer Res.* **55**, 5451–5458 (1995).

82. Quail, D. F. & Joyce, J. A. The Microenvironmental Landscape of Brain Tumors. *Cancer Cell* **31**, 326–341 (2017).

83. Zhao, Z., Nelson, A. R., Betsholtz, C. & Zlokovic, B. V. Establishment and Dysfunction of the Blood-Brain Barrier. *Cell* **163**, 1064–1078 (2015).

84. Charles, N. A., Holland, E. C., Gilbertson, R., Glass, R. & Kettenmann, H. The brain tumor microenvironment. *Glia* **59**, 1169–1180 (2011).

85. Matias, D. *et al.* Microglia/Astrocytes–Glioblastoma Crosstalk: Crucial Molecular Mechanisms and Microenvironmental Factors. *Front. Cell. Neurosci.* **12**, (2018).

86. Brandao, M., Simon, T., Critchley, G. & Giamas, G. Astrocytes, the rising stars of the glioblastoma microenvironment. *Glia* **67**, 779–790 (2019).

87. Rath, B. H., Fair, J. M., Jamal, M., Camphausen, K. & Tofilon, P. J. Astrocytes Enhance the Invasion Potential of Glioblastoma Stem-Like Cells. *PLOS ONE* **8**, e54752 (2013).

88. Henrik Heiland, D. *et al.* Tumor-associated reactive astrocytes aid the evolution of immunosuppressive environment in glioblastoma. *Nat Commun* **10**, 2541 (2019).

89. Venkataramani, V. *et al.* Glutamatergic synaptic input to glioma cells drives brain tumour progression. *Nature* **573**, 532–538 (2019).

90. Hossain, A. *et al.* Mesenchymal Stem Cells Isolated From Human Gliomas Increase Proliferation and Maintain Stemness of Glioma Stem Cells Through the IL-6/gp130/STAT3 Pathway. *Stem Cells* **33**, 2400–2415 (2015).

91. Figueroa, J. *et al.* Exosomes from Glioma-Associated Mesenchymal Stem Cells Increase the Tumorigenicity of Glioma Stem-like Cells via Transfer of miR-1587. *Cancer Res.* **77**, 5808–5819 (2017).

92. Bao, S. *et al.* Glioma stem cells promote radioresistance by preferential activation of the DNA damage response. *Nature* **444**, 756–760 (2006).

93. Singh, S. K. *et al.* Identification of human brain tumour initiating cells. *Nature* **432**, 396–401 (2004).

94. Ananthanarayanan, B., Kim, Y. & Kumar, S. Elucidating the mechanobiology of malignant brain tumors using a brain matrix-mimetic hyaluronic acid hydrogel platform. *Biomaterials* **32**, 7913–7923 (2011).

95. Burdick, J. A. & Prestwich, G. D. Hyaluronic Acid Hydrogels for Biomedical Applications. *Advanced Materials* **23**, H41–H56 (2011).

96. Shu, X. Z., Liu, Y., Palumbo, F. & Prestwich, G. D. Disulfide-crosslinked hyaluronan-gelatin hydrogel films: a covalent mimic of the extracellular matrix for in vitro cell growth. *Biomaterials* **24**, 3825–3834 (2003).

97. Herrera-Perez, R. M. *et al.* Presence of stromal cells in a bioengineered tumor microenvironment alters glioblastoma migration and response to STAT3 inhibition. *PLoS ONE* **13**, e0194183 (2018).

98. Florczyk, S. J. *et al.* Porous chitosan-hyaluronic acid scaffolds as a mimic of glioblastoma microenvironment ECM. *Biomaterials* **34**, 10143–10150 (2013).

99. Arulmoli, J. *et al.* Combination scaffolds of salmon fibrin, hyaluronic acid, and laminin for human neural stem cell and vascular tissue engineering. *Acta Biomaterialia* **43**, 122–138 (2016).

100. Rao, S. S. *et al.* Glioblastoma Behaviors in Three-Dimensional Collagen-Hyaluronan Composite Hydrogels. *ACS Appl Mater Interfaces* **5**, 9276–9284 (2013).

101. Bonnesœur, S. *et al.* Hyaluronan-based hydrogels as versatile tumor-like models: Tunable ECM and stiffness with genipin-crosslinking. *J Biomed Mater Res A* (2020) doi:10.1002/jbm.a.36899.

102. Tan, Z., Parisi, C., Di Silvio, L., Dini, D. & Forte, A. E. Cryogenic 3D Printing of Super Soft Hydrogels. *Sci Rep* **7**, 16293 (2017).

103. Ngo, M. T. & Harley, B. A. C. Perivascular signals alter global gene expression profile of glioblastoma and response to temozolomide in a gelatin hydrogel. *Biomaterials* **198**, 122–134 (2019).

104. Van Den Bulcke, A. I. *et al.* Structural and rheological properties of methacrylamide modified gelatin hydrogels. *Biomacromolecules* **1**, 31–38 (2000).

105. Pedron, S., Becka, E. & Harley, B. A. Spatially Gradated Hydrogel Platform as a 3D Engineered Tumor Microenvironment. *Advanced Materials* **27**, 1567–1572 (2015).

106. Hsieh, C.-T. & Hsu, S.-H. Double-Network Polyurethane-Gelatin Hydrogel with Tunable Modulus for High-Resolution 3D Bioprinting. *ACS Appl Mater Interfaces* **11**, 32746–32757 (2019).

107. Chen, J.-W. E., Pedron, S. & Harley, B. A. C. The Combined Influence of Hydrogel Stiffness and Matrix-Bound Hyaluronic Acid Content on Glioblastoma Invasion. *Macromol Biosci* **17**, (2017).

108. Wang, X. *et al.* Generation of three-dimensional hepatocyte/gelatin structures with rapid prototyping system. *Tissue Eng.* **12**, 83–90 (2006).

109. Koh, I. *et al.* The mode and dynamics of glioblastoma cell invasion into a decellularized tissue-derived extracellular matrix-based three-dimensional tumor model. *Sci Rep* **8**, 4608 (2018).

110. Tirella, A., Liberto, T. & Ahluwalia, A. Riboflavin and collagen: New crosslinking methods to tailor the stiffness of hydrogels. *Materials Letters* **74**, 58–61 (2012).

111. Diamantides, N. *et al.* Correlating rheological properties and printability of collagen bioinks: the effects of riboflavin photocrosslinking and pH. *Biofabrication* **9**, 034102 (2017).

112. Lee, Y.-B. *et al.* Bio-printing of collagen and VEGF-releasing fibrin gel scaffolds for neural stem cell culture. *Experimental Neurology* **223**, 645–652 (2010).

113. Grundy, T. J. *et al.* Differential response of patient-derived primary glioblastoma cells to environmental stiffness. *Scientific Reports* **6**, 1–10 (2016).

114. Fan, R. *et al.* Bio-printing cell-laden Matrigel-agarose constructs. *J Biomater Appl* **31**, 684–692 (2016).

115. Pascoal, J. F. *et al.* Three-Dimensional Cell-Based Microarrays: Printing Pluripotent Stem Cells into 3D Microenvironments. *Methods Mol. Biol.* **1771**, 69–81 (2018).

116. Berg, J. *et al.* Optimization of cell-laden bioinks for 3D bioprinting and efficient infection with influenza A virus. *Sci Rep* **8**, 13877 (2018).

117. Duong, H., Wu, B. & Tawil, B. Modulation of 3D Fibrin Matrix Stiffness by Intrinsic Fibrinogen–Thrombin Compositions and by Extrinsic Cellular Activity. *Tissue Engineering Part A* **15**, 1865–1876 (2009).

118. Bayat, N. *et al.* The Anti-Angiogenic Effect of Atorvastatin in Glioblastoma Spheroids Tumor Cultured in Fibrin Gel: in 3D in Vitro Model. *Asian Pac J Cancer Prev* **19**, 2553–2560 (2018).

119. Tang-Schomer, M. D. *et al.* Bioengineered functional brain-like cortical tissue. *Proceedings of the National Academy of Sciences* **111**, 13811–13816 (2014).

120. Lozano, R. *et al.* 3D printing of layered brain-like structures using peptide modified gellan gum substrates. *Biomaterials* **67**, 264–273 (2015).

121. Xu, Z., Li, Z., Jiang, S. & Bratlie, K. M. Chemically Modified Gellan Gum Hydrogels with Tunable Properties for Use as Tissue Engineering Scaffolds. *ACS Omega* **3**, 6998–7007 (2018).

122. Li, Q. *et al.* Scalable Production of Glioblastoma Tumor-initiating Cells in 3 Dimension Thermoreversible Hydrogels. *Sci Rep* **6**, (2016).

123. Comolli, N., Neuhuber, B., Fischer, I. & Lowman, A. In vitro analysis of PNIPAAm–PEG, a novel, injectable scaffold for spinal cord repair. *Acta Biomaterialia* **5**, 1046–1055 (2009).

124. Hsieh, F.-Y., Lin, H.-H. & Hsu, S. 3D bioprinting of neural stem cell-laden thermoresponsive biodegradable polyurethane hydrogel and potential in central nervous system repair. *Biomaterials* **71**, 48–57 (2015).

125. Wang, T.-W. *et al.* Effects of an injectable functionalized self-assembling nanopeptide hydrogel on angiogenesis and neurogenesis for regeneration of the central nervous system. *Nanoscale* **9**, 16281–16292 (2017).

126. Raphael, B. *et al.* 3D cell bioprinting of self-assembling peptide-based hydrogels. *Materials Letters* **190**, 103–106 (2017).

127. Perkins, K. L., Arranz, A. M., Yamaguchi, Y. & Hrabetova, S. Brain extracellular space, hyaluronan, and the prevention of epileptic seizures. *Rev Neurosci* **28**, 869–892 (2017).

128. Wang, X. *et al.* Gelatin-Based Hydrogels for Organ 3D Bioprinting. *Polymers* **9**, 401 (2017).

129. Cui, H. *et al.* 4D physiologically adaptable cardiac patch: A 4-month in vivo study for the treatment of myocardial infarction. *Science Advances* **6**, eabb5067 (2020).

130. Mazzocchi, A., Devarasetty, M., Huntwork, R., Soker, S. & Skardal, A. Optimization of collagen type I-hyaluronan hybrid bioink for 3D bioprinted liver microenvironments. *Biofabrication* **11**, 015003 (2018).

131. Lee, A. *et al.* 3D bioprinting of collagen to rebuild components of the human heart. *Science* **365**, 482–487 (2019).

132. Moncal, K. K., Ozbolat, V., Datta, P., Heo, D. N. & Ozbolat, I. T. Thermally-controlled extrusion-based bioprinting of collagen. *J Mater Sci Mater Med* **30**, 55 (2019).

133. Yu, C. *et al.* Scanningless and continuous 3D bioprinting of human tissues with decellularized extracellular matrix. *Biomaterials* **194**, 1–13 (2019).

134. Toprakhisar, B. *et al.* Development of Bioink from Decellularized Tendon Extracellular Matrix for 3D Bioprinting. *Macromol Biosci* **18**, e1800024 (2018).

135. Kim, B. S., Kim, H., Gao, G., Jang, J. & Cho, D.-W. Decellularized extracellular matrix: a step towards the next generation source for bioink manufacturing. *Biofabrication* **9**, 034104 (2017).

136. Nam, S. Y. & Park, S.-H. ECM Based Bioink for Tissue Mimetic 3D Bioprinting. *Adv. Exp. Med. Biol.* **1064**, 335–353 (2018).

137. Lee, H. *et al.* Development of Liver Decellularized Extracellular Matrix Bioink for Three-Dimensional Cell Printing-Based Liver Tissue Engineering. *Biomacromolecules* **18**, 1229–1237 (2017).

138. Bagó, J. R., Pegna, G. J., Okolie, O. & Hingtgen, S. D. Fibrin matrices enhance the transplant and efficacy of cytotoxic stem cell therapy for post-surgical cancer. *Biomaterials* **84**, 42 (2016).

139. Han, J., Kim, D. S., Jang, H., Kim, H.-R. & Kang, H.-W. Bioprinting of three-dimensional dentin–pulp complex with local differentiation of human dental pulp stem cells. *J Tissue Eng* **10**, 204173141984584 (2019).

140. Wang, Z., Lee, S. J., Cheng, H.-J., Yoo, J. J. & Atala, A. 3D bioprinted functional and contractile cardiac tissue constructs. *Acta Biomater* **70**, 48–56 (2018).

141. Wang, X. *et al.* Coaxial extrusion bioprinted shell-core hydrogel microfibers mimic glioma microenvironment and enhance the drug resistance of cancer cells. *Colloids and Surfaces B: Biointerfaces* **171**, 291–299 (2018).

142. Ribeiro, V. P. *et al.* Rapidly responsive silk fibroin hydrogels as an artificial matrix for the programmed tumor cells death. *PLoS ONE* **13**, e0194441 (2018).

143. Wang, Q., Han, G., Yan, S. & Zhang, Q. 3D Printing of Silk Fibroin for Biomedical Applications. *Materials (Basel)* **12**, (2019).

144. Gomez-Roman, N., Stevenson, K., Gilmour, L., Hamilton, G. & Chalmers, A. J. A novel 3D human glioblastoma cell culture system for modeling drug and radiation responses. *Neuro-Oncology* **19**, 229 (2017).

145. Lanzalaco, S. & Armelin, E. Poly(N-isopropylacrylamide) and Copolymers: A Review on Recent Progresses in Biomedical Applications. *Gels* **3**, (2017).

146. Nishiguchi, A. *et al.* 4D Printing of a Light-Driven Soft Actuator with Programmed Printing Density. *ACS Appl Mater Interfaces* **12**, 12176–12185 (2020).

147. Soman, P. *et al.* A Three-dimensional Polymer Scaffolding Material Exhibiting a Zero Poisson's Ratio. *Soft Matter* **8**, 4946–4951 (2012).

148. Soman, P., Lee, J. W., Phadke, A., Varghese, S. & Chen, S. Spatial tuning of negative and positive Poisson's ratio in a multi-layer scaffold. *Acta Biomater* **8**, 2587–2594 (2012).

149. Soman, P. *et al.* Three-dimensional scaffolding to investigate neuronal derivatives of human embryonic stem cells. *Biomed Microdevices* **14**, 829–838 (2012).

150. Avci, N. G., Fan, Y., Dragomir, A., Akay, Y. M. & Akay*, M. Investigating the Influence of HUVECs in the Formation of Glioblastoma Spheroids in High-Throughput Three-Dimensional Microwells. *IEEE Transactions on NanoBioscience* **14**, 790–796 (2015).

151. Fan, Y., Nguyen, D. T., Akay, Y., Xu, F. & Akay, M. Engineering a Brain Cancer Chip for High-throughput Drug Screening. *Sci Rep* **6**, (2016).

152. Li, J., Xing, R., Bai, S. & Yan, X. Recent advances of self-assembling peptide-based hydrogels for biomedical applications. *Soft Matter* **15**, 1704–1715 (2019).

153. Loo, Y. & Hauser, C. A. E. Bioprinting synthetic self-assembling peptide hydrogels for biomedical applications. *Biomed. Mater.* **11**, 014103 (2015).

154. Xia, Y. *et al.* Printable Fluorescent Hydrogels Based on Self-Assembling Peptides. *Sci Rep* **7**, (2017).

CHAPTER 2 Establishing Glioblastoma Extracellular Matrix Heterogeneity

2.1 Abstract

GBM is the most lethal primary brain tumor characterized by high cellular and molecular heterogeneity, hyper-vascularization, and innate drug resistance. Current treatment options include a combination of surgical resection, radiotherapy, and chemotherapy primarily with temozolomide, but the prognosis is poor with an average life expectancy of 15 months. Despite significant research and drug development efforts, therapeutic advances to treat glioblastoma remain stagnant. Cellular components and ECM are the two primary sources of heterogeneity in GBM. One of the major roadblocks in understanding the genetic basis of the cancer and developing new therapies is the lack of physiologically relevant and patient specific GBM tumor models. Here, we develop biomimetic tri-regional GBM models with a tumor region, an acellular ECM region, and an endothelial region – with regional stiffnesses patterned corresponding to the GBM stroma, pathological or normal brain parenchyma, and brain capillaries. Patient-derived GBM cells, human endothelial cells, and hyaluronic acid derivatives are used to generate a species-matched and biochemically relevant microenvironment. This *in vitro* study demonstrates that biophysical cues are involved in various tumor cell behaviors and angiogenic potentials and promote different molecular subtypes of GBM. The stiff models are enriched in the mesenchymal subtype, exhibit diffuse invasion of tumor cells, and induce protruding angiogenesis and higher drug resistance to temozolomide. Meanwhile, the soft models demonstrate enrichment in the classical subtype and support expansive cell growth. The 3D bioprinting technology utilized in our study enables rapid, flexible, and reproducible GBM modeling with biophysical heterogeneity that can be employed by future studies as a tunable system to interrogate GBM disease mechanisms and screen drug compounds.

2.2 Introduction

GBM is the most lethal CNS cancer that has a notable short median patient survival time of 14.6 months.[1] Therapeutic dilemma of GBM results from its genetic heterogeneity, diffusive infiltration, hyper-angiogenesis, and innate resistance to treatments. GBM is characterized by a unique ECM composition, mainly composed of HA, glycosaminoglycans, proteoglycans, and glycoproteins, and lack of collagens.[2] Proteases secreted by cells within the GBM tumor microenvironment (TME) constantly remodel the ECM, leading to altered expression of ECM components as well as changes in biophysical properties such as the stiffness.[2] Dynamic interactions of the ECM with cells regulate GBM initiation, progression, invasion, and treatment responses through both biochemical and biophysical cues. The role of biochemical cues of ECM on tumor cells have been widely studied owing to the availability of ECM-derived materials that can be used for cell culture.[3–5] Biophysical cues such as stiffness, geometry, and topography regulates gene expression and cell behaviors, and cells reciprocally exert forces on ECM and remodel the microenvironment.[6] Mechanoreciprocity involved in these dynamic interactions has been identified to cause tissue stiffening in several cancer types. However, precisely creating the biophysical properties *in vitro* and investigating their roles in GBM are relatively challenging using traditional tissue engineering techniques. Hyper-angiogenesis is another characteristic of GBM that promotes GBM growth and invasion.[7] Biophysical cues of the TME regulate the abnormal tumor angiogenesis, and anti-angiogenesis treatment leads to changes in GBM stiffness.[8,9] However, models for investigating the angiogenesis activity of endothelial cells and GBM cell responses to vascularization in a stiffness-matched model has not been developed.

In vitro 3D models have gained popularity in investigating the cellular crosstalk and cell-ECM interactions due to their improved biomimicry compared to conventional models. Organoids as a self-assembled 3D model system have been explored for various cancer types, including

pancreatic cancer, bladder cancer, as well as GBM.[10–12] Organoids generally better retain the tumor heterogeneity and transcriptional signatures compared to the traditional 2D culture. However, organoids are limited by innate variations and limited control over the structures due to the self-assembly process. Among various biofabrication technologies, 3D bioprinting enables cell-encapsulation in native ECM-derived biomaterials with defined architectures and matrix properties, and thus is increasingly employed for modeling complex cellular tissues and investigating the role of ECM in cancer progression.[13] 3D-printed models have successfully modeled the cellular heterogeneity, a characteristic of many cancer types including GBM, by creating a stromal layer surrounding a tumor zone, for the investigation of stromal impacts on tumor development and treatment responses.[14–16] In addition to cellular components, ECM is another critical aspect of the tumor microenvironment. Previously, polyethylene glycol (PEG)-based or HA-based hydrogels with different stiffnesses have been developed to evaluate stiffness impact on GBM cell growth.[17,18] PEG-HA composite hydrogels with tunable stiffnesses independent of the HA concentration have been employed for 3D culture of GBM cells.[19] Most studies either investigated ECM biophysical impacts on GBM using hydrogels with a bulk stiffness or relied on synthetic materials to modulate the stiffnesses.[17] Use of synthetic materials reduces the biomimicry of models due to the lack of proper biochemical cues. Stiffnesses of the tumor stroma, brain parenchyma, and brain capillaries are not homogeneous *in vivo*, thus hydrogels with bulk mechanical properties may also be insufficient to recapitulate the TME.[17,20–23] Investigating the biophysical aspects of ECM requires 3D matrices that can faithfully recapitulate native architectures as well as mechanical properties. Digital light processing (DLP)-based bioprinting is a rapid biofabrication technique compatible with various light-sensitive biomaterials.[24] Several tissue models and cancer models have been developed using this technology and ECM-derived

biomaterials.[15,24–26] Orthogonal control of biophysical properties and biochemical cues have also been achieved using DLP-based printing and ECM-derived materials, making the technology ideal for the investigation of biophysical impacts on GBM development within a biomimetic ECM-based model.[27,28]

We hereby developed the first species-matched *in vitro* models that recapitulate the biophysical heterogeneity of GBM – with regionally varied stiffnesses corresponding to GBM stroma, pathological or healthy brain parenchyma, and brain capillaries – based on patient-derived cells and HA derivatives via DLP-based bioprinting. HA-based biomaterial and patient-derived cells enable the evaluation of biophysical impacts on GBM in a biochemically relevant and species-matched microenvironment. By adjusting printing parameters and the concentrations of the biomaterials, we were able to modulate the stiffness of three distinct regions in 3D-printed GBM models with a constant HA concentration. Modeling the biophysical heterogeneity potentially enhanced the biomimicry of models. Changes associated with tumorigenesis, including cell morphologies, invasion behaviors, gene expressions, angiogenic potentials, and drug responses rapidly occurred within two weeks in the 3D-printed GBM models with different stiffness conditions. The stiff ECM microenvironment induced the mesenchymal phenotype associated with recurrence and poorest treatment outcomes in patients. The soft ECM microenvironment promoted rapid cell proliferation and supported the expansion of cells with the classical phenotype. Endothelial cells incorporated in the 3D-printed GBM models also demonstrated different modes of growth and interaction, such as protruding morphologies in the stiff models and expansive growth in the soft models. Endothelial co-culture also induced

differential drug responses in the GBM cells in the 3D-printed models, suggesting their potential roles in GBM drug resistance.

2.3 Results

2.3.1 3D bioprinted GBM models with regionally varied biophysical properties

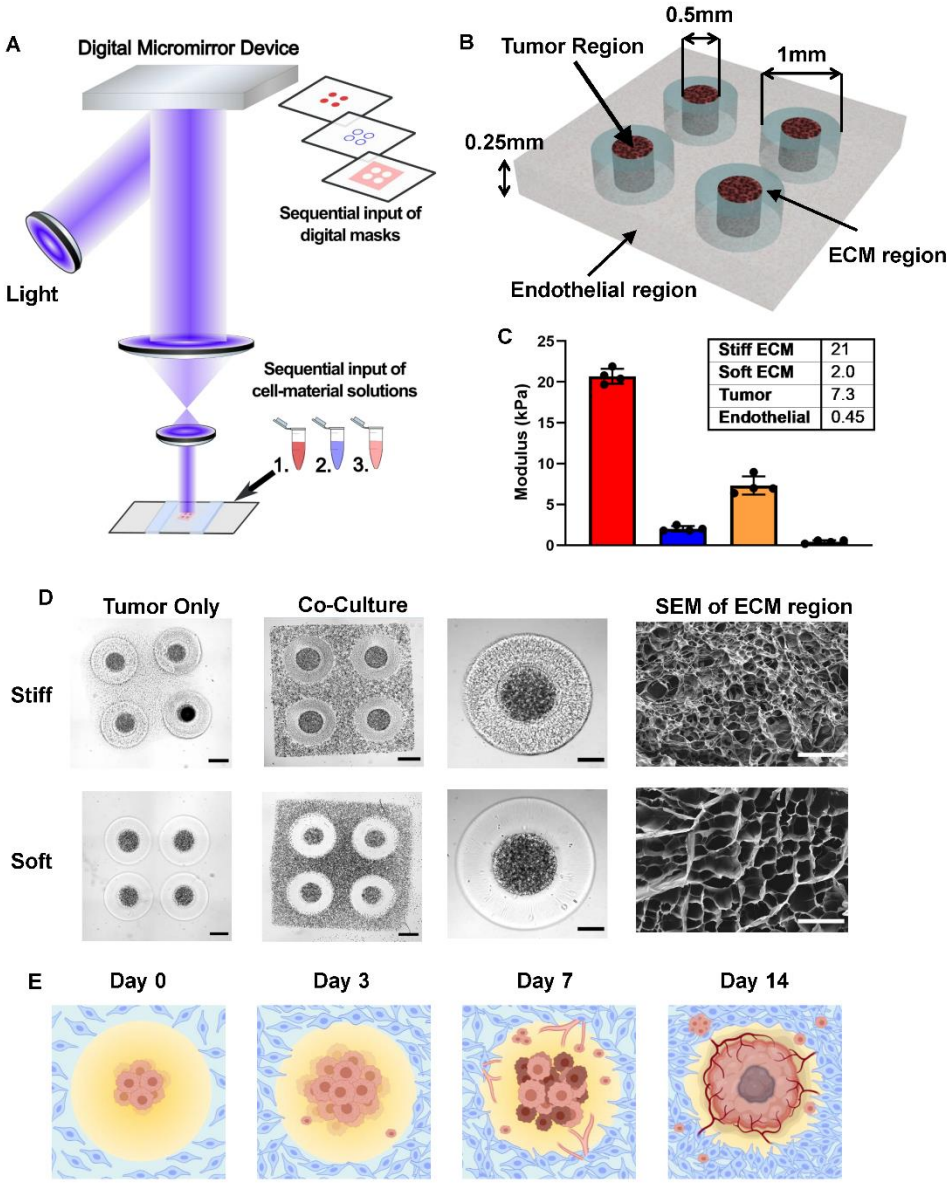

Figure 2.1 3D-bioprinted GBM models with regionally varied biophysical properties.

GBM tumor cells respond to the complex ECM cues and constantly remodel the ECM as cancer progresses. The remodeled ECM affects both the tumor survival and progression, and other

critical stromal cell events such as angiogenesis by the endothelial cells. To recapitulate the spatially inhomogeneous ECM microenvironment and interrogate how ECM heterogeneity impacts on GBM development and endothelial cell growth, we utilized our DLP-based 3D bioprinting system and brain tumor-specific ECM-derived bioinks consisted of glycidyl methacrylate hyaluronic acid (GMHA) and gelatin GelMA, to create four different models: the tumor-only stiff model, the tumor-only soft model, the coculture stiff model, and the coculture soft model (Figure 2.1A). The 3D bioprinting system utilized a digital micromirror device chip consisting of over a million independently controlled micromirrors and a light source to project predesigned patterns on the bioink, allowing rapid polymerization of each region with 20-30 seconds of light exposure. A complete multi-stiffness GBM model could be created within 2 minutes. Considering the diffusion limit of nutrition and oxygen, the models were designed with a thickness of 250 μm. For each model, four initial tumor regions were generated with GBM cells with a diameter of 500 μm, surrounded by a donut-shape acellular ECM region with the ring width of 500 μm. For coculture models, an additional endothelial region was printed with human umbilical vascular endothelial cells (HUVECs) to encompass the tumor and ECM regions (Figure 2.1B). Matrix stiffness of the tumor core and the endothelial regions was designed to mimic that of GBM patient tissues (7 kPa) and normal brain tissues (0.45 kPa).[21] Encapsulating the GBM cells in a pathologically stiffened matrix was to mimic their physiological conditions and promote cell growth. Both the tumor cells and endothelial cells demonstrated high viability in their corresponding hydrogel environment through one week of culture.[20–23] Clinical measurements indicated that the matrix stiffness could increase up to 26 kPa in GBM tissues.[17,22,29,30] For the ECM regions, two different stiffnesses, 21 kPa (hereby referred to as stiff models) and 2 kPa (referred to as soft models), were designed to mimic the GBM tissue stiffness and healthy brain

stiffness (Figure 2.1C). Leveraging the GelMA concentration and printing parameters, we were able to obtain desired stiffness for each region while keeping the HA content constant across all models. Keeping a constant HA concentration avoided potential impacts on the tumor cells due to the difference in the amount of biochemical cues provided by HA. For all three ranges, hydrogel stiffnesses remained stable through one week of incubation at 37 ºC and 5% CO_2, the same condition used for all samples. Difference in the appearance of stiff and soft ECM hydrogels was observed using bright field imaging or scanning electron microscopy (SEM) (Figure 2.1D). The pore sizes of the stiff ECM were significantly smaller than the pore sizes of the soft ECM. We further used these 3D-printed GBM models with regionally varied mechanical properties to perform various assessments and studies, including gene expressions, drug responses, tumor cell migration behaviors, and angiogenesis activities, occurred in response to the biophysical cues and culture conditions (Figure 2.1E).

2.3.2 3D models have distinct transcriptional profiles compared to sphere culture

Traditional cell culture methods including 2D culture and sphere culture have been extensively used for in vitro expansion and maintenance of GBM cells. Patient-derived cells cultured as spheres in serum-free conditions were enriched for GBM stem cells that better replicate the transcriptional signatures of the original tumor tissue than cell line-based 2D cultures. However, studies have demonstrated that cells maintained in traditional culture conditions still display distinct transcriptional profiles and cellular dependencies compared to primary tissue, 3D culture, or xenografts.[15,31]

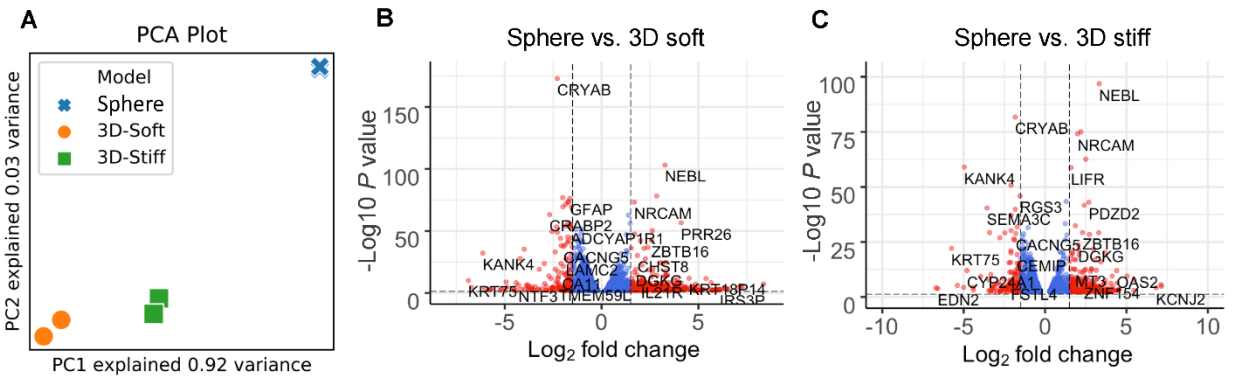

Figure 2.2 Distinct transcriptional profiles between the GBM sphere culture and 3D models.

Global transcriptome profiling was performed through RNA extraction and RNA sequencing (RNAseq) on TS576 GBM cells cultured as spheres and isolated from the tumor-only 3D soft and the tumor-only 3D stiff conditions. We first interrogated the difference among the sphere culture and the two 3D conditions to investigate the impact of 3D culture and ECM cues on the transcriptional signature of tumor cells. Principal component analysis revealed that the sphere culture had a drastically different transcriptional profile compared to either 3D conditions, while the difference between the two 3D conditions was to a lesser extent (Figure 2.2A). A few protein-coding cancer-related genes or prognostic genes were significantly upregulated over 16 folds in both 3D conditions, such as SLCO2A1, TCN1, and NTN4. Overexpression of the solute carrier organic anion transporter SLCO2A1 has been observed in GBM cells compared to normal brain tissues, promoting colon cancer tumorigenesis and mediating lung cancer invasion through the PI3K/AKT/mTOR pathway.[32–34] TCN1 encodes vitamin B12 binding proteins and is a prognostic marker in renal cancer. NTN4 promotes GBM proliferation and is associated with TMZ resistance.[35,36] Genes significantly downregulated in both 3D conditions but enriched in sphere cultures included CYP24A1, DIRAS2, KANK4, KRT75, and PRSS35 (Figure 2.2B-C).

We performed a gene ontology (GO) enrichment analysis with the RNAseq results of sphere culture and the 3D tumor-only models to investigate the changes in biological processes

and molecular functions of the tumor cells in different culture conditions. Cell-cell adhesion via plasma-membrane adhesion molecules was over-represented in both 3D conditions compared to the sphere culture, demonstrating the biomimetic ECM materials used for printing promoted cell adhesion and cellular crosstalk. GO terms about DNA replication, cell cycle regulation, and cell division, were significantly over-represented in the 3D soft model compared to the sphere culture. Enriched GO terms involved in cellular component organizations such as chromosome segregation, organelle fission, microtubule cytoskeleton organization, and spindle organization were identified in the 3D soft model. In addition, positive regulation of cell cycles, G1/S phase transition and G2/M phase transition, suggests an enhanced proliferation of tumor cells in the 3D soft model compared to the sphere culture. Highly enriched term of exocrine system development implied that cell differentiation probably occurred in the 3D soft condition. Gene set enrichment analysis (GSEA) revealed that compared to the 3D soft condition, sphere cultured cells express enriched gene sets involved in STAT pathway, chemotaxis, autophagosome, and cell differentiation.

Cells in the 3D stiff condition also demonstrated distinctly enriched GO terms compared to sphere cultures. The protein kinase C (PKC) activity is highly enriched in the 3D stiff condition compared to the sphere control, and previous studies have demonstrated that the PKC pathway is involved in the aggressive phenotype of GBM.[37] Cell adhesion mediated by integrin, cell-substrate adhesion, and extracellular structure organization were over-represented by the cells in the stiff condition. GSEA comparing the expression of cells cultured as spheres and in the 3D stiff condition revealed that sphere cultured cells expressed highly enriched cellular organization and modification activities including DNA repair and histone modifications. Sphere culture were also enriched in pathways related to signal transduction and metabolism, including NGF-stimulated

transcription, MAPK signaling pathways, oxidative phosphorylation, respiratory electron transport, complex I biogenesis, response of EIF2AK4 to amino acid deficiency, eukaryotic translation elongation, and KEGG ribosome related pathway.

The changes in gene expression and subsequent functional changes of cells cultured in the 3D models compared to the control are the combined results of the dimensionality, biochemical cues and mechanical cues of the ECM-like matrix, and cellular crosstalk enabled by 3D modeling. While in both 3D soft and 3D stiff conditions, biomimetic HA-based hydrogel were used to fabricate the models, genes related to cell-ECM interactions were more enriched in the stiff condition, suggesting that the stiff microenvironment might have enhanced the cellular response to the ECM-derived cues.

2.3.3 Stiff model promotes hypoxia and tumorigenicity signature in GBM

We further interrogated the transcriptional profiles of the GBM cells encapsulated in the 3D stiff and 3D soft models. The amount of HA in the two models was identical so that we could evaluate the effects of the biophysical cues from the ECM on the tumor development. Gene sets related to hypoxia conditions, cancer invasiveness, E-cadherin loss-induced metastasis, and responses to external stimulations including interferons, inflammation, ECM, and cell apoptosis were significantly enriched in the stiff model (Figure 2.3A-B). A cut-off of fold change greater than 2 and false discovery rate (FDR) less than 0.05 was used to identify the most differentially expressed genes (DEGs) in either 3D tumor-only condition.

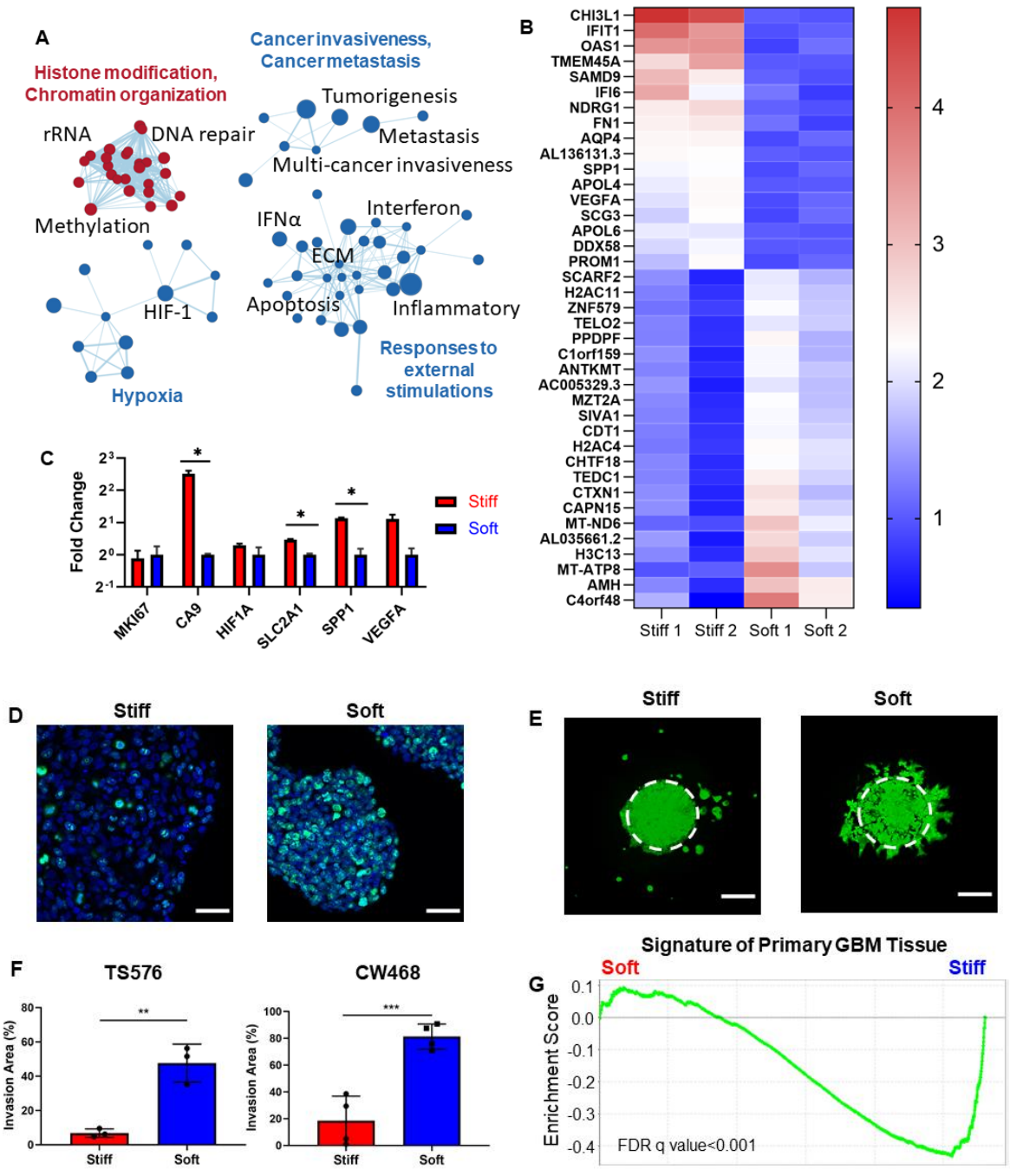

Figure 2.3 Biophysical patterning induced distinct transcriptional profiles and invasion patterns of GBM cells.

Genes significantly elevated by the 3D stiff condition included CHI3L1, IFIT1, OAS1, TMEM45A, SAMD9, IFI6, NDRG1, FN1, AQP4, AL136131.3, SPP1, APOL4, VEGFA, SCG3, APOL6, DDX58, and PROM1. High expression of CHI3L1 and SAMD9 has been identified to be

negatively correlated with GBM patient survival time.[38,39] TMEM45A and NDRG1 are involved in hypoxia-associated chemoresistance, and the knockdown of TMEM45A reduces glioma proliferation and invasion.[40–42] FN1 is highly upregulated in GBM and involved in the adhesion, growth, angiogenesis, and recurrence of GBM.[43] GBM expresses higher level of AQP4 compared to low-grade gliomas, and AQP4 with its highest water flux capacity in the CNS is potentially associated with tumor edema, migration, and proliferation.[44] Long non-coding RNA (lncRNA) genes AL136131.3, an antisense to VEGFA, was concordantly upregulated in the stiff condition with the angiogenesis markers VEGFA and SPP1. Genes encoding apolipoproteins including APOL4 and APOL6 were also significantly upregulated in the stiff condition. IFIT1, OAS1, IFI6, and DDX58 are associated with the interferon (IFN) signaling pathways which has been suggested to be involved in the immune escape of GBM.[45] CD133 (or RPOM1) upregulated in the stiff condition is essential for the maintenance of GBM stem cells.[46]

Gene sets related to cell cycle regulation, such as phase transition, DNA synthesis, chromosome organization, transcriptional regulation, and DNA repair were upregulated in the soft condition, more specifically, the most upregulated genes in the soft models included AMH, MT-ATP8, H3C13, MT-ND6, CAPN15, CTXN1, TEDC1, CHTF18, H2AC4, CDT1, SIVA1, MZT2A, ANTKMT, PPDPF, TELO2, ZNF579, H2AC11, SCARF2. AMH belongs to the transforming growth factor β (TGFβ) superfamily which plays a role in the initiation and progression of gliomas.[47] MT-ATP8 and MT-ND6 are mitochondrially encoded genes, and ANTKMT regulates mitochondrial respiration. Various cell cycle related genes were enriched. H3C13, H2AC4, and H2AC11 are histone genes whose upregulation often occur during the S phase of the cell cycle. Genes associated with biogenesis, such DNA replication, DNA synthesis, DNA repair, or spindle organization, were also upregulated, including TEDC1, CHTF18, CDT1,

SIVA1, MZT2A, and TELO2. CAPN15, CTXN1, and ZNF579 are involved in transcriptional regulations or cell signaling. High expression of PPDPF correlates with cancer progression and tumor size in hepatocellular carcinoma.[48] SCARF2 upregulated in the soft model has been suggested as a risk gene for glioma.[49]

A hypoxic microenvironment has been shown to promote cell stemness, cancer invasiveness, endothelial-mesenchymal transition, and cell-cycle arrest.[50] Hypoxia related genes including CA IX, HIF1-α, SLC2A1 (encoding glucose transporter 1 protein), and hypoxia-associated angiogenesis markers VEGFA and SPP1 were upregulated in the stiff condition (Figure 2.3C). While mRNA expression of the proliferation marker MKI67 of cells from the two conditions showed no significant difference, immunofluorescence (IF) staining revealed that more KI67 positive cells were present in the soft model, suggesting that post translational regulations may be involved (Figure 2.3D). In addition, IF staining showed that the stiff model better maintained the overall stemness of the TS576 cells, while the SOX2+ tumor cells were mainly located on the invasive edge of the tumor core in the soft model. The astrocytic differentiation marker glial fibrillary acidic protein (GFAP) was observed in the soft model but not in the stiff mode.

2.3.4 3D models induce different GBM invasion patterns and transcriptional subtypes

Using green fluorescent protein labeled tumor cells, the migration patterns of GBM cells were imaged on day 7. Distinct modes of invasion were observed (Figure 2.3E). GBM cells diffusively migrated out from the original region as single cells or small clusters and proliferated with a rounded morphology at new locations in the stiff model. Diffusive invasion is a characteristic of GBM making it difficult for complete surgical removal. The cells in the soft model expanded from their original location with protrusions, forming invasive margins as observed in a GBM mouse xenograft model.[51] Multiple invasion patterns have been observed in xenografts, in

vitro cell culture, and biopsies, such as single cell invasion, cluster invasion, and expansive-growth, demonstrating the highly heterogeneous and dynamic behavior of GBM.[51,52] The area of invasion in the soft models was 7 folds and 4.4 folds higher than in the stiff models for TS576 cells and CW468 cells, respectively, consistent with the KI67 staining (Figure 2.3F).

We next generated a "primary GBM tissue" gene set with a core set of genes upregulated in GBM surgical specimens compared to sphere cultured GBM cells *in vitro*. Principle component analysis demonstrated that the sphere culture had a distinct transcriptome profile from primary GBM tissues. TS576 cells isolated from the stiff model were highly enriched with the primary GBM tissue signatures when compared to TS576 cells isolated from the soft model (Figure 2.3G), indicating that the stiff model transformed the cells to a more clinically relevant state. Bulk transcriptional profiling of the primary GBM tissue from The Cancer Genome Atlas (TCGA) identified three major subtypes of GBM, the proneural, the mesenchymal, and the classical subtype, each enriched for different genetic alterations.[53] GSEA revealed that gene sets related to epithelial-mesenchymal transition (EMT) and mesenchymal signatures were enriched in the stiff condition. Expression of genes associated with the mesenchymal subtype such as FN1 and CHI3L1 were 2-fold and 4-fold higher in the stiff model than in the soft model. PDGFRA commonly altered in the proneural subtype had a higher expression level in the stiff model, while EGFR related genes commonly amplified in the classical subtype showed higher expressions in the soft model. These findings suggested that the stiff model could better model the mesenchymal subtype and proneural subtype, while the soft model was more suitable for modeling the classical subtype. The stiffness patterned GBM model enables us to create different GBM situations *in vitro*.

2.3.5 Endothelial cells exhibit different growth patterns and angiogenic events

To further investigate the crosstalk between the GBM cells and endothelial cells, we incorporated HUVEC into the 3D-printed multi-stiffness models. The endothelial region and the

tumor cores were separated by the ECM regions with either the stiff or the soft type hydrogels. The spatial separation allowed investigation of paracrine signaling-induced endothelial cell growth and migration towards the tumor core as well as the tumor cell migration. In both 3D co-culture models, migration of HUVEC towards GBM cells were observed. In the stiff model, the migrated CD31+ HUVECs exhibited a sprouted blood-vessel like morphology and were in close contact with the SOX2+ GBM cells (Figure 2.4A).

In the soft model, the HUVECs exhibited expansive-growth morphology without visible sprouting. We performed a quantitative real-time PCR (qPCR) on tumor cells isolated from all our 3D printed models and sphere cultures. Angiogenic markers SPP1 and VEGFA were upregulated in all 3D models, and significantly enriched by the stiff culture condition or the co-culture condition (Figure 2.4B).

More specifically, in the tumor-only 3D models, cells expressed significantly higher VEGFA in the stiff model than in the soft model; comparing the tumor-only models and the co-culture models, the co-culture condition significantly increased the expression of VEGFA in the tumor cells in both the soft and the stiff conditions. Tumor cells in the stiff co-culture condition expressed the highest level of VEGFA and SPP1. Prior studies showed that VEGFA and other signals generated by hypoxic tumor cells within the pseudo-palisades near necrotic tumor core could trigger sprouting angiogenesis events near the tumor-parenchyma interface, consistent with our observation of more active sprouting events in the 3D stiff co-culture model.[54,55]

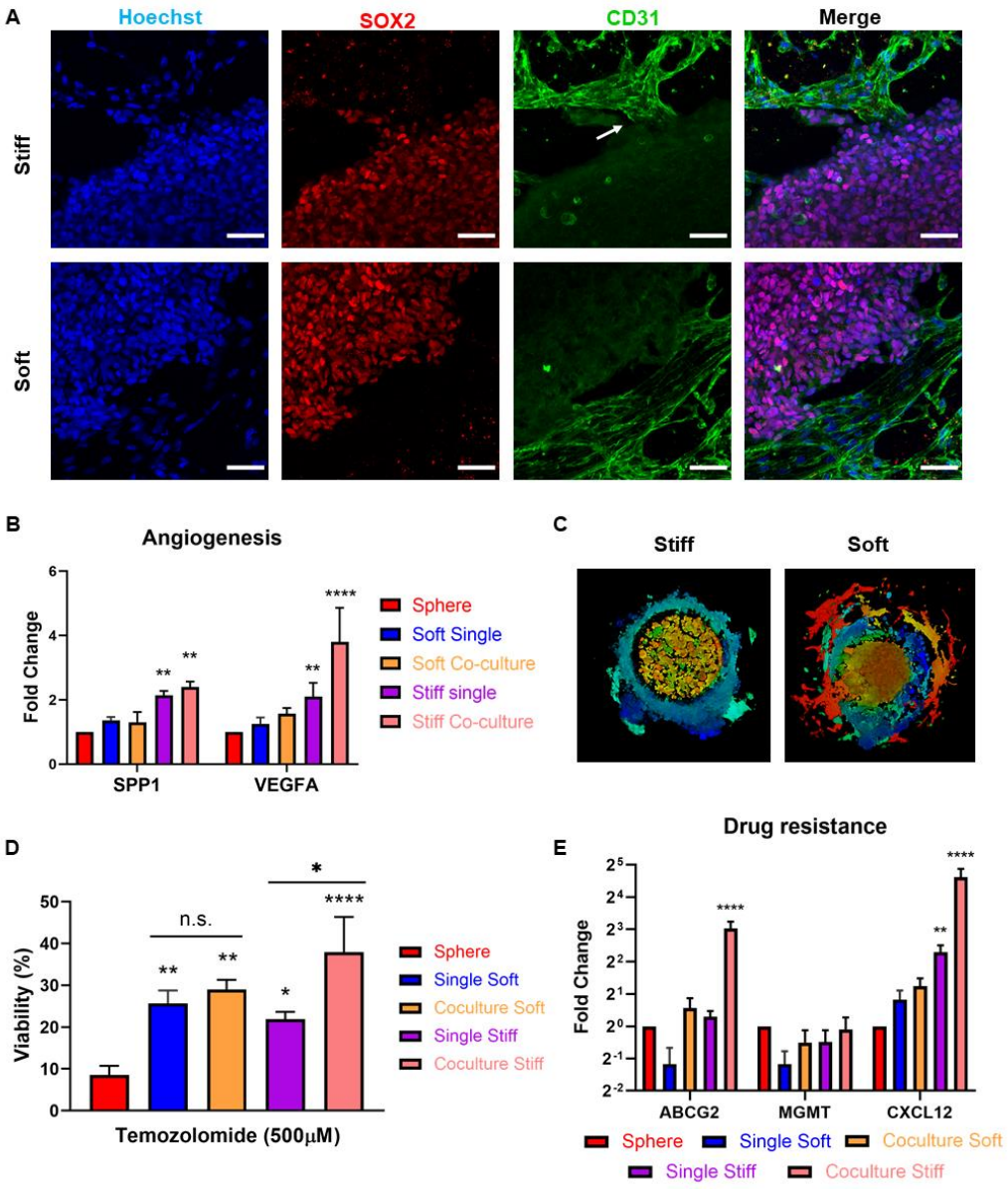

Figure 2.4 Stiff condition induced sprouting angiogenesis of endothelial cells and enhanced drug resistance of GBM cells.

2.3.6 GBM-endothelial crosstalk enhances tumor invasion and drug resistance

We then interrogated the impact of co-culture condition on GBM cell behaviors and functions. Similar to their tumor-only 3D counterparts, GBM cells in the co-culture models also demonstrated different invasion patterns. Tumor cells expanded with a fibroblastic morphology in the soft co-culture model, and more rounded morphology in the stiff model (Figure 2.4C). The co-

culture condition promoted CW468 invasion into the ECM regions in both the soft and stiff models and promoted invasion of TS576 cells only in the stiff condition. The observed difference may be resulted from the innate heterogeneity of GBM cells. SOX2 was expressed by most tumor cells in the stiff condition but mainly by the cells on the outer rim of the tumor region in the soft condition. The expression of differentiation marker GFAP was significantly elevated in the soft condition compared to the stiff condition. The IF staining results suggested that the stiff co-culture condition promoted the stemness of tumor cells and the soft co-culture condition promoted cell differentiation.

All 3D-bioprinted models demonstrated enhanced drug resistance of tumor cells to TMZ compared to sphere cultured cells (Figure 2.4D). IC_{50} of TMZ on sphere cultured TS576 cells was measured to be 30 μM, but the dosage was ineffective in the 3D models. For fair comparison, all conditions were treated with 500 μM of TMZ for 6 days. No significant difference in the viability of tumor cells were detected in the tumor-only stiff or soft models. The co-culture condition significantly increased the viability of TS576 cells to TMZ treatment in the stiff models but had no significant impact on cell viability in the soft models. We have previously observed sprouting events of endothelial cells in the stiff models. The sprouting endothelial cells were in close contact with a cluster of SOX2+ tumor cells, potentially forming a perivascular niche near the invading edge of the tumor zone. The perivascular niche has been reported to enrich cancer stem cells that are highly drug resistant.[56] It is possible that the interaction between endothelial cells and tumor cells in the stiff model have enriched the drug resistant population more than that in the soft model, leading to higher viability of tumor cells after TMZ treatment. To confirm that differential drug responses were not a result of diffusion kinetics of drugs into the 3D hydrogels, we simulated the diffusion of drugs with fluorescently labeled Dextran molecules. After 30 minutes of incubation,

the fluorescence signals reached plateau in both the stiff hydrogel and the soft hydrogel and demonstrated no statistical significance in the signal intensities. QPCR analysis revealed that drug resistance related genes such as ABCG2 and CXCL12 were upregulated 8-fold and 24-fold, respectively, in the stiff co-culture condition (Figure 2.4E), consistent with the TMZ treatment responses.

2.4 Conclusion

We have developed biochemically and biophysically relevant GBM models with stiffness patterning in HA-rich matrix for investigation of behaviors and interactions of tumor cell and endothelial cells in a heterogeneous and biomimetic microenvironment. Tumor regions and endothelial regions were designed to have stiffness resembling their native states. Two stiffness conditions of the ECM region specifically designed to mimic GBM-remodeled stroma or healthy brain parenchyma were printed between the tumor region and the endothelial region, resulting in differential tumor cell growth and behaviors. While cell proliferation and expansion occurred rapidly in the soft models, hypoxia, stemness, and angiogenic potentials related to malignant phenotypes were enhanced in the stiff models. Tumor cells invade the ECM regions with distinct morphologies and patterns in the two-stiffness microenvironment. The stiff condition demonstrated a single cell diffuse invasion pattern, a characteristic of GBM precluding complete surgical removal, while the soft condition exhibited an expansive growth pattern. Both invasion patterns have been previously observed for GBM cells, suggesting that our stiffness-patterned models may be suitable for modeling different states of GBM development. Gene set enrichment analysis suggested that the stiff condition recapitulated the primary GBM tissue signatures and was enriched in gene sets related to the mesenchymal and proneural subtypes. Meanwhile, GBM

cells in the soft condition were more enriched in gene sets related to the classical subtype, indicating that the two types of stiffness are suitable for modeling different subtypes.

Vascularization is a characteristic feature of GBM that promotes tumor growth and facilitates tumor invasion. The incorporation of HUVECs into the stiffness-patterned model allowed us to observe different endothelial cell growth patterns and potential angiogenic events in two different stiffness conditions, as well as altered tumor invasion patterns and drug responses in the presence of endothelial cells. Sprouting and proliferation of endothelial cells coordinate to mediate blood vessel formation.[54,57] While proliferation of HUVECs was observed in the soft models, proliferation and sprouting were both observed in the stiff models. The gene expression revealed that tumor cells in the stiff model expressed high angiogenic markers, consistent with the observation of sprouting events in the stiff models. The soft condition in general promoted cell proliferation, demonstrated by the larger invasion area of tumor cells and the proliferation of endothelial cells. Moreover, TMZ treatment on all models and a sphere culture control demonstrated that the stiff co-culture model had the highest tumor cell viability, suggesting that the stiff condition as well as co-culture with endothelial cells enhanced the drug resistance of GBM. Many cancer drugs including TMZ induce cell cycle arrest and block cell division, thus are more effective on proliferating cells, consistent with the higher TMZ sensitivity of cells in the soft models compared to the stiff models.

To conclude, the tri-regional stiffness-patterned GBM models presented in this work are the first to incorporate physiologically relevant biophysical heterogeneity of GBM with biochemically relevant ECM materials. The regional stiffnesses better recapitulate the native environments and potentially favor more biomimetic cell-ECM and cellular interactions. Transcriptional profiling has demonstrated the potential of using these models to investigate

different subtypes of GBM as well as different stages of GBM. Flexibility of the DLP-based bioprinting process and versatile material selection allow orthogonal modulation of biophysical properties and biochemical characteristics. The stiffness patterning can also be applied to future models to study the biophysical impacts on other tumor-stromal interactions, such as macrophages and astrocytes, abundant in the GBM microenvironment.

2.5 Experimental Section/Methods

All studies were conducted in accordance with approved IRB protocols by the University of California, San Diego. All animal work was approved by the Institutional Review Board at the University of California, San Diego and was performed in accordance with Institutional Animal Care and Use Committee guidelines.

2.5.1 GMHA and GelMA synthesis and characterization

GMHA was synthesized using 200 kDa hyaluronic acid (HA, Lifecore Biomedicals) and GelMA using gelatin from porcine skin (Sigma-Aldrich) with methods described previously.[58,59] Briefly, HA was dissolved in a 1:1 water and acetone solution at room temperature overnight. On the next day, triethylamine and glycidyl methacrylate was sequentially added to the mixture and stirred overnight. GMHA was precipitated with acetone and re-dissolve in de-ionized water. The resuspended GMHA solution was collected in 12-14 kDa rated dialyzer tubes and dialyzed at room temperature for 12 hours, with water replacement every 3 hours. For the synthesis of GelMA, gelatin was first dissolved in a 0.25M carbonate-bicarbonate buffer solution at 50 °C. For each gram of gelatin, 0.1ml methacrylic anhydride was added dropwise to the gelatin solution and stirred for 1 hour at 50 °C. The solution is then dialyzed at 42°C for a week. After dialysis, both GMHA and GelMA solutions were collected in 50 mL tubes to be frozen overnight at −80 °C and lyophilized. Freeze-dried GelMA and GMHA were stored at −80 °C before reconstitution. To

prepare the printing biomaterials, GelMA was reconstituted to a stock solution of 20% (w/v) and GMHA to a stock solution of 4% (w/v). All stock solutions were sterilized using filters (Millipore) with 0.22 μm pore size and stored at 4°C before use. Proton nuclear magnetic resonance (^{1}H NMR, Bruker) was used to characterize the degree of substitution (methacrylation) of GelMA and GMHA.

2.5.2 Cell culture

Human patient derived glioblastoma stem cells (TS576) were obtained from Dr. Frank Furnari Lab at the University of California, San Diego (UCSD) and cultured as described previously.[60,61] TS576 cells were cultured in DMEM/F12 medium containing 1% (v/v) B27 supplement without vitamin A, 20 ng/mL EGF, 10 ng/mL bFGF, and 100 IU/mL penicillin/streptomycin (P/S) at 37ºC. CW468 cells obtained from Dr. Jeremy Rich Lab at UCSD were cultured in serum-free Neurobasal medium supplemented with 2% (v/v) B27 supplement without vitamin A, 10 ng/mL basic human fibroblast growth factor, 10 ng/mL human epidermal growth factor, and 1% P/S. HUVECs were cultured in EGM-2 (Lonza) complete medium supplemented with 1% P/S.

2.5.3 3D printing of the GBM models

Before printing, TS576 cells were digested with Accutase (Stemcell Technology), and HUVECs were digested with 0.05% Trypsin-EDTA (Gibco). For all 3D samples, the cell suspension solution for the tumor region was resuspended to 10 x 10^7 cells/mL of TS576s. For the co-culture model, the cell suspension solution for the endothelial region was resuspended to 5 x 10^7 cells/mL of HUVECs. The cell suspension was then prepared as 10 μL aliquots and stored on ice before printing. Bioinks for each region was prepared with concentrations in **Table 2.1**. For tumor and endothelial regions, the bioinks were prepared with twice of their desired final

concentrations (final biomaterial concentrations of these two regions are included in the parentheses).

Table 2.1 Material composition of different regions.

Region	GelMA (w/v)	GMHA (w/v)
Tumor region	10% (5%)	2% (1%)
Endothelial region	5% (2.5%)	1% (0.5%)
Stiff ECM	10%	1%
Soft ECM	5%	1%

The bioinks were stored on heat block at 37 °C and covered with foil to avoid light exposure. Bioinks for the tumor and endothelial regions were mixed with the corresponding cell suspension solution at 1:1 ratio immediately before printing to maximize cell viability. Bioinks for the ECM region was directly used for printing with no further dilution.

A customized DLP-based 3D bioprinting system was used for the multicomponent printing process. The primary components of the 3D bioprinting system are a digital micromirror device (DMD) chip (Texas Instruments), optics for light control, a printing stage with motion controller (Newport), and a light source (Hamamatsu). Specialized computer software was developed to coordinate the loaded patterns, light exposure time, and stage movement. A specialized printing apparatus was used to precisely control the thickness of the printed structure. After loading the cell-biomaterial mixture onto the printing stage, light was switched on with a set of exposure times. The exposure time was 20 seconds for the soft ECM and 25 seconds for the endothelial region. The exposure time was 25 seconds for the tumor region and 30 seconds for the stiff ECM. Printed constructs were rinsed with DPBS supplemented with 1% P/S and 0.2% Normocin (Invitrogen) and cultured in maintenance medium at 37 °C. The maintenance medium composed of 50% of complete TS576 medium and 50% EGM-2.

2.5.4 Mechanical testing

MicroSquisher (CellScale) was used to measure the compressive modulus of the printed samples. For each prepolymer mixture, pillars with 250 μm in diameter and 250 μm in height were printed with the same printing setup used for the tumor models. Pillars were stored at 37 °C before measurement to mimic the culture condition. Mechanical testing was performed on Day 1, 3, and 7 to evaluate the stability of printed constructs. For measurement on the MicroSquisher, stainless steel beams and platens were used to consecutively compress the constructs at 10% displacement of their height for three times. The last measurement is used for analysis. Compressive modulus was generated using customized MATLAB scripts from the force and displacement data.

2.5.5 Scanning electron microscopy (SEM)

Micron-scale patterns of the printed constructs were imaged using Zeiss Sigma 500. Samples were prepared using a chemical dehydration protocol optimized for printed hydrogels. Briefly, samples were fixed with 2.5% glutaraldehyde for 1 hour at room temperature and overnight at 4°C. Then the samples were rinsed with DPBS and sequentially soaked in 70%, 90%, 95%, and 100% ethanol. After replacing the 100% ethanol solution for 3 times, the samples were transferred to hexamethyldisilazane (HDMS):EtOH (1:2) for 15 minutes, HDMS:EtOH (2:1) for another 15 minutes, and eventually 100% HDMS for 15 minutes. The samples were left in a chemical hood overnight. Right before SEM imaging, the chemically dried samples were coated with iridium using a sputter coater (Emitech).

2.5.6 Immunofluorescence staining and image acquisition

3D bioprinted constructs were rinsed with DPBS for three times and fixed with 4% paraformaldehyde for 1 hour at room temperature. The block/permeabilization solution was prepared by dissolving 5% (w/v) bovine serum albumin (BSA, Gemini Bio-Products) and 0.1%

Triton X-100 (Promega) in PBS and filtered after fully dissolved. Fixed samples were blocked/permeabilized for 1 hour at room temperature on a shaker at 100 rpm.

Primary antibodies (**Table 2.2**) were diluted in PBS, and samples were incubated in primary antibody solution overnight at 4 ℃. Samples were rinsed three times using DPBS with 0.05% Tween 20 (PBST) at 100 rpm at room temperature. Secondary Alexa Fluor-conjugated antibodies (1:200; Abcam) and Hoechst 33342 (1:1000; Life Technologies) were diluted in DPBS with 3% (w/v) BSA. Samples were incubated in secondary antibody and counterstain solutions in dark for 1 hour at room temperature. Samples were rinsed three times with PBST after secondary incubation. Before imaging, the samples were soaked in a 0.05% sodium azide (Alfa Aesar) solution and stored at 4 ℃ in dark. A confocal microscope (Leica SP8) was used for image acquisition with consistent settings for each primary antibody. Fluorescence images of EGFP labeled cells were also acquired using the confocal microscope.

Table 2.2 Antibodies used for immunofluorescence staining.

Primary Antibody	Species	Dilution	Manufacturer
SOX2	rabbit anti human	1:100	Abcam 97959
GFAP	mouse anti human	1:100	Millipore Sigma G3893
CD31	mouse anti human	1:100	Abcam 24590
Ki67	rabbit anti human	1:100	Abcam ab16667

2.5.7 RNA isolation and quantitative reverse transcription polymerase chain reaction (RT-qPCR)

For 3D single cell culture models, TS576 cells were retrieved from printed constructs by dissociating the hydrogel with collagenase type II (Sigma-Aldrich). For 3D co-culture models, endothelial layers were mechanically removed before using collagenase II to retrieve tumor cells. TRIzol reagent (Life Technologies) was mixed with tumor cells isolated from 3D models or their

sphere culture counterparts to prepare cell lysates. Total RNA of each sample was extracted using the Direct-zol RNA MiniPrep Kit (Zymo). The RNA concentration from each sample was evaluated using a Tecan plate reader after resuspending RNAs in RNase free water. The RNA samples were immediately stored at −80 °C.

For RT-qPCR, cDNA was first synthesized from the RNA samples using the ProtoScript® First Strand cDNA Synthesis Kit (New England BioLabs). Input RNA was 200ng for each sample. The primers were designed using NCBI primer-BLAST and purchased from Integrated DNA Technologies. RT-qPCR was performed using PowerUp SYBR Green master mix (Applied Biosystems) and the Quantstudio 3 RT-PCR system. Expressions of specific genes were determined by normalizing the threshold cycle (Ct) values against the housekeeping gene. Primer sequences are listed in **Table 2.3.**

Table 2.3 Primers for RT-qPCR.

Gene	Accession Number	Forward Primer (5'->3')	Reverse Primer (5'->3')
ABCG2	NM_004827.3	AAGCCACAGAGATCATAGAGCC	TCTTCTTCTCACCCCCGGAA
CXCL12	NM_199168.4	AGATGCCCATGCCGATTCTT	AGGGCACAGTTTGGAGTGTT
GAPDH	NM_002046.7	ACAACTTTGGTATCGTGGAAGG	GCCATCACGCCACAGTTTC
MGMT	NM_002412.5	GCACCGTTTGCGACTTGG	GCTCACAACCAGACAGCTCC
SPP1	NM_000582.3	AGCTTTACAACAAATACCCAGATGC	GACTTACTTGGAAGGGTCTGTGG
VEGFA	NM_001025366.3	ACGAAAGCGCAAGAAATCCC	CTCCAGGGCATTAGACAGCA

2.5.8 RNA sequencing and data analysis

For RNA-seq analysis, RNA was extracted from sphere culture and 3D printed samples of TS576 cells using Direct-zol RNA MiniPrep Kit (Zymo, USA) and sequenced as described previously.[62] RNA was ribo-depleted and RNA-seq was performed using high-throughput Illumina sequencing system, Illumina NovaSeq 6000 (Illumina, San Diego, CA, USA) at the UC

San Diego IGM Genomics Center. The single-end reads that passed Illumina filters were filtered for reads aligning to transfer RNA, ribosomal RNA, adapter sequences and spike-in controls. We used Trim Galore (v0.6.5, https://github.com/FelixKrueger/TrimGalore) to trim and filter low-quality reads. After quality control, each FASTQ file was mapped to the human hg38 genome with gene annotation from GENCODE version 33 using STAR (v2.5.3a, https://github.com/alexdobin/STAR).[63] We then used htseq-count (v0.9.1, https://htseq.readthedocs.io/en/master/) to count exonic reads of each BAM file at the gene level and identify pairwise differentially expressed genes (DEG) between three experimental groups (sphere, 3D-stiff, 3D-soft) using R package DESeq2 (v1.24.0) with default settings.[64] Significant DEGs were determined by false discovery rate < 0.05. GO terms were identified using WebGestaltR (v0.4.4, http://www.webgestalt.org/).

Gene set enrichment analysis was performed with the GSEA desktop application (http://software.broadinstitute.org/gsea/downloads.jsp) and gene sets from molecular signatures database.[65] Processed data from primary patient GBM tissues and in vitro cultured GBM cells were derived from Mack et al.[31] and the list of upregulated expressed genes in primary GBM tissue were obtained using python package Scanpy (v1.6.0).[66] DEGs from the primary GBM tissue with adjusted *p*-value < 0.01 and log2 fold change >5 were selected to generate the input gene set for GSEA. Pathway enrichment bubble plots were generated using the Enrichment Map App of Cytoscape (v3.8.0).[67] Principal component analysis was performed using the top 5,000 DEGs.

2.5.9 Drug response assessment

Sphere cultured TS576 cells were seeded at a cell density of 1 x 10^5 cells per well and cultured for 5 days before treatment. Spheres were treated with different dosages of TMZ (Sigma-Aldrich) to generate the IC_{50} value of the TMZ on the sphere cultured TS576. For comparison of

drug sensitivity on TS576 cells in different culture conditions, spheres and 3D-printed samples were cultured for 5 days and treated with 500 μM TMZ. Cell viability was evaluated using CellTiter-Glo 3D after 6 days of TMZ treatment.

2.5.10 Molecular diffusion assessment

3D constructs with the same material composition and stiffness as the stiff ECM and soft ECM were printed and stabilized overnight. FITC-dextran with a molecular weight 4.4 kDa (Sigma) was prepared at a concentration of 0.5 mg/ml. A FITC-dextran solution was added to 3D-printed samples and incubated at 37 °C. Samples were rinsed and imaged at several time points (5, 15, 30, 60, 120 minutes). Intensity quantification was performed using ImageJ.

2.5.11 Statistical analysis

The results were presented as mean ± standard deviations. The statistical significance was evaluated using unpaired Student's t-test, ordinary one-way ANOVA, or two-way ANOVA with GraphPad Prism. *$p < 0.05$, ** $p < 0.01$, *** $p < 0.001$, **** $p<0.0001$.

2.5.12 Data deposition

All raw sequencing data reported in this paper has been deposited in the National Center for Biotechnology Information Gene Expression Omnibus (GEO) database, https://www.ncbi.nlm.nih.gov/geo/, at the accession numbers GSE158097. There are no restrictions on data availability, and all data will be made available upon request directed to the corresponding authors.

Acknowledgements

Chapter 2, in full, is a reprint of the published article, "Rapid 3D bioprinting of glioblastoma model mimicking native biophysical heterogeneity", Min Tang, Shashi Kant Tiwari, Kriti Agrawal, Matthew Tan, Jason Dang, Trevor Tam, Jing Tian, Xueyi Wan, Jacob Schimelman,

Shangting You, Qinghui Xia, Tariq M Rana, Shaochen Chen. *Small*, 2021. The dissertation author was the primary investigator and author of this paper.

We thank members of the Chen and Rana lab for helpful discussions and advices. M.Tang, S.K.T., K.A., M.Tan, J.D. contributed to the conceptualization; M.Tang, S.K.T, T.T., J.T., and X.W. performed the experiments; M.Tang, S.T., and K.A. analyzed data; J.S. performed material synthesis and characterization; S.Y. and Q.X. contributed to the printer and software optimization. M.Tang wrote the manuscript with help from S.K.T. and K.A.. T.R. and S.C. participated in the overall experimental design, data analyses, interpretation, manuscript writing, and obtained funding for the project. We thank Hanqing Liu for helpful suggestions on RNAseq analysis. This publication includes data generated at the UC San Diego IGM Genomics Center utilizing an Illumina NovaSeq 6000 that was purchased with funding from a National Institutes of Health SIG grant (#S10 OD026929). Confocal images were taken at the UCSD School of Medicine Microscopy Core, which is supported by a NINDS P30 grant (NS047101). This work was supported in part by grants from the National Institutes of Health (EB021857, CA253615, CA177322, DA039562, DA046171, and NS118250) and National Science Foundation (1937653). This material is based upon work supported by the National Science Foundation Graduate Research Fellowship Program under Grant No. DGE-1650112.

References

1. Koshy, M. *et al.* Improved survival time trends for glioblastoma using the SEER 17 population-based registries. *J Neurooncol* **107**, 207–212 (2012).

2. Bellail, A. C., Hunter, S. B., Brat, D. J., Tan, C. & Van Meir, E. G. Microregional extracellular matrix heterogeneity in brain modulates glioma cell invasion. *Int. J. Biochem. Cell Biol.* **36**, 1046–1069 (2004).

3. Chen, J.-W. E. *et al.* Influence of Hyaluronic Acid Transitions in Tumor Microenvironment on Glioblastoma Malignancy and Invasive Behavior. *Front. Mater.* **5**, (2018).

4. Gilg, A. G. *et al.* Targeting hyaluronan interactions in malignant gliomas and their drug-resistant multipotent progenitors. *Clin. Cancer Res.* **14**, 1804–1813 (2008).

5. Koh, I. *et al.* The mode and dynamics of glioblastoma cell invasion into a decellularized tissue-derived extracellular matrix-based three-dimensional tumor model. *Sci Rep* **8**, 4608 (2018).

6. Butcher, D. T., Alliston, T. & Weaver, V. M. A tense situation: forcing tumour progression. *Nature Reviews Cancer* **9**, 108–122 (2009).

7. Ahir, B. K., Engelhard, H. H. & Lakka, S. S. Tumor Development and Angiogenesis in Adult Brain Tumor: Glioblastoma. *Mol. Neurobiol.* **57**, 2461–2478 (2020).

8. Zanotelli, M. R. & Reinhart-King, C. A. Mechanical Forces in Tumor Angiogenesis. *Adv Exp Med Biol* **1092**, 91–112 (2018).

9. Schregel, K. *et al.* Magnetic Resonance Elastography reveals effects of anti-angiogenic glioblastoma treatment on tumor stiffness and captures progression in an orthotopic mouse model. *Cancer Imaging* **20**, 35 (2020).

10. Tiriac, H. *et al.* Organoid Profiling Identifies Common Responders to Chemotherapy in Pancreatic Cancer. *Cancer Discov* **8**, 1112–1129 (2018).

11. Lee, S. H. *et al.* Tumor Evolution and Drug Response in Patient-Derived Organoid Models of Bladder Cancer. *Cell* **173**, 515-528.e17 (2018).

12. Hubert, C. G. *et al.* A Three-Dimensional Organoid Culture System Derived from Human Glioblastomas Recapitulates the Hypoxic Gradients and Cancer Stem Cell Heterogeneity of Tumors Found In Vivo. *Cancer Res.* **76**, 2465–2477 (2016).

13. Murphy, S. V. & Atala, A. 3D bioprinting of tissues and organs. *Nature Biotechnology* **32**, 773–785 (2014).

14. Langer, E. M. *et al.* Modeling Tumor Phenotypes In Vitro with Three-Dimensional Bioprinting. *Cell Reports* **26**, 608-623.e6 (2019).

15. Tang, M. *et al.* Three-dimensional bioprinted glioblastoma microenvironments model cellular dependencies and immune interactions. *Cell Res* 1–21 (2020) doi:10.1038/s41422-020-0338-1.

16. Yi, H.-G. *et al.* A bioprinted human-glioblastoma-on-a-chip for the identification of patient-specific responses to chemoradiotherapy. *Nat Biomed Eng* **3**, 509–519 (2019).

17. Wang, C., Tong, X. & Yang, F. Bioengineered 3D Brain Tumor Model To Elucidate the Effects of Matrix Stiffness on Glioblastoma Cell Behavior Using PEG-Based Hydrogels. *Molecular Pharmaceutics* **11**, 2115–2125 (2014).

18. Ananthanarayanan, B., Kim, Y. & Kumar, S. Elucidating the mechanobiology of malignant brain tumors using a brain matrix-mimetic hyaluronic acid hydrogel platform. *Biomaterials* **32**, 7913–7923 (2011).

19. Xiao, W., Ehsanipour, A., Sohrabi, A. & Seidlits, S. K. Hyaluronic-Acid Based Hydrogels for 3-Dimensional Culture of Patient-Derived Glioblastoma Cells. *J Vis Exp* (2018) doi:10.3791/58176.

20. Wang, T.-W. & Spector, M. Development of hyaluronic acid-based scaffolds for brain tissue engineering. *Acta Biomaterialia* **5**, 2371–2384 (2009).

21. Engler, A. J., Sen, S., Sweeney, H. L. & Discher, D. E. Matrix Elasticity Directs Stem Cell Lineage Specification. *Cell* **126**, 677–689 (2006).

22. Chauvet, D. *et al.* In Vivo Measurement of Brain Tumor Elasticity Using Intraoperative Shear Wave Elastography. *Ultraschall in Med* **37**, 584–590 (2015).

23. Ulrich, T. A., de Juan Pardo, E. M. & Kumar, S. The mechanical rigidity of the extracellular matrix regulates the structure, motility, and proliferation of glioma cells. *Cancer Res.* **69**, 4167–4174 (2009).

24. Hribar, K. C. *et al.* Nonlinear 3D projection printing of concave hydrogel microstructures for long-term multicellular spheroid and embryoid body culture. *Lab Chip* **15**, 2412–2418 (2015).

25. Ma, X. *et al.* Deterministically patterned biomimetic human iPSC-derived hepatic model via rapid 3D bioprinting. *Proc. Natl. Acad. Sci. U.S.A.* **113**, 2206–2211 (2016).

26. Soman, P. *et al.* Three-dimensional scaffolding to investigate neuronal derivatives of human embryonic stem cells. *Biomed Microdevices* **14**, 829–838 (2012).

27. Ma, X. *et al.* Rapid 3D bioprinting of decellularized extracellular matrix with regionally varied mechanical properties and biomimetic microarchitecture. *Biomaterials* **185**, 310–321 (2018).

28. Yu, C. *et al.* Scanningless and continuous 3D bioprinting of human tissues with decellularized extracellular matrix. *Biomaterials* **194**, 1–13 (2019).

29. Polacheck, W. J., Zervantonakis, I. K. & Kamm, R. D. Tumor cell migration in complex microenvironments. *Cellular and molecular life sciences : CMLS* **70**, 1335–56 (2013).

30. Netti, P. A., Baxter, L. T., Boucher, Y., Skalak, R. & Jain, R. K. Time-dependent behavior of interstitial fluid pressure in solid tumors: implications for drug delivery. *Cancer research* **55**, 5451–8 (1995).

31. Mack, S. C. *et al.* Chromatin landscapes reveal developmentally encoded transcriptional states that define human glioblastoma. *J. Exp. Med.* **216**, 1071–1090 (2019).

32. Wang, Y., Ma, S. & Ruzzo, W. L. Spatial modeling of prostate cancer metabolic gene expression reveals extensive heterogeneity and selective vulnerabilities. *Scientific Reports* **10**, 3490 (2020).

33. Nakanishi, T. *et al.* A novel role for OATP2A1/ SLCO2A1 in a murine model of colon cancer. *Scientific Reports* **7**, 16567 (2017).

34. Zhu, Q., Liang, X., Dai, J. & Guan, X. Prostaglandin transporter, SLCO2A1, mediates the invasion and apoptosis of lung cancer cells via PI3K/AKT/mTOR pathway. *Int J Clin Exp Pathol* **8**, 9175–9181 (2015).

35. Hu, Y. *et al.* Netrin-4 Promotes Glioblastoma Cell Proliferation through Integrin β4 Signaling. *Neoplasia* **14**, 219–227 (2012).

36. Li, L. *et al.* NETRIN-4 protects glioblastoma cells FROM temozolomide induced senescence. *PLoS ONE* **8**, e80363 (2013).

37. do Carmo, A., Balça-Silva, J., Matias, D. & Lopes, M. C. PKC signaling in glioblastoma. *Cancer Biol Ther* **14**, 287–294 (2013).

38. Steponaitis, G. *et al.* High CHI3L1 expression is associated with glioma patient survival. *Diagn Pathol* **11**, (2016).

39. Liang, A., Zhou, B. & Sun, W. Integrated genomic characterization of cancer genes in glioma. *Cancer Cell International* **17**, 90 (2017).

40. Schmit, K. *et al.* Characterization of the role of TMEM45A in cancer cell sensitivity to cisplatin. *Cell Death & Disease* **10**, 1–18 (2019).

41. Sun, W. *et al.* Knockdown of TMEM45A inhibits the proliferation, migration and invasion of glioma cells. *Int J Clin Exp Pathol* **8**, 12657–12667 (2015).

42. Weiler, M. *et al.* mTOR target NDRG1 confers MGMT-dependent resistance to alkylating chemotherapy. *PNAS* **111**, 409–414 (2014).

43. Chen, X. *et al.* Identification of survival-associated key genes and long non-coding RNAs in glioblastoma multiforme by weighted gene co-expression network analysis. *Int. J. Mol. Med.* **43**, 1709–1722 (2019).

44. Lan, Y.-L., Wang, X., Lou, J.-C., Ma, X.-C. & Zhang, B. The potential roles of aquaporin 4 in malignant gliomas. *Oncotarget* **8**, 32345–32355 (2017).

45. Silginer, M. *et al.* Autocrine activation of the IFN signaling pathway may promote immune escape in glioblastoma. *Neuro Oncol* **19**, 1338–1349 (2017).

46. Brescia, P. *et al.* CD133 is essential for glioblastoma stem cell maintenance. *Stem Cells* **31**, 857–869 (2013).

47. Han, J., Alvarez-Breckenridge, C. A., Wang, Q.-E. & Yu, J. TGF-β signaling and its targeting for glioma treatment. *Am J Cancer Res* **5**, 945–955 (2015).

48. Mao, Z. *et al.* Pancreatic progenitor cell differentiation and proliferation factor predicts poor prognosis in heptaocellular carcinoma. *Medicine (Baltimore)* **98**, (2019).

49. Zhang, Y. *et al.* Dissecting dysfunctional crosstalk pathways regulated by miRNAs during glioma progression. *Oncotarget* **7**, 25769–25782 (2016).

50. Zhang, K. *et al.* Proteome Analysis of Hypoxic Glioblastoma Cells Reveals Sequential Metabolic Adaptation of One-Carbon Metabolic Pathways. *Mol Cell Proteomics* **16**, 1906–1921 (2017).

51. Alieva, M. *et al.* Intravital imaging of glioma border morphology reveals distinctive cellular dynamics and contribution to tumor cell invasion. *Scientific Reports* **9**, 2054 (2019).

52. Diao, W. *et al.* Behaviors of Glioblastoma Cells in in Vitro Microenvironments. *Sci Rep* **9**, (2019).

53. Neftel, C. *et al.* An Integrative Model of Cellular States, Plasticity, and Genetics for Glioblastoma. *Cell* **178**, 835-849.e21 (2019).

54. Pauty, J. *et al.* A Vascular Endothelial Growth Factor-Dependent Sprouting Angiogenesis Assay Based on an In Vitro Human Blood Vessel Model for the Study of Anti-Angiogenic Drugs. *EBioMedicine* **27**, 225–236 (2018).

55. Ngo, M. T. & Harley, B. A. The Influence of Hyaluronic Acid and Glioblastoma Cell Coculture on the Formation of Endothelial Cell Networks in Gelatin Hydrogels. *Adv. Healthcare Mater.* **6**, 1700687 (2017).

56. Lathia, J. D., Heddleston, J. M., Venere, M. & Rich, J. N. Deadly Teamwork: Neural Cancer Stem Cells and the Tumor Microenvironment. *Cell Stem Cell* **8**, 482–485 (2011).

57. Pitulescu, M. E. *et al.* Dll4 and Notch signalling couples sprouting angiogenesis and artery formation. *Nat Cell Biol* **19**, 915–927 (2017).

58. Leach, J. B., Bivens, K. A., Jr, C. W. P. & Schmidt, C. E. Photocrosslinked hyaluronic acid hydrogels: Natural, biodegradable tissue engineering scaffolds. *Biotechnology and Bioengineering* **82**, 578–589 (2003).

59. Shirahama, H., Lee, B. H., Tan, L. P. & Cho, N.-J. Precise Tuning of Facile One-Pot Gelatin Methacryloyl (GelMA) Synthesis. *Scientific Reports* **6**, 31036 (2016).

60. Benitez, J. A. *et al.* PTEN regulates glioblastoma oncogenesis through chromatin-associated complexes of DAXX and histone H3.3. *Nat Commun* **8**, 15223 (2017).

61. Wang, S. *et al.* Integrin αvβ5 Internalizes Zika Virus during Neural Stem Cells Infection and Provides a Promising Target for Antiviral Therapy. *Cell Rep* **30**, 969-983.e4 (2020).

62. Zhang, Q. *et al.* The long noncoding RNA ROCKI regulates inflammatory gene expression. *The EMBO Journal* **38**, e100041 (2019).

63. Frankish, A. *et al.* GENCODE reference annotation for the human and mouse genomes. *Nucleic Acids Res.* **47**, D766–D773 (2019).

64. Love, M. I., Huber, W. & Anders, S. Moderated estimation of fold change and dispersion for RNA-seq data with DESeq2. *Genome Biol.* **15**, 550 (2014).

65. Subramanian, A. *et al.* Gene set enrichment analysis: a knowledge-based approach for interpreting genome-wide expression profiles. *Proc. Natl. Acad. Sci. U.S.A.* **102**, 15545–15550 (2005).

66. Wolf, F. A., Angerer, P. & Theis, F. J. SCANPY: large-scale single-cell gene expression data analysis. *Genome Biology* **19**, 15 (2018).

67. Merico, D., Isserlin, R., Stueker, O., Emili, A. & Bader, G. D. Enrichment map: a network-based method for gene-set enrichment visualization and interpretation. *PLoS ONE* **5**, e13984 (2010).

CHAPTER 3 Modeling Glioblastoma Cellular Heterogeneity and Dependencies

3.1 Abstract

Brain tumors are dynamic complex ecosystems with multiple cell types. To model the brain tumor microenvironment in a reproducible and scalable system, we developed a rapid three-dimensional (3D) bioprinting method to construct clinically relevant biomimetic tissue models. In recurrent glioblastoma, macrophages/microglia prominently contribute to the tumor mass. To parse the function of macrophages in 3D, we compared the growth of glioblastoma stem cells (GSCs) alone or with astrocytes and neural precursor cells (NPCs) in a HA-rich hydrogel, with or without macrophage. Bioprinted constructs integrating macrophage recapitulate patient-derived transcriptional profiles predictive of patient survival, maintenance of stemness, invasion, and drug resistance. Whole genome CRISPR screening with bioprinted complex systems identified unique molecular dependencies in GSCs, relative to sphere culture. Multicellular bioprinted models serve as a scalable and physiologic platform to interrogate drug sensitivity, cellular crosstalk, invasion, context-dependent functional dependencies, as well as immunologic interactions in a species-matched neural environment.

3.2 Introduction

Brain tumors are complex tissues with multicomponent interactions between multiple cell types.[1] Precision medicine efforts based solely on genomic alterations and molecular circuitries driving neoplastic cells have translated into relatively limited benefit in clinical practice for brain cancers, including glioblastoma, the most prevalent and lethal primary intrinsic brain tumor. Crosstalk between neoplastic cells and the surrounding stroma contributes to tumor initiation, progression, and metastasis. However, most cancer research studies investigate cancer cells in isolation, cultured in non-physiologic adherent conditions containing species-mismatched serum.

Massive efforts have interrogated functional dependencies of cancer cell lines.[2-5] While these studies provide valuable insights into cancer cell dependencies, they lack the capacity to investigate interactions of cancer cells with stromal cells or the microenvironment in an appropriate physiological context. PDXs and genetically engineered mouse models are informative and can better recapitulate the genomic and transcriptomic profiles of patient brain tumors than two-dimensional (2D) culture. However, challenges with engraftment, the low throughput nature of animal experiments, and the lack of normal human cellular interactions, limit their broad applications in clinical settings. In tumors with significant immune cell involvement, such as glioblastoma, PDXs are limited as immunocompromised animals prevent investigation of immune cells in cancer biology.[6]

Methods to construct self-organizing 3D co-culture systems, termed organoids, have been developed to interrogate physiological and pathophysiological processes.[7,8] In cancer research, organoid systems serve as models of colorectal cancer[9,10], breast cancer[11,12], hepatocellular and cholangiocarcinomas,[13] pancreatic cancers,[14] and glioblastomas,[15] among others.[16,17] In glioblastoma, we first described organoid systems that recapitulate tumor architecture, microenvironmental gradients, and tumor cellular heterogeneity.[15] Additional glioblastoma models utilize human-embryonic stem cell (hESC)-derived cerebral organoids to investigate interactions between GSCs and normal brain components including infiltration, microenvironmental stimuli, and response to therapies.[18] However, organoid modeling is labor intensive, relatively low throughput, and highly variable in terms of cellular composition and structure due to the process of self-assembly.

Further development of tissue engineering approaches inform new 3D culture systems with improved scalability and capacity to tune specific biological parameters, including cellular

composition and extracellular matrix stiffness.[19] The development of physiologically relevant brain tumor microenvironments[20] requires careful consideration of the biophysical and biochemical properties of the matrix and cellular composition of specific tumor types, which can be achieved with recent advances in 3D bioprinting and biomaterials designed specifically for the bioprinting process.[21-24] Biocompatible scaffolds for tumor microenvironments include the naturally occurring extracellular matrix products chitosan-alginate (CA)[25] and hyaluronic acid (HA)-based hydrogels[26,27], but also synthetic polymers, including poly lactide-co-glycolide (PLGA)[28], and polyethylene-glycol (PEG)[26], or polyacrylamide hydrogels[29]. 3D printing with biocompatible materials is emerging to advance the fields of regenerative medicine and tissue modeling[21], with notable relevance and applicability to cancer research[22]. 3D bioprinting models microenvironmental interactions and drug sensitivities,[18] reciprocal interactions with macrophages,[23] and patient-specific screening tools in microfluidics-based systems.[24] Among many 3D printing technologies, digital light processing (DLP)-based 3D bioprinting provides superior scalability and printing speed in addition to versatility and reproducibility.[30] Several biomimetic tissue models have been developed using this technology, creating tissue specific architecture and cellular composition that could be used for functional analyses, metastasis studies, and drug screening.[31,32]

Here, we employ a rapid 3D bioprinting system and photocrosslinkable native ECM derivatives to create a biomimetic 3D cancer microenvironment for the highly lethal brain tumor, glioblastoma. The model is comprised of patient derived GSCs, macrophages, astrocytes, and NPCs in a HA-rich hydrogel. One major microenvironmental feature of glioblastoma is the prominent infiltration of tumor masses by macrophage and microglia. In progressive or recurrent glioblastoma, macrophage and microglia account for a substantial fraction of the tumor bulk. Using

genetic depletion, co-implantation, and pharmacologic depletion, macrophage/microglia have been shown to be functionally important for glioblastoma growth, but each of these approaches may have broader effects beyond direct tumor cell-macrophage interactions. Using this scalable and reproducible platform, we can interrogate functional dependencies and multicellular interactions in a physiologically relevant manner.

3.3 Results

3.3.1 DLP-based rapid 3D bioprinting generates glioblastoma tissue models

Brain tumors are composed of numerous distinct populations of malignant and supporting stromal cells, and these complex cellular interactions are essential for tumor survival, growth, and progression. Glioblastomas display high levels of intratumoral heterogeneity, with contributions from astrocytes, neurons, NPCs, macrophage/microglia, and vascular components. To move beyond serum-free sphere culture-based models, we utilized a DLP-based rapid 3D bioprinting system to generate 3D tri-culture or tetra-culture glioblastoma tissue models, with a background "normal brain" made up of NPCs and astrocytes and a tumor mass generated by GSCs, with or without macrophage, using brain-specific ECM materials (Figure 3.1a). Leveraging this system with exquisite control of cellular constituents in specific locations, we selected macrophage for additional study, as we hypothesized that DLP-based 3D bioprinting could enable precise spatial arrangement of cells and matrix, and selection of any cell type. The key components of the bioprinting system were a digital micromirror device (DMD) chip and a motorized stage where prepolymer cell-material mixtures were sequentially loaded. The DMD chip with approximately $2x10^6$ micromirrors controlled the light projection of the brain-shaped patterns onto the printing materials (Figure 3.1b). The elliptical pattern corresponded to the core region and the coronal slice pattern corresponded to the peripheral region. Each pattern was printed with 20 seconds of light exposure. In the 3D tri-culture model, a central tumor core composed of GSCs was surrounded by

a less dense population of astrocytes and NPCs. In the 3D tetra-culture model, we mixed M2 macrophages with GSCs within the central core to mimic the immune cell infiltrated tumor mass (Figure 3.1c).

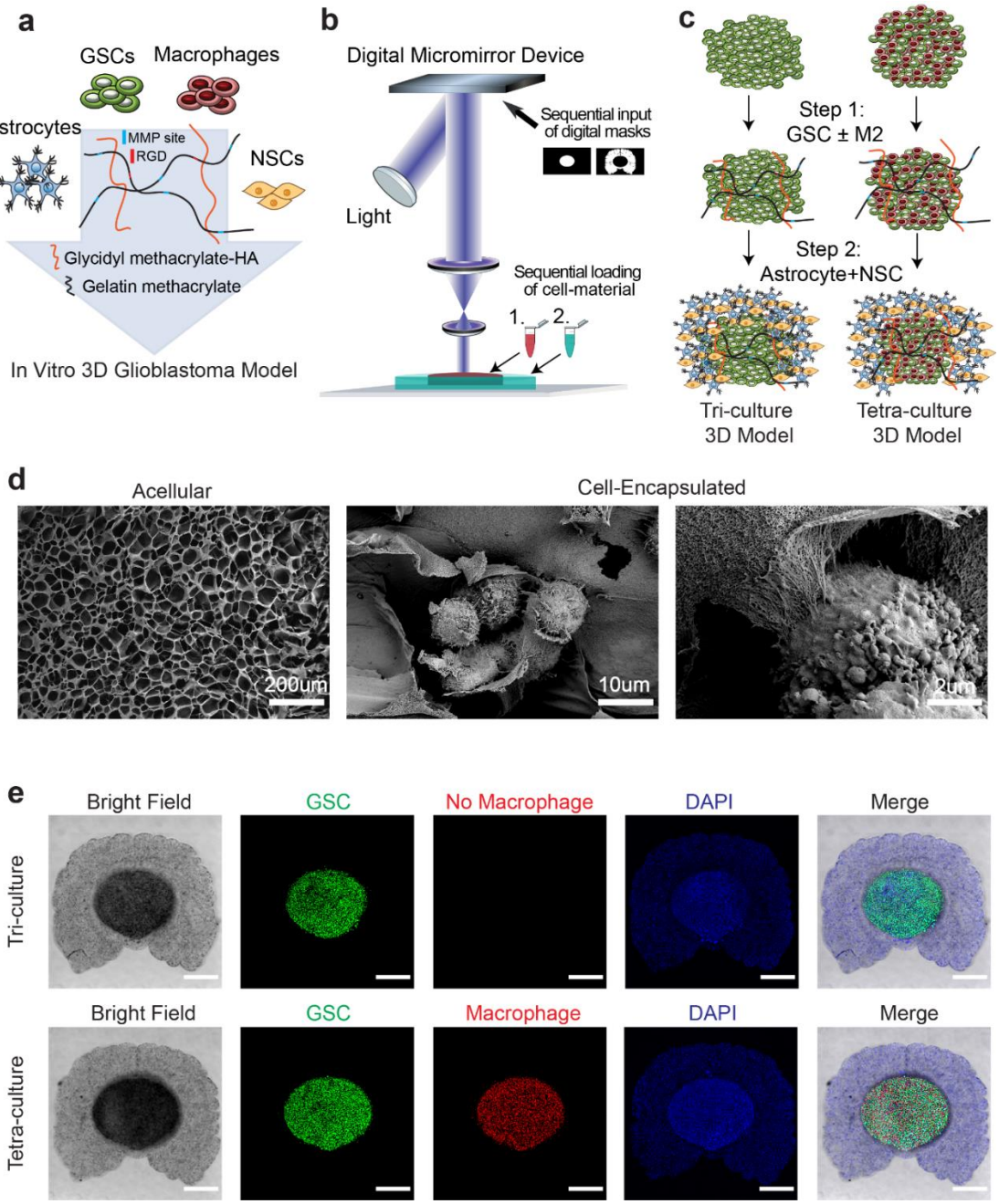

Figure 3.1 3D bioprinting enables generation of glioblastoma tri-culture and tetra-culture tissue environment model.

The ECM composition of the glioblastoma microenvironment was modeled with GelMA and GMHA hydrogels. Cells were encapsulated into a material mixture of 4% GelMA (at 95% degree of methacrylation) and 0.25% GMHA (at 38% degree of methacrylation), which generated a hydrogel matrix that resembled glioblastoma tissue. GelMA has good biocompatibility and serves as a stiffness modulator that provided desirable mechanical properties and little intervention in biochemical cues. HA is the most abundant ECM component in healthy brain tissue and promotes glioblastoma progression, including regulating glioblastoma invasion through the receptor for hyaluronan-mediated motility (RHAMM) and CD44, as well as other mechanical and topographical cues.[33] We used a physiologically relevant concentration of HA (0.25%) determined from clinical analysis of a diverse population of biopsy specimens from patients with different brain tumors.[34] While a range of molecular weight HAs are present in the brain, low molecular HA promotes GSC stemness and resistance.[33] Thus, in this study, low molecular weight HA (200 kDa) was used to synthesize GMHA to model the pro-invasive brain tumor microenvironment. The mechanical properties of the model were characterized by the compressive modulus and pore sizes. The stiffness of the acellular hydrogel remained stable over a week of incubation at 37°C (data not shown). The stiffness of cell-encapsulated tumor core was 2.8 ± 0.6 kPa, while the less populated peripheral region containing NPCs and astrocytes was 0.9 ± 0.2 kPa.

The peripheral region stiffness was designed to match that of healthy brain tissue reported to be around 1 kPa. Glioblastoma displays enhanced migration and proliferation in stiffer materials.[33] The stiffness of the tumor core was modulated with the light exposure time on the 3D bioprinter to have higher modulus than the healthy region. The hydrogel had a porosity of 53% and an average pore size of 85 μm. With these microscale features, small molecules, such as drug molecules, freely diffuse through the matrix. Cells closely interacted with other cells and the

matrix (Figure 3.1d). At a macro scale, the model had a thickness of 1 mm, and 4.4 mm by 3.6 mm in the X-Y dimensions, which allowed gradients of oxygen and nutrition diffusion to be formed within the tissue. Cells were precisely printed into two prearranged regions to provide more physiologically relevant features: a non-neoplastic peripheral region composed of NPCs and astrocytes surrounding a tumor core composed of either GSCs alone or GSCs with macrophage (Figure 3.1e). Following optimization for cell density, the tumor core in the 3D tri-culture consisted of 25 x 10^6 GSCs/mL, while the tetra-culture tumor core contained 25 x 10^6 GSCs/mL and 12.5 x 10^6 macrophages/mL.

3.3.2 3D bioprinted models recapitulate glioblastoma transcriptional profiles

Traditionally grown cell lines have been extensively characterized in glioblastoma, revealing that these conditions fail to replicate patient tumors in cellular phenotypes (e.g. invasion) or transcriptional profiles.[35] While patient-derived glioblastoma cells grown under serum-free conditions enrich for stem-like tumor cells (GSCs) that form spheres and more closely replicate transcriptional profiles and invasive potential than standard culture conditions, we previously demonstrated that spheres display differential transcriptional profiles and cellular dependencies in an RNA interference screen compared to in vivo xenografts.[36] Based on this background, we interrogated the transcriptional profiles from a large cohort of patient-derived GSCs grown in serum-free, sphere cell culture that we recently reported.[37] GSCs grown as spheres were transcriptionally distinct from primary glioblastoma surgical resection tissue specimens, when compared through either principal component analysis (PCA) or Uniform Manifold Approximation and Projection (UMAP) (Figures 3.2a and 3.2b).

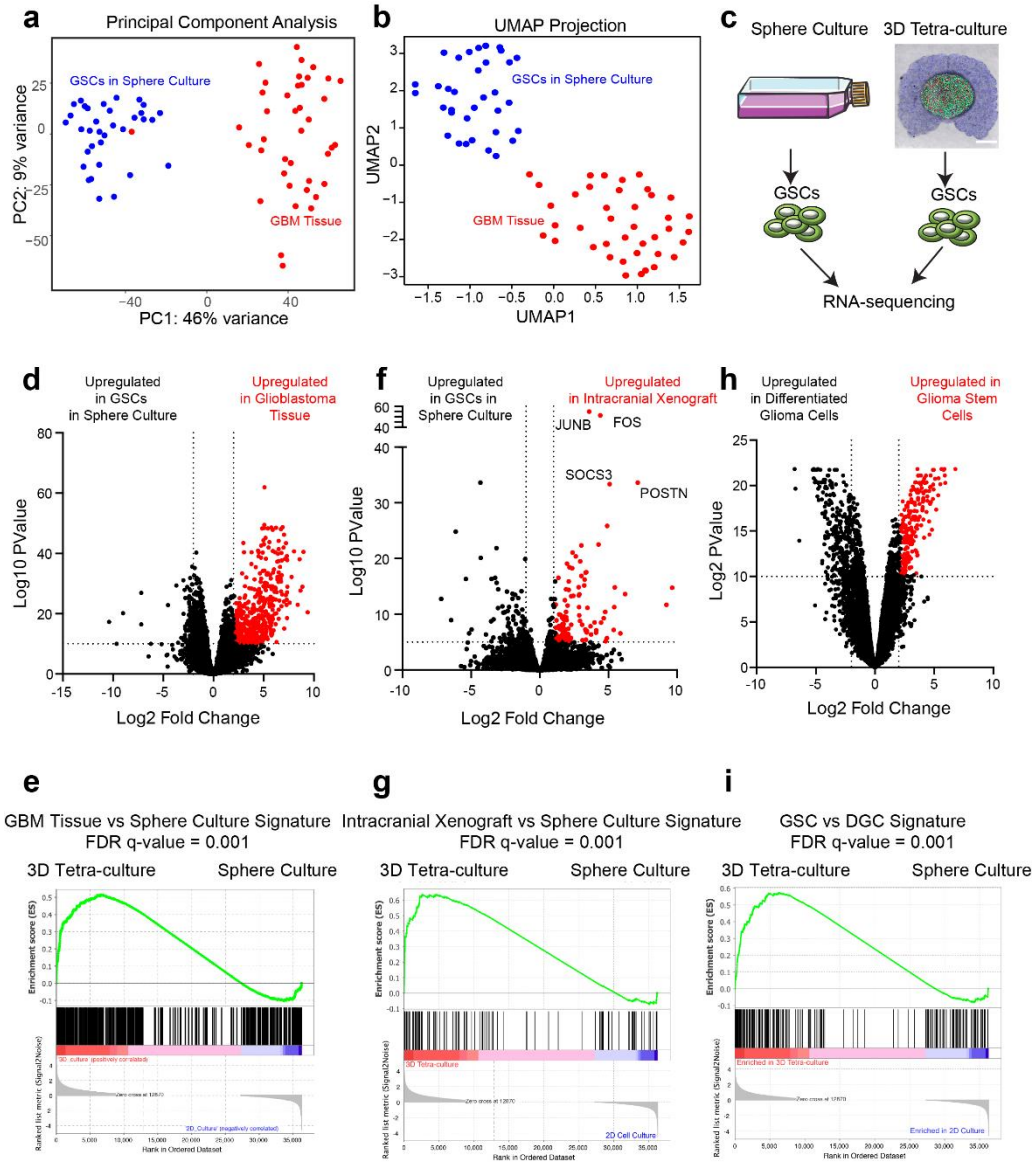

Figure 3.2 3D tetra-culture models better recapitulate transcriptional signatures found in glioblastoma tissues than standard sphere culture.

To determine if the 3D bioprinted culture systems more closely resemble primary glioblastoma tumors, we performed global transcriptional profiling through RNA extraction followed by next-generation sequencing (RNA-seq) on GSCs isolated from the bioprinted models (Figure 3.2c). Upregulation of a core set of glioblastoma tissue-specific genes defined a "Glioblastoma Tissue" gene signature (Figure 3.2d). When compared to GSCs grown in sphere

culture, the tetra-culture bioprinted model displayed upregulation of the glioblastoma tissue-specific gene set (Figure 3.2e), suggesting that the bioprinted model recapitulates transcriptional states present in patient-derived glioblastoma tissues. GSCs in 3D tetra-culture displayed upregulation of genes specifically expressed in orthotopic intracranial xenografts (Figures 3.2f and 3.2g) and, to a lesser extent, genes specifically expressed in subcutaneous flank xenografts compared to sphere culture. Additionally, GSC signatures were upregulated in the tetra-culture system compared to sphere culture (Figures 3.2h and 3.2i), suggesting that the physiologic tissue environment promotes stem-like transcriptional states.

We further interrogated the gene expression profiles that distinguish GSCs grown in sphere culture from the 3D tetra-culture bioprinted models (Figure 3.3a). While cells grown in sphere culture displayed enrichment for gene sets involved in ion transport, protein localization, and vesicle membrane function, cells in the tetra-culture 3D model displayed transcriptional upregulation of cell adhesion, extracellular matrix, cell and structure morphogenesis, angiogenesis, and hypoxia signatures (Figure 3.3b). Furthermore, the tetra-culture model displayed an increase in the mesenchymal glioblastoma signature (Figure 3.3c). Hypoxia response genes, CA9, NDRG1, ANGPTL4, and EGLN family members, were upregulated in the tetra-culture system, while various ion transporters, including SLC25A48 and SLC6A9, were downregulated (Figures 3.3d and 3.3e). By qPCR, GSCs isolated from either 3D system 10 days after printing displayed elevated levels of the stemness marker OLIG2 and decreased levels of the differentiation markers MAP2 and TUJ1 compared to their sphere counterparts grown in parallel (Figure 3.3f). Additionally, GSC levels of MAP2 and TUJ1 were decreased to a greater degree in tetra-culture (i.e. with macrophage) compared to tri-culture. We further evaluated the protein expression of stemness, hypoxia, and proliferative markers in the tetra-culture system compared to sphere culture. The

hypoxia marker CA9 was upregulated in the tetra-culture model compared to sphere culture (Figure 3.3g). The heightened hypoxia level more closely resembled pathologic in vivo conditions, in which the tumor core had a higher hypoxia expression compared to the peripheral region of neurons and astrocytes. In the 3D culture system, cells also showed increased levels of the proliferative marker Ki67 and increased protein expression of the stemness markers OLIG2 and SOX2 (Figures 3.3h-j).

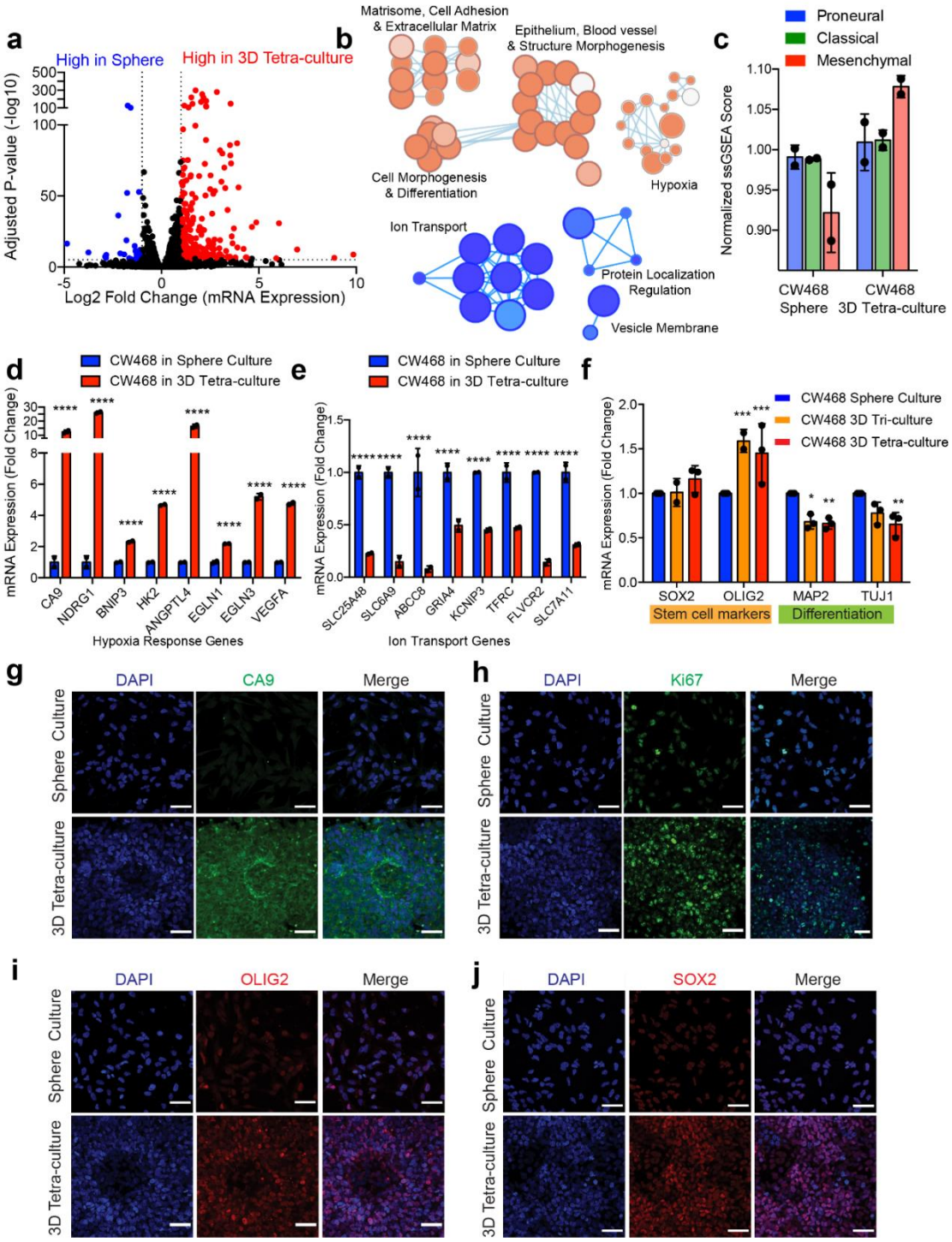

Figure 3.3 GSCs grown in 3D tetra-culture models upregulate transcriptional signatures of cellular interaction, hypoxia, and cancer stem cells.

3.3.3 Macrophages promote hypoxic and invasive signatures in bioprinted models

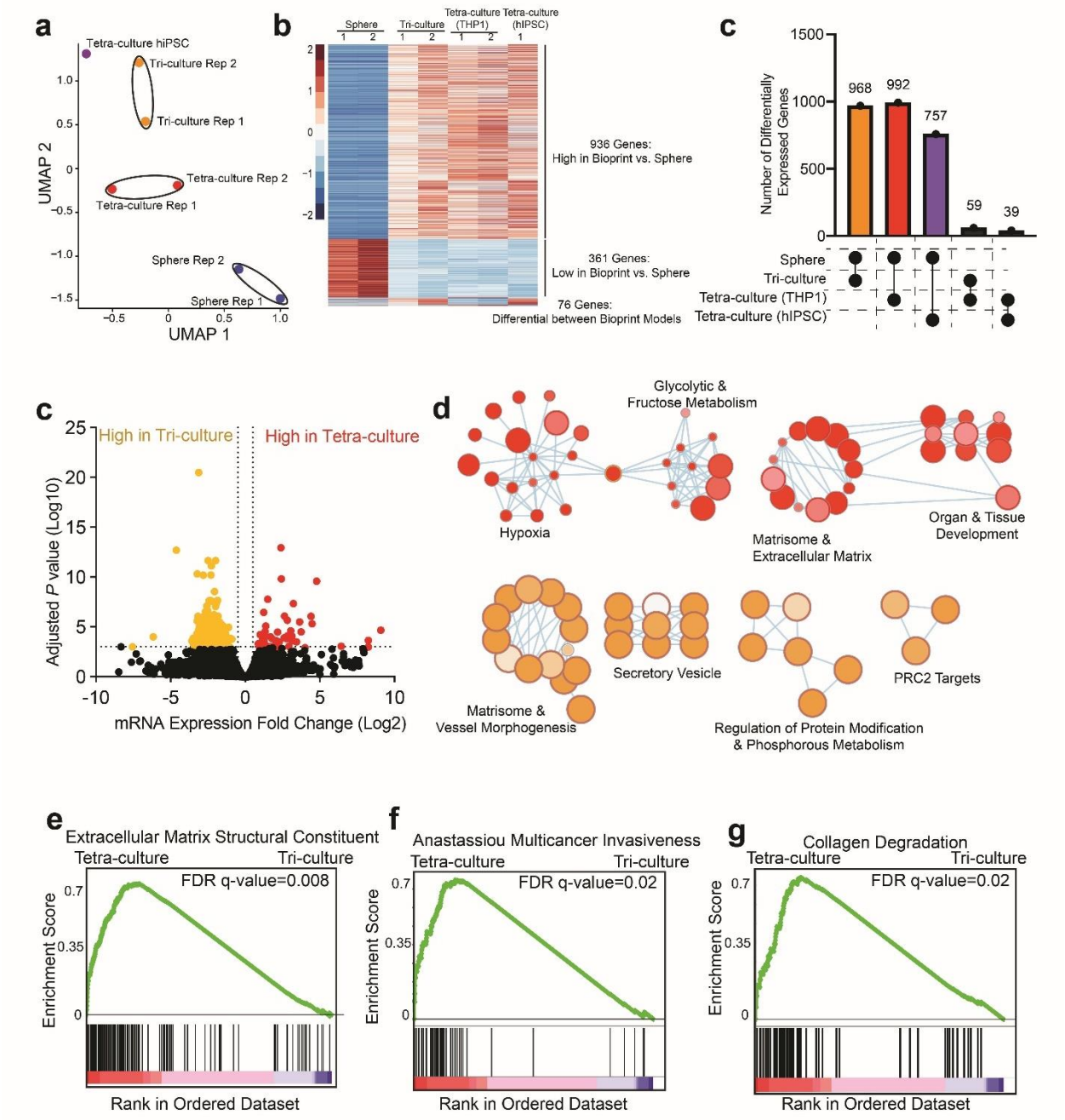

Figure 3.4 Addition of macrophages activates extracellular matrix and invasiveness signatures.

To understand the relative contributions of each cell type incorporated into bioprinted models, we performed RNA-sequencing on GSCs derived from tri-cultures and tetra-cultures. Given that THP1-derived macrophages display distinct expression profiles as primary

macrophages, we built tetra-cultures containing THP1-derived macrophage, human induced pluripotent stem cell (hiPSC)-derived macrophage generated from an established protocol,[38] and primary human volunteer-derived macrophage. Both hiPSC-derived macrophage and primary macrophage integrated into the tetra-culture models. UMAP clustering revealed that the transcriptional outputs of sphere cultured GSCs are distinct from that of GSCs in bioprinted models (Figures 3.4a and 3.4b). Concordantly, we detected differentially expressed genes between sphere cultured cells and any of the bioprinted models (757-968 differentially expressed genes), while there were fewer genes that distinguished the bioprinted models (39-59 differentially expressed genes) (Figure 3.4c). Bioprinted models were characterized by activation of invasion, extracellular matrix, cell surface interaction, and hypoxia signatures, while GSCs in sphere culture expressed cell cycle, DNA replication, RNA processing, and mitochondrial translation signatures. Multiple genes in the hypoxia, biological adhesion and extracellular matrix, and the mesenchymal glioblastoma subtype signature were consistently upregulated across bioprinted models. When grown in bioprinted models, GSCs transitioned from an initial proneural/classical transcriptional subtype to a mesenchymal state.

We next investigated differentially expressed pathways between bioprinted models. Triculture-derived GSCs upregulated extracellular matrix and biological adhesion pathways compared to GSCs in sphere culture. Addition of macrophage further increased activation of hypoxia and glycolytic metabolism signatures, with enrichment for invasiveness signatures (Figures 3.4d-h). Tetra-cultures constructed with hiPSC-derived macrophage expressed higher levels of extracellular matrix and wound healing and platelet activation signatures and decreased levels of neuron and glial development and differentiation pathways compared to tetra-cultures, including THP1-derived macrophages. Incorporation of primary human macrophages did not

affect levels of Ki67 or SOX2 compared to use of THP1-derived cells. Consistent with our previous findings, use of hiPSC-derived macrophages reduced GSC expression of MAP2 and TUJ1 differentiation markers and increased expression of CA9 and NDRG1 hypoxia markers.

3.3.4 3D bioprinted tissues model complex cellular interactions and migration

Interactions between malignant cells and stromal components shape tumor tissue with each cell type impacting the other tissue components. To understand these changes, we investigated how macrophage responded to the 3D brain tumor microenvironment by isolating THP1-derived macrophages from 3D bioprinted structures and performing RNA-seq (Figures 3.5a and 3.5b). For the 3D printed tissue, macrophage were mixed with GSCs at a 1:2 ratio to form the tumor core, while the periphery was formed by astrocytes and NPCs using the same composition described previously. The transcriptional output of macrophage grown in traditional culture displayed enrichment for PRC2 complex targets, amino acid biosynthesis, protein metabolism signatures and ribosomal pathways, while macrophage exposed to GSCs in the bioprinted structure showed elevation of pathways involved in leukocyte activation and innate immune response, cytokine signaling and inflammatory responses, and TLR-stimulated signatures (Figure 3.5c). Defense response genes, including CH14, PLA2G7, and ALOX5, were upregulated in macrophage derived from the tetra-culture system, while genes involved in amino acid restriction, including IL18, CD37, and VLDLR, were downregulated (Figures 3.5d and 3.5e). M2 macrophage-related markers were upregulated in the 3D samples, with CD163 increased by 37-fold and IL-10 increased by 17-fold compared to traditional suspension culture, as measured by qPCR. M1-related markers, including TNF-α and NOS2, did not increase, demonstrating that the 3D printed microenvironment preferentially polarized macrophage towards the M2 phenotype (Figure 3.5f). Gene expression signatures defining peripherally-derived tumor associated macrophage in glioma[39,40] were selectively enriched in macrophage derived from tetra-culture models compared to those grown in

2D culture. Collectively, macrophage grown in our 3D bioprinted tetra-culture model express gene expression signatures consistent with patient-derived tumor-associated macrophage.

We interrogated the functional consequences of the addition of immune components to the 3D bioprinted model. In four patient-derived GSCs spanning three major glioblastoma transcriptional subtypes (proneural, classical, and mesenchymal) the addition of monocyte-derived M2 macrophage increased GSC invasion into the surrounding brain-like parenchyma (Figures 3.5g-j). Consistent with our gene expression analyses, M2 macrophage increased the area of invasion by 20% for CW468, 60% for GSC23, 41% for GSC3264, and 30% for GSC2907. Collectively, these results support the tetra-culture model as an effective tool to study cancer cell invasion and the mechanisms by which cellular interactions impinge upon these processes.

As numerous stromal compartments, including neural progenitor cells, astrocytes, and neurons, interact with glioblastoma cells within patient tumors, we interrogated the effects of the bioprinting model on neuronal and oligodendrocyte differentiation of the non-neoplastic NPCs. In 2D culture, most NPCs expressed the proliferative NPC marker SOX2. The high expression and frequency of SOX2 was retained in tri-cultures and tetra-cultures containing macrophage derived from THP1 cells or primary human macrophage. In 2D culture, NPCs expressed the neuronal marker TUBB3, but retained a progenitor-like cellular morphology. In bioprinting models, NPCs adopted a neuronal morphology with the appearance of elongated cellular projection. Expression of MAP2 was reduced in bioprinted models compared to 2D culture. OLIG2 staining revealed oligodendrocyte-like cells in tri-cultures. Taken together, NPCs partially differentiate in our bioprinted system, but are unlikely to form mature functional neurons or oligodendrocytes.

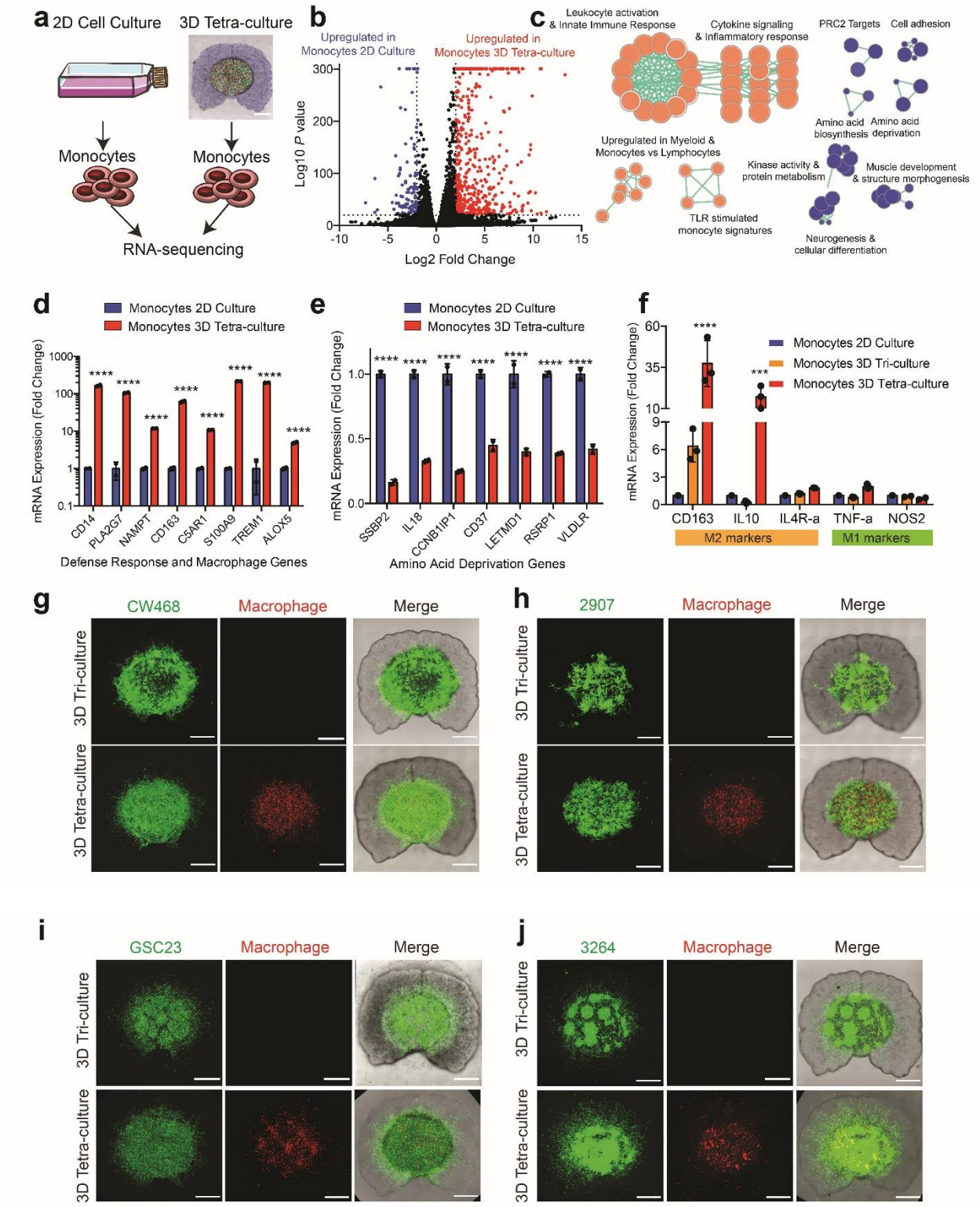

Figure 3.5 Monocytes grown in 3D tetra-culture models upregulate immune activation signatures, increase M2 polarization, and promote GSC invasion.

3.3.5 The 3D bioprinted model serves as a platform for drug response modeling

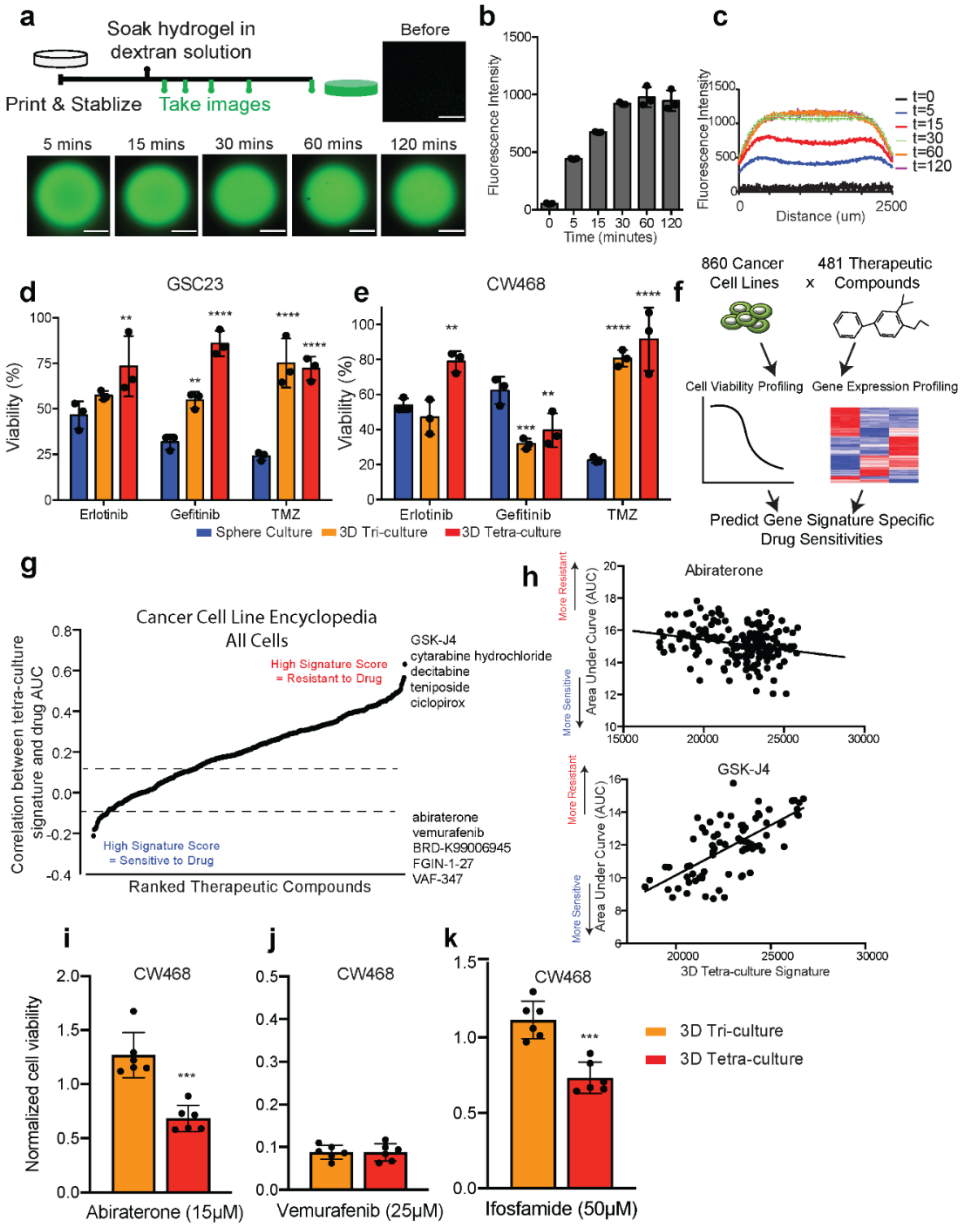

Figure 3.6 3D bioprinting enables a drug discovery platform and microenvironmental interactions contribute to drug resistance.

We next investigated the ability of our 3D bioprinted system to model drug responses and the capacity for cellular interactions within the 3D bioprinted system to affect drug sensitivity of GSCs. Fluorescent dextran molecules (4 kDa) modeled drug penetration into 3D bioprinted models.[31,41] Dextran molecules rapidly entered bioprinted constructs when the hydrogel was

soaked in a dextran solution, with rapid increases in average fluorescence intensity measured from the hydrogel. The fluorescence intensity plateaued after 30 minutes of incubation and displayed a uniform spatial intensity across the hydrogel, demonstrating that drug compounds can effectively permeate the 3D bioprinted model (Figures 3.6a-c).

EGFR is commonly amplified, overexpressed, or mutated in glioblastoma, so we evaluated the treatment efficacy of two EGFR inhibitors, erlotinib and gefitinib, and the glioblastoma standard-of-care alkylating agent temozolomide in our system. 3D tri-cultures and tetra-cultures were cultured for 5 days before drug treatment. Despite activated EGFR in glioblastomas, EGFR inhibitors have shown little benefit for glioblastoma patients. GSC23 in either 3D model displayed enhanced resistance to EGFR inhibitors and temozolomide compared to sphere culture. Inclusion of M2 macrophage further increased resistance of GSC23 to EGFR inhibitors (Figure 3.6d). CW468 cultured in 3D models displayed enhanced resistance to erlotinib and temozolomide treatment, in contrast to gefitinib (Figure 3.6e), despite maintaining high EGFR mRNA and protein expression in tetra-cultures. Both erlotinib and gefitinib displayed on target effects and reduced EGFR activity as measured by phosphorylation of the EGFR-Y1173 residue in both sphere culture and in tetra-cultures.

Glioblastomas are highly lethal cancers for which current therapy is palliative.[42,43] Therefore, we explored the potential utility of 3D bioprinted systems to inform drug responses in glioblastoma. Overlaying gene expression data from the 3D tetra-culture model with drug sensitivity and gene expression data from the Cancer Cell Line Encyclopedia (CCLE) and the Cancer Therapeutic Response Platform (CTRP) enabled prediction of drug sensitivity and resistance in our 3D tetra-culture system based on transcriptional signatures (Figure 3.6f).[44-46] Consistent with our studies of erlotinib, gefitinib, and temozolomide, high expression of genes

upregulated in GSCs in the 3D tetra-culture model was predicted to be associated with drug resistance for the majority of compounds across all cancer cell lines tested (Figure 3.6g) or when restricted to brain cancer cell lines. Drugs predicted to ineffective included GSK-J4 (JMJD3/KDM6B inhibitor), cytarabine (nucleotide antimetabolite), and decitabine (DNA methyltransferase inhibitor), while drugs predicted to be effective included abiraterone (CYP17A1 inhibitor), vemurafenib, ifosfamide, and PLX-4720 (RAF inhibitors), and ML334 (NRF2 activator) (Figures 3.6g-j). These results were similar, but not entirely overlapping, when a glioblastoma orthotopic xenograft expression signature was used. Investigation of the Library of Integrated Network-Based Cellular Signatures (LINCS) dataset showed that compounds predicted to recapitulate the 3D tetra-culture signature included hypoxia inducible factor activators, caspase activators, and HDAC inhibitors, while RAF inhibitors and immunosuppressive agents may impair expression of this gene signature. These findings suggest that interactions with the local microenvironment affect GSC sensitivity to therapeutic compounds and that the 3D bioprinted tissue model can interrogate these context-dependent effects. Further, as the tetra-culture model expresses genes associated with poor sensitivity to a variety of therapeutic compounds, this system may be a more realistic model for drug discovery in glioblastoma. To validate these predictions, we treated GSCs with three of the predicted compounds, abiraterone, vemurafenib, and ifosfamide in triculture and tetraculture bioprinted models. When treated at the sphere culture IC50 value, GSCs in tetra-culture displayed enhanced sensitivity to abiraterone and ifosfamide compared to GSCs in tri-culture, while sensitivity to vemurafenib was unchanged (Figure 3.6i-k). This suggests that abiraterone and ifosfamide may be effective in targeting tetra-culture derived GSCs. In a subcutaneous glioblastoma xenograft model, ifosfamide therapy displayed a trend towards reduced tumor growth compared to vehicle.

3.3.6 CRISPR Screening Discovered Novel Context-Dependent Essential Pathways

Given widespread therapeutic resistance in glioblastoma, we leveraged the 3D bioprinted system as a discovery platform for glioblastoma dependencies. Parallel whole genome CRISPR-Cas9 loss-of-function screening was performed in GSCs in sphere culture as well as in the 3D tetra-culture system (Figure 3.7a). Functional dependencies segregated GSCs based on their method of growth (Figure 3.7b). Guide RNAs were enriched (indicating that the targeted gene enhances viability when deleted) or depleted (indicating that the targeted gene reduces cell viability when deleted) in each platform (Figures 3.7c and 3.7d). Genes essential in each context, as well as pan-essential genes common to both platforms, included core pathways involved in translation, ribosome functions, and RNA processing, cell cycle regulation, protein localization, and chromosomes and DNA repair (Figure 3.7e). Gene hits were stratified to identify context-specific dependencies (Figure 3.7f). Genes selectively essential in sphere culture were enriched for cell cycle, endoplasmic reticulum, golgi and glycosylation, lipid metabolism, and response to oxygen pathways. GSCs grown in the 3D tetra-culture system were more dependent on transcription factor activity, cell development and differentiation, NF-κB signaling, and immune regulation pathways (Figures 3.7g-k). Thus, the 3D bioprinted model system allowed for interrogation of functional dependencies of brain tumor cells in physiological settings and in combination with stromal fractions and revealed a more complex functional dependency network than that observed in sphere culture.

To further validate 3D bioprinted-specific dependencies, we stratified our whole genome CRISPR screening results (Figures 3.8a and 3.8b). Individual gene knockout in luciferase labeled GSCs of PAG1, ZNF830, ATP5H, and RNF19A with two independent sgRNAs reduced GSC viability in both sphere culture and tetracultures (Figures 3.8c-m).

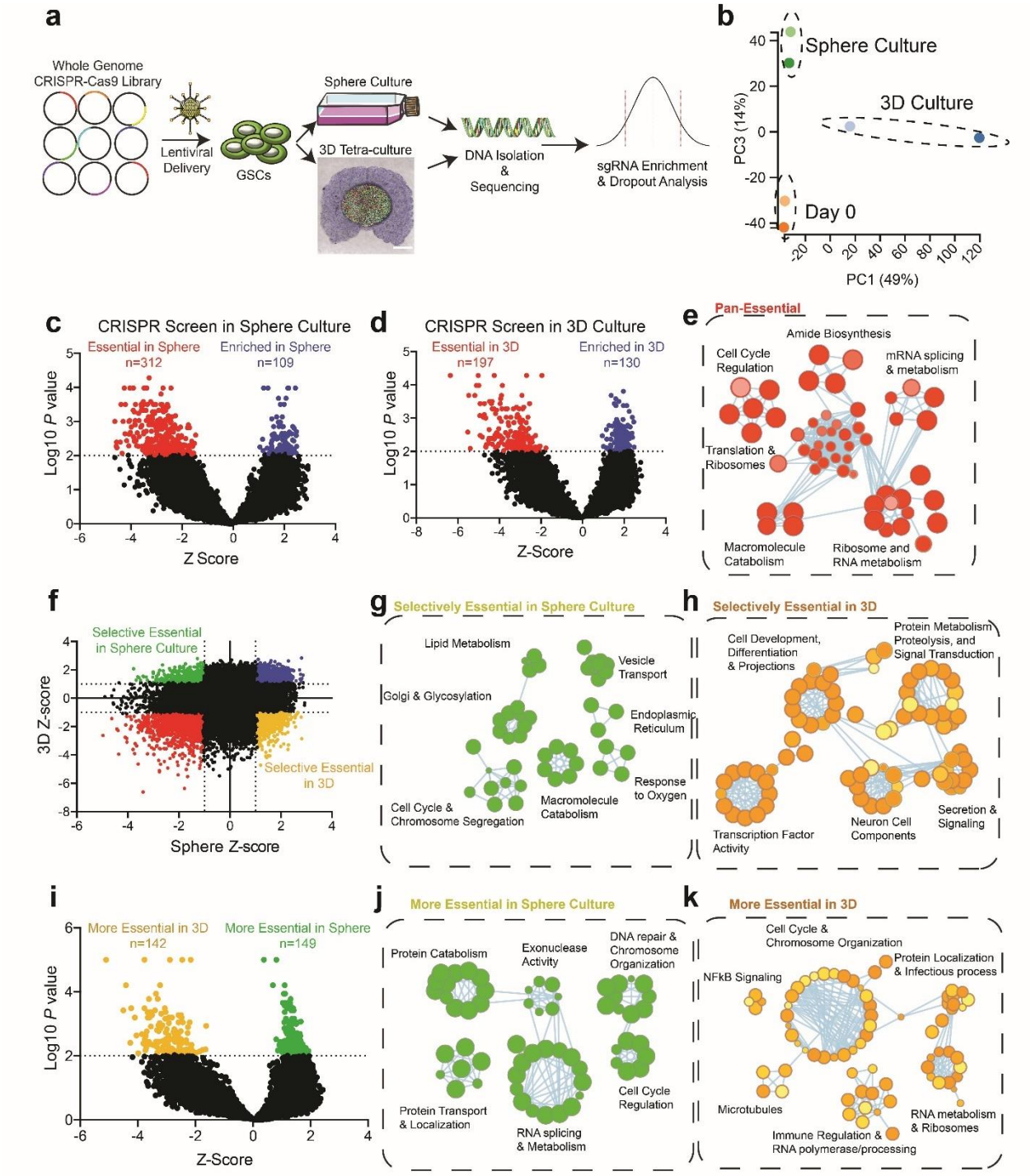

Figure 3.7 Whole genome CRISPR-Cas9 screen reveals context-dependent functional dependencies.

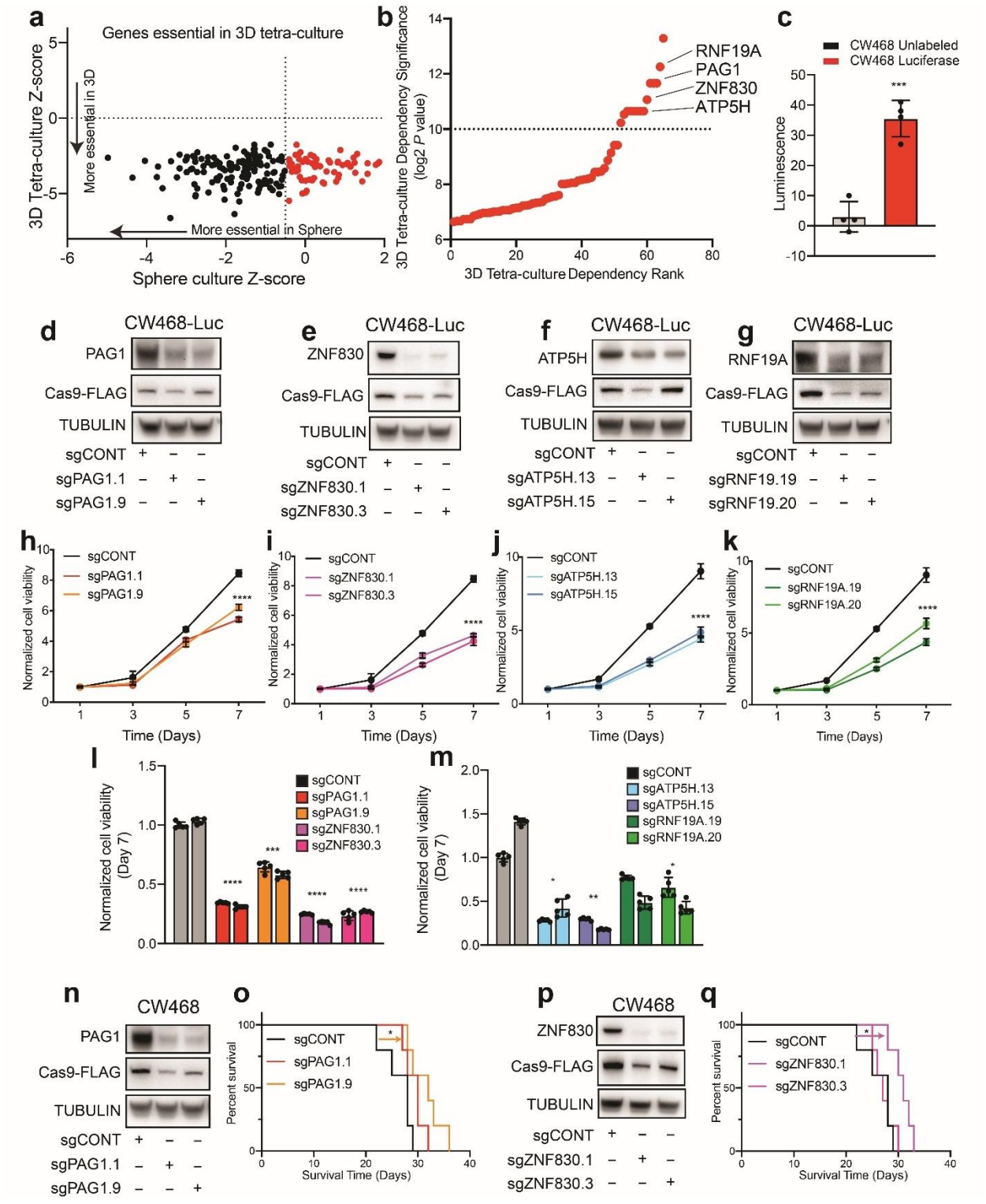

Figure 3.8 PAG1 and ZNF830 are potential therapeutic targets in glioblastoma.

Taken together, this screening approach has identified novel candidates for future investigation and potential therapeutic development.

3.3.7 3D Bioprinted Signatures Associated with Poor GBM Prognosis

To determine the clinical relevance of the 3D bioprinted system, we investigated the transcriptional profiles relative to glioblastoma patients. Signatures of genes upregulated either in intracranial orthotopic xenografts or in 3D tetra-culture compared to sphere culture were elevated in glioblastomas compared to low-grade gliomas in The Cancer Genome Atlas (TCGA), Chinese Glioma Genome Atlas (CGGA), and the Rembrandt dataset (Figures 3.9a-d). The 3D tetra-culture gene signature was elevated in recurrent glioblastomas compared to primary tumors (Figure 3.9e) and in the mesenchymal subtype compared to classical or proneural glioblastomas (Figure 3.9f). In the TCGA and CGGA datasets, the orthotopic xenograft signature and the 3D tetra-culture signature were associated with poor glioblastoma patient prognosis (Figures 3.9g-j). Many genes with individual poor prognostic significance were upregulated in the intracranial xenograft signature, including CHI3L2, POSTN, and NDRG1 (Figure 3.9k), while DENND2A, MAOB, and IGFBP2 were upregulated in the 3D bioprinted cultures (Figure 3.9l). Genes with poor prognostic significance were enriched among all genes in the 3D tetra-culture signature, when compared to a background of all genes (Figure 9m). Thus, 3D bioprinting enabled investigation of gene pathways associated with more aggressive glioblastomas, suggesting that this model can serve as a more realistic therapeutic discovery platform for the most lethal classes of glioblastoma.

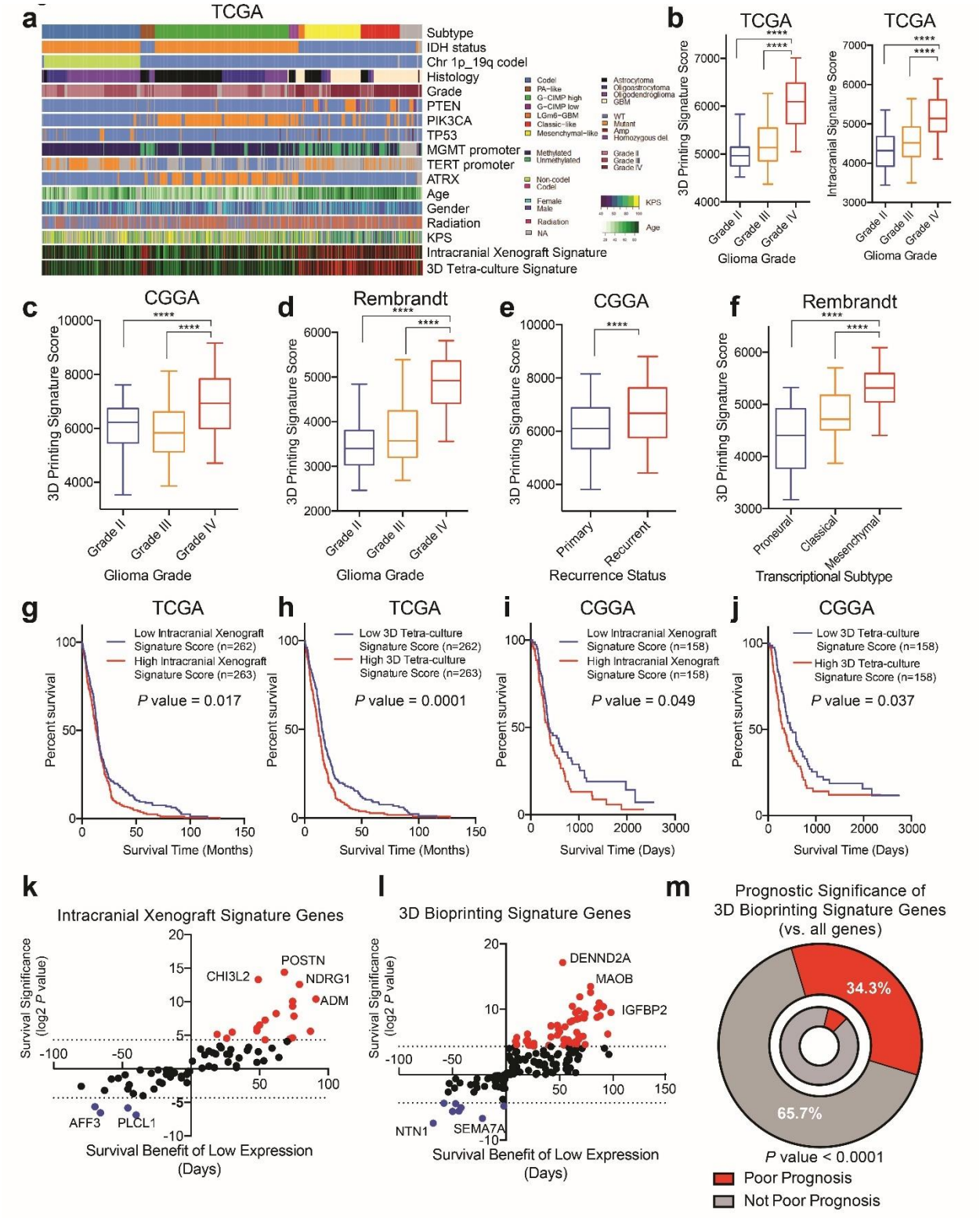

Figure 3.9 3D bioprinting contributes to upregulation of genes with poor prognostic significance in glioblastoma.

3.4 Discussion

To improve modeling of a highly lethal brain cancer for which current therapies are limited, we utilized a DLP-based 3D bioprinting system to model glioblastoma, the most common and highly lethal type of brain tumor. Studies have reported using 3D printing to create coculture models of glioblastoma cells with other stromal cells or fabricate HA-based hydrogel to mimic brain ECM.[23,24,47] However, most prior models focus on only one aspect of the in vivo situation or used non-human cells, which reduced their capacity to be applied to actual clinical settings. To the best of our knowledge, this is the first report of a human cell-based 3D glioblastoma model that recapitulates the complex tumor microenvironment with inclusion of normal brain, immune components, stromal components, and essential mechanical and biochemical cues from the extracellular matrix.

The tumor microenvironment provides essential signals to guide tumor growth and survival; however, these cues are inefficiently modeled in standard 2D culture, even in the absence of serum. Hypoxic signaling contributes to glioblastoma aggressiveness by remodeling GSC phenotypes.[48,49] Our 3D tetra-culture brain tumor model expressed hypoxia response signatures, allowing for investigation of hypoxic signaling in a physiologic environment, unlike standard cell culture systems. Critical growth factor signaling elements are provided from neurons[50-54], NPCs[55], ECM components[56,57], and immune fractions, including macrophages[58,59]. The perivascular niche provides a variety of signals including Wnts[60], ephrins[61], and osteopontins[62] to promote glioblastoma invasion, growth, and maintenance of GSCs. Future studies will be required to integrate vascular components into the 3D printed model system to further study these important components of the brain tumor microenvironment. The 3D tetra-culture tissue environment presented here enables controlled, reproducible, and scalable interrogation of these various cellular

interactions that drive brain tumor biology. While microenvironmental components supply critical niche factors to sustain the tumor ecosystem, stromal elements are also actively remodeled by malignant cells.[63] Here, we observed the role of immune cells in glioblastoma growth, including changes in gene expression, invasive behaviors, and response to treatments. Reciprocally, we also find that the 3D glioblastoma microenvironment promoted polarization of macrophages towards a protumoral M2 macrophage phenotype, highlighting this bidirectional crosstalk.

The bioprinting approach generates a spatially separated tumor region and surrounding non-neoplastic neural tissue with defined cell density which allows the cells to interact in a more realistic manner, providing a highly reproducible platform for the interrogation of cell-cell interactions with several key advantages. First, this 3D glioblastoma tissue model allows for investigation of tumor-immune interactions in a fully human species-matched system, which is not possible in xenograft or genetically engineered mouse model. This may facilitate understanding of human-specific immune interactions and advance the field of neuro-oncoimmunology by providing insights into immunotherapy efficacy. Second, combining tumoral and non-neoplastic neural components within one model will propel drug discovery efforts by enabling measurements of therapeutic efficacy, toxicities, and therapeutic index. The scalability and reproducibility of this 3D bioprinted system also allows for more high-throughput compound screening efforts. Our findings suggest that the 3D bioprinted model displays transcriptional signatures closer to patient-derived glioblastoma tissue, and that local stromal interactions present within our model promotes broad therapeutic resistance, enabling compound discovery efforts in a challenging environment. Third, the 3D bioprinted model is amenable to large-scale whole-genome CRISPR-Cas9-based screening methods to uncover novel functional dependencies in a physiologic setting. This model

extends previous approaches by characterizing context-dependent target essentiality in cancer cells and allowing for investigation of multivalent stromal cell dependencies.

In conclusion, we report a controlled, reproducible, and scalable 3D engineered glioblastoma tissue environment that serves as a more physiologically accurate brain tumor model, facilitates interrogation of the multicellular interactions that drive brain tumor biology, and acts as a platform for discovery of novel functional dependencies.

3.5 Materials and Methods

3.5.1 GelMA and GMHA synthesis and characterization

GelMA and GMHA were synthesized using Type A, gel strength 300 gelatin from porcine skin (Sigma Aldrich cat #: G2500) and 200,000 Da hyaluronic acid (Lifecore), respectively, as described previously.[64,65] Briefly, for the GelMA synthesis of 95% degree of methacrylation, 10% (w/v) gelatin was dissolved in 0.25 M 3:7 carbonate-bicarbonate buffer solution (pH ~9) at 50 °C. Methacrylic anhydride was added dropwise at a volume of 0.1 mL/(gram gelatin). The reaction was left to run for one hour at 50 °C. After synthesis, the solutions were dialyzed, frozen overnight at −80 °C, and lyophilized. Freeze-dried GelMA and GMHA were stored at −80 °C and reconstituted immediately before printing to stock solutions of 20% (w/vol) and 4% (w/vol), respectively. All materials were sterilized by syringe filters before mixing with cells (Millipore). The degree of methacrylation of GelMA and GMHA were quantified using proton NMR (Bruker, 600 MHz).

3.5.2 Cell culture

Xenografted tumors were dissociated using a papain dissociation system according to the manufacturer's instructions. GSCs were then cultured in Neurobasal medium supplemented with 2% B27, 1% L-glutamine, 1% sodium pyruvate, 1% penicillin/streptomycin, 10 ng/mL basic

human fibroblast growth factor (bFGF), and 10 ng/mL human epidermal growth factor (EGF) for at least 6 hours to recover expression of surface antigens. GSC phenotypes were validated by expression of stem cell markers (SOX2 and OLIG2) functional assays of self-renewal (serial neurosphere passage), and tumor propagation using in vivo limiting dilution.

THP-1 monocytes were cultured in RPMI 1640 (Gibco) medium supplemented with 10% heat-inactivated fetal bovine serum (FBS, Invitrogen) and 1% penicillin/streptomycin. To obtain monocyte-derived M2 macrophage, THP-1 monocytes were first seeded in 6-well plates at a density of 5 x 10^5 cells/mL (3 mL/well). Polarization to M2 macrophage was induced by (1) incubating cells in 200 ng/mL phorbol 12-myristate 13-acetate (PMA, Sigma Aldrich) for 48 hours, (2) replacing with THP1 complete medium for 24 hours, and then (3) incubating in 20 ng/mL interleukin 4 (IL4, Peprotech) and 20 ng/mL interleukin 13 (IL13, Peprotech) for 48 hours. hNP1 neural progenitor cells (Neuromics) were cultured on Matrigel coated plates using the complete NBM medium for GSCs. Human astrocytes (ThermoFisher) were cultured with astrocyte medium (ScienCell) supplemented with 1% penicillin/streptomycin.

3.5.3 3D bioprinting process

Before printing, GSCs, hNP1s, and astrocytes were digested by Accutase (Stemcell Technology), and macrophages were digested with TrypLE (ThermoFisher). For the 3D tetra-culture samples, the cell suspension solution for the tumor core consisted of 25 x 10^6 cells/mL GSCs and 12.5 x 10^6 cells/mL macrophages (GSCs:M2=2:1). For the 3D tri-culture samples, the core cell suspension solution consisted of 25 x 10^6 cells/mL GSCs only. The cell suspension solution for the peripheral region for both models consisted of 10 x 10^6 cells/mL hNP1s and 10 x 10^6 cells/mL astrocytes. All cell suspensions were aliquoted into 0.5ml Eppendorf tubes and stored on ice before use. The prepolymer solution for bioprinting was prepared with 8% (w/v) GelMA,

0.5% (w/v) GMHA, and 0.6% (w/v) lithium phenyl(2,4,6-trimethylbenzoyl)phosphinate (LAP) (Tokyo Chemical Industry). Prepolymer solution was kept at 37 °C in dark before use. Cell suspension was mixed with prepolymer solution at 1:1 ratio immediately before printing to maximize viability.

The two-step bioprinting process utilized a customized light-based 3D printing system. Components of the system included a digital micromirror device (DMD) chip (Texas Instruments), a motion controller (Newport), a light source (Hamamatsu), a printing stage, and a computer with software to coordinate all the other components. The thickness of the printed samples was precisely controlled by the motion controller and the stage. Cell-material mixture was loaded onto the printing stage, and the corresponding digital mask was input onto the DMD chip. Light was turned on for an optimized amount of exposure time (20 seconds for the core and 15 seconds for the periphery). The bioprinted 3D tri-culture/tetra-culture samples were then rinsed with DPBS and cultured in maintenance medium at 37 °C with 5% CO_2. Maintenance medium was made of 50% of complete NBM medium, 25% of THP1 medium, and 25% of astrocyte medium.

3.5.4 Human Induced Pluripotent Stem Cell (hiPSC)-derived macrophage generation

hiPSC-derived macrophages differentiation protocol was adapted from Yanagimachi et al.[66] and modified from Mesci et al.[38] Briefly, iPSCs cell lines were generated as previously described, by reprogramming fibroblast from a healthy donor.[67] The iPSC colonies were plated on Matrigel-coated (BD Biosciences) plates and maintained in mTESR media (Stem Cell Technologies). The protocol of myeloid cell lineage consisted of 4 sequential steps. In the first step, primitive streak cells were induced by BMP4 addition, which in step 2, were differentiated into hemangioblast-like hematopoietic precursors [VEGF (80 ng/ml, Peprotech), SCF (100 ng/ml, Gemini) and basic fibroblast growth factor (bFGF), (25 ng/ml, Life Technologies)]. Then, in the

third step, the hematopoietic precursors were pushed towards myeloid differentiation [FLT-3 ligand (50 ng/ml, HumanZyme), IL-3 (50 ng/ml, Gemini), SCF (50 ng/ml, Gemini), Thrombopoietin, TPO (5 ng/ml), M-CSF (50 ng/ml)] and finally into the monocytic lineage in step 4 [FLT3-ligand (50 ng/ml), M-CSF (50ng/ml), GM-CSF (25 ng/ml)]. Cells produced in suspension in step 4 were recovered, sorted by using anti-CD14 magnetic microbeads (MACS, Miltenyi) and then integrated into 3D bioprinted models as described above.

3.5.5 Isolation and generation of primary human macrophages

Human blood was obtained from healthy volunteers from the Scripps Research Institute Normal Blood Donor service. Mononuclear cells were isolated by gradient centrifugation using Lymphoprep (#07851 STEMCELL), washed with PBS, and treated with red blood cell lysis buffer. Cells were plated to adhere monocytes and cultured in 10% heat inactivated FBS in RPMI with HEPES, GlutaMAX, 1mM Sodium Pyruvate, and Pen/Strep with 50 ng/mL mCSF for 6 days as described by Ogasawara et al.[68] Unpolarized M0 macrophages were collected and integrated into 3D bioprinted models as described above.

3.5.6 Mechanical Testing

Compressive modulus of the 3D printed constructs was measured with a MicroSquisher (CellScale). Pillars with 1 mm in diameter and 1 mm in height were printed with same conditions used for the tissue models and incubated overnight at 37 °C. Both acellular and cell-encapsulated constructs were tested. The MicroSquisher utilized stainless steel beams and platens to compress the constructs at 10% displacement of their height. Customized MATLAB scripts were used to calculate the modulus from the force and displacement data collected by MicroSquisher.

3.5.7 Scanning electron microscopy (SEM)

Surface patterns of the materials and cell-material interactions on micron-scale were imaged with a scanning electron microscope (Zeiss Sigma 500). Acellular samples were snap-frozen in liquid nitrogen and immediately transferred to the freeze drier to dry overnight. Cell-encapsulated samples were dried based on a chemical dehydration protocol. Briefly, samples were fixed using 2.5% glutaraldehyde solution for 1 hour at room temperature and then overnight at 4°C. On the next day, the samples were rinsed with DPBS for three times and soaked in 70% ethanol, 90% ethanol, and 95% ethanol subsequently, each for 15 minutes. Then the solution was replaced with 100% ethanol for 10 minutes, and the step was repeated two more times. Hexamethyldisilazane (HDMS) was mixed with 100% ethanol at 1:2 ratio and 2:1 ratio. Samples were first transferred to HDMS:EtOH (1:2) for 15 minutes, then HDMS:EtOH (2:1) for 15 minutes. Then the solution was replaced with 100% HDMS for 15 minutes, and the step was repeated two more times. The samples were left uncovered in chemical hood overnight to dry. The freeze-dried or chemically dried samples were coated with iridium by a sputter coater (Emitech) prior to SEM imaging.

3.5.8 Immunofluorescence staining and image acquisition of tumor model

3D bioprinted samples and sphere cultured cells were fixed with 4% paraformaldehyde (PFA; Wako) for 30 minutes and 15 minutes, respectively, at room temperature. All samples were blocked and permeabilized using 5% (w/v) bovine serum albumin (BSA, Gemini Bio-Products) solution with 0.1% Triton X-100 (Promega) for 1 hour at room temperature on a shaker. Samples were then incubated with the respective primary antibody (listed below) overnight at 4 °C. On the next day, samples were rinsed by DPBS with 0.05% Tween 20 (PBST) for three times on the shaker. Samples were incubated with fluorophore-conjugated goat anti rabbit or goat anti mouse secondary antibodies (1:200; Biotium) and Hoechst 33342 (1:1000; Life Technologies)

counterstain in DPBS with 2% (w/v) BSA for 1 hour at room temperature in dark. After incubation, samples were rinsed three times in PBST and stored in DPBS with 0.05% sodium azide (Alfa Aesar) at 4 °C before imaging. Fluorescence images of 3D samples and their sphere cultured counterparts were taken with a confocal microscope (Leica SP8) using consistent settings for each antibody.

Fluorescence images of EGFP or mCherry labeled cells in the 3D samples were also acquired using the confocal microscope. Tile scan merging was completed by the automated program on the Leica microscope and the z-stack projection was completed by ImageJ. Quantification of the migration was based on the fluorescence images processed by ImageJ.

Table 3.1 Immunofluorescent antibodies.

Immunofluorescence Antibody	**Species**	**Dilution**	**Manufacturer**
SOX2	rabbit anti human	1:100	Abcam 97959
GFAP	mouse anti human	1:100	MilliporeSigma G3893
CA9	rabbit anti human	1:100	Novus Biologicals NB100-417
Ki67	rabbit anti human	1:100	Abcam ab16667
MAP2	mouse anti human	1:100	R&D systems MAB304
TUBB3 (TUJ1)	mouse anti human	1:100	R&D systems MAB1195
OLIG2	mouse anti-human	1:100	Millipore MABN50
EGFR (D38B1)	rabbit anti-human	1:50	Cell Signaling Technologies #4267
PhosphoEGFR Y1173	mouse anti-human	1:200	MilliporeSigma 16244

3.5.9 RNA isolation and reverse transcription-polymerase chain reaction (RT-PCR)

EGFP labeled GSCs and mCherry labeled THP1s were isolated from 3D printed tri-culture and tetra-culture samples using flow cytometry (BD FACSAria II). Cells isolated from 3D and sphere cultured cells were treated with TRIzol reagent (Life Technologies) before RNA extraction. Total RNA of each sample was extracted using Direct-zol RNA MiniPrep Kit (Zymo) and

immediately stored at −80 °C. To perform RT-PCR, cDNA was first obtained by RNA reverse transcription using the ProtoScript® First Strand cDNA Synthesis Kit (New England BioLabs) with input RNA of 200ng per sample. The primers were purchased from Integrated DNA Technologies. RT-PCR was performed using PowerUp SYBR Green master mix (Applied Biosystems) and detected with Quantstudio 3 RT-PCR system. Gene expression was determined by the threshold cycle (Ct) values normalized against the housekeeping gene.

Table 3.2 Primer sequences for RT-PCR.

Gene	**Accession Number**	**Forward Primer (5'->3')**	**Reverse Primer (5'->3')**
GAPDH	NM_002046.7	ACAACTTTGGTATCGTGGAAGG	GCCATCACGCCACAGTTTC
SOX2	NM_003106.4	TACAGCATGTCCTACTCGCAG	GAGGAAGAGGTAACCACAGGG
OLIG2	NM_005806.4	TGGCTTCAAGTCATCCTCGTC	ATGGCGATGTTGAGGTCGTG
MAP2	XM_017004138.2	CTCAGCACCGCTAACAGAGG	CATTGGCGCTTCGGACAAG
TUJ1	NM_006086.4	GGCCAAGGGTCACTACACG	GCAGTCGCAGTTTTCACACTC
CD163	NM_203416.3	AAAAAGCCACAACAGGTCGC	CTTGAGGAAACTGCAAGCCG
IL10	NM_000572.3	TACGGCGCTGTCATCGATTT	TAGAGTCGCCACCCTGATGT
IL4Ra	NM_001257406.1	GACCTGGAGCAACCCGTATC	AATCTGCCGGGTCGTTTTCA
TNFa	NM_000594.4	AGAACTCACTGGGGCCTACA	GCTCCGTGTCTCAAGGAAGT
NOS2	NM_000625.4	CGCATGACCTTGGTGTTTGG	CATAGACCTTGGGCTTGCCA
CA9	NM_001216	GGATCTACCTACTGTTGAGGCT	CATAGCGCCAATGACTCTGGT
NDRG1	NM_006096	CTCCTGCAAGAGTTTGATGTCC	TCATGCCGATGTCATGGTAGG
COL6A2	NM_058174	TACGGAGAGTGCTACAAGGTG	GGTCCTGGGAATCCAATGGG
COL1A1	NM_000088	GAGGGCCAAGACGAAGACATC	CAGATCACGTCATCGCACAAC
LOX	NM_001178102	CGGCGGAGGAAAACTGTCT	TCGGCTGGGTAAGAAATCTGA
RUNX2	NM_001015051	TGGTTACTGTCATGGCGGGTA	TCTCAGATCGTTGAACCTTGCTA
STAT6	NM_001178080	GTTCCGCCACTTGCCAATG	TGGATCTCCCCTACTCGGTG
TLR4	NM_138557	AGACCTGTCCCTGAACCCTAT	CGATGGACTTCTAAACCAGCCA
HIF3A	NM_152795	ATGCGGTCAGCAAGAGCATC	AGACGATACTCTCCGACTGGG

3.5.10 RNA sequencing and data analysis

RNA was purified as described above and subjected to RNA-sequencing. Paired-end FASTQ sequencing reads were trimmed using Trim Galore version 0.6.2 (https://www.bioinformatics.babraham.ac.uk/projects/trim_galore/) using cutadapt version 2.3. Transcript quantification was performed using Salmon[69] version 0.13.1 in the quasi-mapping mode from transcripts derived from human Gencode release 30 (GRCh38.12).[70] Salmon "quant" files were converted using Tximport[71] (https://bioconductor.org/packages/release/bioc/html/tximport.html) and differential expression analysis was performed using DESeq2[72] in the R programming language. Data from GSCs and primary glioblastoma surgical resection tissues were derived from Mack et al[37] and were processed using the same analysis pipeline. Data from matched GSCs grown in serum-free sphere culture and orthotopic intracranial xenografts were derived from Miller et al[36] and were processed using the same analysis pipeline. Processed data from matched GSCs and differentiated tumor cells were derived from Suva et al[73] and differentially expressed genes were calculated using the Limma-Voom algorithm in the Limma package[74] in the R programming language.

Principal component analysis was performed within the DESeq2 package using the top 5,000 differentially expressed genes. Uniform Manifold Approximation and Projection (UMAP) analysis was performed using the UMAPR package (https://github.com/ropenscilabs/umapr) and uwot (https://cran.r-project.org/web/packages/uwot/index.html) For comparisons of glioblastoma tissue samples with GSCs grown in standard sphere culture, analysis parameters include: sample size of local neighborhood, number of neighbors = 40; learning rate = 0.5; Initialization of low dimensional embedding = random; metrics for computation of distance in high dimensional space = manhattan. For comparisons of GSCs derived from sphere culture or 3D bioprinted models,

analysis parameters include: sample size of local neighborhood, number of neighbors = 3; Initialization of low dimensional embedding = random; metrics for computation of distance in high dimensional space = cosine.

Gene set enrichment analysis was performed using the online GSEA webportal (http://software.broadinstitute.org/gsea/msigdb/annotate.jsp) and the GSEA desktop application (http://software.broadinstitute.org/gsea/downloads.jsp) [75,76]. Pathway enrichment bubble plots were generated using the Bader Lab Enrichment Map Application [77] and Cytoscape (http://www.cytoscape.org). Glioblastoma transcriptional subtypes were calculated using a program written by Wang et al [78] and implemented in R. Gene signatures were calculated using the single sample Gene Set Enrichment Analysis Projection (ssGSEAProjection) module on GenePattern (https://cloud.genepattern.org).

3.5.11 CRISPR Editing

CRISPR editing was performed on CW468 GSCs as well as luciferase labeled CW468 GSCs (CW468-Luc). For unlabeled cells, sgRNAs were cloned into the LentiCRISPRV2 plasmid containing a puromycin selection marker (Addgene Plasmid #52961), while luciferase labeled cells were edited with sgRNAs cloned into the LentiCRISPRV2 plasmid containing a hygromycin selection marker (Addgene Plasmid #98291). sgRNA sequences were chosen from the Human CRISPR Knockout Pooled Library (Brunello)[79] and are listed here:

Table 3.3 sgRNA sequences for knockout experiment.

Gene Targeted	Guide Designation	Short Name	Forward	Reverse
Non-targeting Control	sgCONT	sgCONT	CACCGCTCTGCTGCGGAAGGATTCG	AAACCGAATCCTTCCGCAGCAGAGC
PAG1	PAG1_43495	sgPAG1.1	CACCGAACTGTGAAAGAGATCAAGG	AAACCCTTGATCTCTTTCACAGTTC
PAG1	PAG1_43498	sgPAG1.9	CACCGTGAGTTTGCTGAATATGCCT	AAACAGGCATATTCAGCAAACTCAC
ZNF830	ZNF830_55900	sgZNF830.3	CACCGTAAATCAGGAAGAATTGCGG	AAACCCGCAATTCTTCCTGATTTAC
ZNF830	ZNF830_55899	sgZNF830.1	CACCGGGAAAGGAGAGAAAACACCG	AAACCGGTGTTTTCTCTCCTTTCCC
RNF19A	RNF19A_34020	sgRNF19A.20	CACCGAATATCAAGCGAATATCATG	AAACCATGATATTCGCTTGATATTC
RNF19A	RNF19A_34019	sgRNF19A.19	CACCGAAGACACAACCCAAGCATAG	AAACCTATGCTTGGGTTGTGTCTTC
ATP5H	ATP5H_28215	sgATP5H.15	CACCGTCAGAAACATACTGACCTGG	AAACCCAGGTCAGTATGTTTCTGAC
ATP5H	ATP5H_28213	sgATP5H.13	CACCGGAATCCACCAGCTATCGACT	AAACAGTCGATAGCTGGTGGATTCC

3.5.12 Western blot analysis

Cells were collected and lysed in RIPA buffer (50 mM Tris-HCl, pH 7.5; 150 mM NaCl; 0.5% NP-40; 50 mM NaF with protease inhibitors) and incubated on ice for 30 minutes. Lysates were centrifuged at 4°C for 10 minutes at 14,000 rpm, and supernatant was collected. The Pierce BCA protein assay kit (Thermo Scientific) was utilized for determination of protein concentration. Equal amounts of protein samples were mixed with SDS Laemmli loading buffer, boiled for 10 minutes, and electrophoresed using NuPAGE Bis-Tris Gels, then transferred onto PVDF membranes. TBS-T supplemented with 5% non-fat dry milk was used for blocking for a period of 1 hour followed by blotting with primary antibodies at 4°C for 16 hours. Blots were washed 3 times for 5 minutes each with TBS-T and then incubated with appropriate secondary antibodies in

5% non-fat milk in TBS-T for 1 hour. For all western immunoblot experiments, blots were imaged using BioRad Image Lab software and subsequently processed using Adobe Illustrator to create the figures.

Table 3.4 Western blot antibodies.

Western Blot Antibody	Species	Dilution	Manufacturer
PAG1	Rabbit anti human	1:1000	Abcam ab14989
ZNF830	Rabbit anti human	1:2000	Novus Biologicals NB100-68229
ATP5H	Rabbit anti human	1:1000	Proteintech 17589-1-AP
RNF19A	Rabbit anti human	1:1000	Bethyl Laboratories A303-105A
FLAG	Mouse anti human	1:2000	Sigma F1804
Tubulin	Mouse anti-human	1:2000	Sigma T6074
EGFR (D38B1)	Rabbit anti human	1:1000	Cell Signaling Technologies #4267
Phospho-EGFR Y1173 (53A5)	Rabbit anti human	1:1000	Cell Signaling Technologies 4407
Phospho-EGFR Y1068 (D7A5)	Rabbit anti human	1:1000	Cell Signaling Technologies #3777

3.5.13 Molecular diffusion assessment

3D printed hydrogels were printed and incubated in DPBS overnight at 37°C. Fluorescein Isothiocyanate (FITC)-dextran with average molecular weight of 4,000 Da was dissolved in DPBS at concentration of 500 µg/mL. DPBS was removed and FITC-dextran solutions were added to the wells with 3D printed hydrogels. Hydrogels were incubated in FITC-dextran solution at 37 °C for 0, 5, 15, 30, 60, and 120 minutes; rinsed three times with DPBS; and then imaged using a fluorescence microscope. Fluorescence intensities of the hydrogel were measured by ImageJ. The average intensities and the spatial intensities at each time point were calculated in Excel and plotted using PRISM.

3.5.14 Drug response assessment

3D tri-culture/tetra-culture samples were printed as described above, with regular GSCs substituted with luciferase-labeled GSCs. 3D samples and sphere cultured cells plated on Matrigel coated slides were treated with drugs after 5 days in culture. Drug effects were evaluated 72 hours

later for erlotinib and gefitinib. For temozolomide, medium was replaced with fresh medium with temozolomide 72 hours after first treatment, and the drug response was evaluated 72 hours after second treatment. Luciferase readings were obtained using using the Promega luciferase assay system (E1500) based on the provided protocol and a Tecan Infinite M200 plate reader. Abiraterone (HY-70013), vemurafenib (HY-12057), and ifosfamide (HY-17419), erlotinib (HY-50896), and gefitinib (HY-50895) from MedChemExpress was used to generate dose response curves *in vitro.*

Sphere culture cell proliferation experiments were conducted by plating cells of interest at a density of 2,000 cells per well in a 96-well plate with 6 replicates. Cell Titer Glo (Promega) was used to measure cell viability. Data is presented as mean +/- standard deviation.

3.5.15 Drug sensitivity prediction

Therapeutic sensitivity and gene expression data were accessed through the Cancer Therapeutics Response Portal (https://portals.broadinstitute.org/ctrp/)[44-46]. Gene signature scores were calculated for each cell line in the dataset using the single sample Gene Set Enrichment Analysis Projection (ssGSEAProjection) module on GenePattern (https://cloud.genepattern.org). Gene signature score was then correlated with area under the curve (AUC) values for drug sensitivity for each compound tested. Correlation r-value was plotted and statistical analyses were corrected for multiple test correction.

3.5.16 CRISPR screening and data analysis

Whole genome CRISPR-Cas9 loss-of-function screening was performed with the Human CRISPR Knockout Pooled Library (Brunello)[79], which was a gift from David Root and John Doench (Addgene #73178). The library was used following the instructions on Addgene website (https://www.addgene.org/pooled-library/broadgpp-human-knockout-brunello). Briefly, the

library was stably transduced into GSCs by lentiviral infection with a multiplicity of infection (MOI) around 0.3-0.6, after puromycin selection, cells were propagated in either standard sphere cell culture conditions or in a 3D tetra-culture system. After 10 days, genomic DNA was extracted from GSCs and the sequencing library was generated using the protocol on Addgene website (https://media.addgene.org/cms/filer_public/61/16/611619f4-0926-4a07-b5c7-e286a8ecf7f5/broadgpp-sequencing-protocol.pdf). Sequencing quality control was performed using FASTQC (http://www.bioinformatics.babraham.ac.uk/projects/fastqc) and enrichment and dropout were calculated using the MAGECK-VISPR pipeline[80,81] using the MAGeCK-MLE pipeline.

3.5.17 In Vivo Tumorigenesis Assays

Intracranial xenografts experiments were generated by implanting 15,000 patient-derived GSCs (CW468) following treatment with sgRNAs targeting PAG1 or ZNF830 or a non-targeting control sgRNA (sgCONT) into the right cerebral cortex of NSG mice (NOD.Cg-Prkdcscid Il2rgtm1Wjl/SzJ, The Jackson Laboratory, Bar Harbor, ME, USA) at a depth of 3.5 mm under a University of California, San Diego Institutional Animal Care and Use Committee (IACUC) approved protocol. All murine experiments were performed under an animal protocol approved by the University of California, San Diego Institutional Animal Care and Use Committee. Healthy, wild-type male or female mice of NSG background, 4–6 weeks old, were randomly selected and used in this study for intracranial injection. Mice had not undergone prior treatment or procedures. Mice were maintained in 14 hours light/10 hours dark cycle by animal husbandry staff with no more than 5 mice per cage. Experimental animals were housed together. Housing conditions and animal status were supervised by a veterinarian. Animals were monitored until neurological signs were observed, at which point they were sacrificed. Neurological signs or signs of morbidity

included hunched posture, gait changes, lethargy and weight loss. Survival was plotted using Kaplan-Meier curves with statistical analysis using a log-rank test.

Subcutaneous xenografts were established by implanting 2 million luciferase-labeled CW468 GSCs into the right flank of NSG mice and maintained as described above. Two weeks after implantation, treatment was initiated with 80mg/kg of ifosfamide (HY-17419, MedChemExpress) dissolved in 90% safflower oil (Spectrum Laboratory Products) and 10% DMSO or vehicle alone by 100μL intraperitoneal injection once per day for 28 days. Luminescence signal was assessed at days 0, 7, 14, 21, and 28 after initiation of treatment using bioluminescence imaging following injection of luciferin reagent intraperitoneally. Tumor size was normalized based on the day 7 time point for each mouse individually.

3.5.18 Statistical analysis

Statistical analysis parameters are provided in each figure legend. Multiple group comparisons were compared by one-way ANOVA with Tukey's post-hoc analysis (by GraphPad Prism). $P < 0.05$ was designated as the threshold value for statistical significance. All data were displayed as mean values with error bars representing standard deviation.

Acknowledgements

Chapter 3, in full, is a reprint of the published article, "Three-dimensional bioprinted glioblastoma microenvironments model cellular dependencies and immune interactions", Min Tang, Qi Xie, Ryan C Gimple, Zheng Zhong, Trevor Tam, Jing Tian, Reilly L Kidwell, Qiulian Wu, Briana C Prager, Zhixin Qiu, Aaron Yu, Zhe Zhu, Pinar Mesci, Hui Jing, Jacob Schimelman, Pengrui Wang, Derrick Lee, Michael H Lorenzini, Deobrat Dixit, Linjie Zhao, Shruti Bhargava, Tyler E Miller, Xueyi Wan, Jing Tang, Bingjie Sun, Benjamin F Cravatt, Alysson R Muotri,

Shaochen Chen, Jeremy N Rich. *Cell Research*, 2020. The dissertation author was the primary investigator and author of this paper.

This work was supported by grants provided by National Institutes of Health: CA217065 (R.C.G); CA217066 (B.C.P.); DK099810 and DK114785 (B.F.K); CA197718, CA154130, CA169117, CA171652, NS087913, NS089272, NS103434 (J.N.R); CA243296 (D.L.); R01EB021857, R21AR074763, R33HD090662 (S.C.), and National Science Foundation: 1644967, 1937653 (S.C.). Dr. Muotri is supported by grants from the California Institute for Regenerative Medicine (CIRM) DISC2-09649, the National Institutes of Health through the R01MH108528, R01MH094753, R01MH109885, R01MH100175, R56MH109587, an SFARI grant #345469, and a NARSAD Independent Investigator award. We thank the UCSD School of Medicine Microscopy Core, which is supported by a NINDS P30 grant (NS047101), for use of their confocal microscopes. This material is based upon work supported by the National Science Foundation Graduate Research Fellowship Program under Grant No. DGE-1650112 (J.S.). Any opinions, findings, and conclusions or recommendations expressed in this material are those of the author(s) and do not necessarily reflect the views of the National Science Foundation. Portions of individual panels were prepared in part using images from Servier Medical Art by Servier (https://smart.servier.com/), which is licenced under a Creative Commons Attribution 3.0 Unported License (https://creativecommons.org/licenses/by/3.0/).

References

1. Polyak, K., Haviv, I. & Campbell, I. G. Co-evolution of tumor cells and their microenvironment. Trends Genet 25, 30-38, doi:10.1016/j.tig.2008.10.012 (2009).

2. McDonald, E. R., 3rd et al. Project DRIVE: A Compendium of Cancer Dependencies and Synthetic Lethal Relationships Uncovered by Large-Scale, Deep RNAi Screening. Cell 170, 577-592 e510, doi:10.1016/j.cell.2017.07.005 (2017).

3. Barretina, J. et al. The Cancer Cell Line Encyclopedia enables predictive modelling of anticancer drug sensitivity. Nature 483, 603-607, doi:10.1038/nature11003 (2012).

4. Ghandi, M. et al. Next-generation characterization of the Cancer Cell Line Encyclopedia. Nature 569, 503-508, doi:10.1038/s41586-019-1186-3 (2019).

5. Li, H. et al. The landscape of cancer cell line metabolism. Nat Med 25, 850-860, doi:10.1038/s41591-019-0404-8 (2019).

6. Hidalgo, M. et al. Patient-derived xenograft models: an emerging platform for translational cancer research. Cancer discovery 4, 998-1013, doi:10.1158/2159-8290.CD-14-0001 (2014).

7. Lancaster, M. A. & Knoblich, J. A. Organogenesis in a dish: modeling development and disease using organoid technologies. Science 345, 1247125, doi:10.1126/science.1247125 (2014).

8. Fatehullah, A., Tan, S. H. & Barker, N. Organoids as an in vitro model of human development and disease. Nat Cell Biol 18, 246-254, doi:10.1038/ncb3312 (2016).

9. Drost, J. et al. Sequential cancer mutations in cultured human intestinal stem cells. Nature 521, 43-47, doi:10.1038/nature14415 (2015).

10. Matano, M. et al. Modeling colorectal cancer using CRISPR-Cas9-mediated engineering of human intestinal organoids. Nat Med 21, 256-262, doi:10.1038/nm.3802 (2015).

11. Sachs, N. et al. A Living Biobank of Breast Cancer Organoids Captures Disease Heterogeneity. Cell 172, 373-386 e310, doi:10.1016/j.cell.2017.11.010 (2018).

12. Duarte, A. A. et al. BRCA-deficient mouse mammary tumor organoids to study cancer-drug resistance. Nat Methods 15, 134-140, doi:10.1038/nmeth.4535 (2018).

13. Broutier, L. et al. Human primary liver cancer-derived organoid cultures for disease modeling and drug screening. Nat Med 23, 1424-1435, doi:10.1038/nm.4438 (2017).

14. Huang, L. et al. Ductal pancreatic cancer modeling and drug screening using human pluripotent stem cell- and patient-derived tumor organoids. Nat Med 21, 1364-1371, doi:10.1038/nm.3973 (2015).

15. Hubert, C. G. et al. A Three-Dimensional Organoid Culture System Derived from Human Glioblastomas Recapitulates the Hypoxic Gradients and Cancer Stem Cell Heterogeneity of Tumors Found In Vivo. Cancer research 76, 2465-2477, doi:10.1158/0008-5472.CAN-15-2402 (2016).

16. Drost, J. & Clevers, H. Organoids in cancer research. Nature reviews. Cancer 18, 407-418, doi:10.1038/s41568-018-0007-6 (2018).

17. Gao, D. et al. Organoid cultures derived from patients with advanced prostate cancer. Cell 159, 176-187, doi:10.1016/j.cell.2014.08.016 (2014).

18. Linkous, A. et al. Modeling Patient-Derived Glioblastoma with Cerebral Organoids. Cell Rep 26, 3203-3211 e3205, doi:10.1016/j.celrep.2019.02.063 (2019).

19. Duval, K. et al. Modeling Physiological Events in 2D vs. 3D Cell Culture. Physiology (Bethesda) 32, 266-277, doi:10.1152/physiol.00036.2016 (2017).

20. Quail, D. F. & Joyce, J. A. The Microenvironmental Landscape of Brain Tumors. Cancer Cell 31, 326-341, doi:10.1016/j.ccell.2017.02.009 (2017).

21. Murphy, S. V. & Atala, A. 3D bioprinting of tissues and organs. Nature biotechnology 32, 773-785, doi:10.1038/nbt.2958 (2014).

22. Knowlton, S., Onal, S., Yu, C. H., Zhao, J. J. & Tasoglu, S. Bioprinting for cancer research. Trends in biotechnology 33, 504-513, doi:10.1016/j.tibtech.2015.06.007 (2015).

23. Heinrich, M. A. et al. 3D-Bioprinted Mini-Brain: A Glioblastoma Model to Study Cellular Interactions and Therapeutics. Adv Mater 31, e1806590, doi:10.1002/adma.201806590 (2019).

24. Yi, H. G. et al. A bioprinted human-glioblastoma-on-a-chip for the identification of patient-specific responses to chemoradiotherapy. Nat Biomed Eng 3, 509-519, doi:10.1038/s41551-019-0363-x (2019).

25. Kievit, F. M. et al. Chitosan-alginate 3D scaffolds as a mimic of the glioma tumor microenvironment. Biomaterials 31, 5903-5910, doi:10.1016/j.biomaterials.2010.03.062 (2010).

26. Ananthanarayanan, B., Kim, Y. & Kumar, S. Elucidating the mechanobiology of malignant brain tumors using a brain matrix-mimetic hyaluronic acid hydrogel platform. Biomaterials 32, 7913-7923, doi:10.1016/j.biomaterials.2011.07.005 (2011).

27. Xiao, W. et al. Brain-Mimetic 3D Culture Platforms Allow Investigation of Cooperative Effects of Extracellular Matrix Features on Therapeutic Resistance in Glioblastoma. Cancer research 78, 1358-1370, doi:10.1158/0008-5472.CAN-17-2429 (2018).

28. Fischbach, C. et al. Engineering tumors with 3D scaffolds. Nat Methods 4, 855-860, doi:10.1038/nmeth1085 (2007).

29. Grundy, T. J. et al. Differential response of patient-derived primary glioblastoma cells to environmental stiffness. Sci Rep 6, 23353, doi:10.1038/srep23353 (2016).

30. Ma, X. et al. 3D bioprinting of functional tissue models for personalized drug screening and in vitro disease modeling. Adv Drug Deliv Rev 132, 235-251, doi:10.1016/j.addr.2018.06.011 (2018).

31. Ma, X. et al. Rapid 3D bioprinting of decellularized extracellular matrix with regionally varied mechanical properties and biomimetic microarchitecture. Biomaterials 185, 310-321, doi:10.1016/j.biomaterials.2018.09.026 (2018).

32. Ma, X. et al. Deterministically patterned biomimetic human iPSC-derived hepatic model via rapid 3D bioprinting. Proc Natl Acad Sci U S A 113, 2206-2211, doi:10.1073/pnas.1524510113 (2016).

33. Wolf, K. J., Chen, J., Coombes, J. D., Aghi, M. K. & Kumar, S. Dissecting and rebuilding the glioblastoma microenvironment with engineered materials. Nat Rev Mater 4, 651-668, doi:10.1038/s41578-019-0135-y (2019).

34. Delpech, B. et al. Hyaluronan and hyaluronectin in the extracellular matrix of human brain tumour stroma. Eur J Cancer 29A, 1012-1017, doi:10.1016/s0959-8049(05)80214-x (1993).

35. Lee, J. et al. Tumor stem cells derived from glioblastomas cultured in bFGF and EGF more closely mirror the phenotype and genotype of primary tumors than do serum-cultured cell lines. Cancer Cell 9, 391-403, doi:10.1016/j.ccr.2006.03.030 (2006).

36. Miller, T. E. et al. Transcription elongation factors represent in vivo cancer dependencies in glioblastoma. Nature 547, 355-359, doi:10.1038/nature23000 (2017).

37. Mack, S. C. et al. Chromatin landscapes reveal developmentally encoded transcriptional states that define human glioblastoma. The Journal of experimental medicine 216, 1071-1090, doi:10.1084/jem.20190196 (2019).

38. Mesci, P. et al. Modeling neuro-immune interactions during Zika virus infection. Hum Mol Genet 27, 41-52, doi:10.1093/hmg/ddx382 (2018).

39. Muller, S. et al. Single-cell profiling of human gliomas reveals macrophage ontogeny as a basis for regional differences in macrophage activation in the tumor microenvironment. Genome Biol 18, 234, doi:10.1186/s13059-017-1362-4 (2017).

40. Venteicher, A. S. et al. Decoupling genetics, lineages, and microenvironment in IDH-mutant gliomas by single-cell RNA-seq. Science 355, doi:10.1126/science.aai8478 (2017).

41. Dreher, M. R. et al. Tumor vascular permeability, accumulation, and penetration of macromolecular drug carriers. Journal of the National Cancer Institute 98, 335-344, doi:10.1093/jnci/djj070 (2006).

42. Ostrom, Q. T. et al. CBTRUS Statistical Report: Primary Brain and Other Central Nervous System Tumors Diagnosed in the United States in 2012-2016. Neuro Oncol 21, v1-v100, doi:10.1093/neuonc/noz150 (2019).

43. Stupp, R. et al. Radiotherapy plus concomitant and adjuvant temozolomide for glioblastoma. N Engl J Med 352, 987-996, doi:10.1056/NEJMoa043330 (2005).

44. Rees, M. G. et al. Correlating chemical sensitivity and basal gene expression reveals mechanism of action. Nature chemical biology 12, 109-116, doi:10.1038/nchembio.1986 (2016).

45. Seashore-Ludlow, B. et al. Harnessing Connectivity in a Large-Scale Small-Molecule Sensitivity Dataset. Cancer discovery 5, 1210-1223, doi:10.1158/2159-8290.CD-15-0235 (2015).

46. Basu, A. et al. An interactive resource to identify cancer genetic and lineage dependencies targeted by small molecules. Cell 154, 1151-1161, doi:10.1016/j.cell.2013.08.003 (2013).

47. Pedron, S., Becka, E. & Harley, B. A. Regulation of glioma cell phenotype in 3D matrices by hyaluronic acid. Biomaterials 34, 7408-7417, doi:10.1016/j.biomaterials.2013.06.024 (2013).

48. Man, J. et al. Hypoxic Induction of Vasorin Regulates Notch1 Turnover to Maintain Glioma Stem-like Cells. Cell Stem Cell 22, 104-118 e106, doi:10.1016/j.stem.2017.10.005 (2018).

49. Lee, S. B. et al. An ID2-dependent mechanism for VHL inactivation in cancer. Nature 529, 172-177, doi:10.1038/nature16475 (2016).

50. Venkatesh, H. S. et al. Neuronal Activity Promotes Glioma Growth through Neuroligin-3 Secretion. Cell 161, 803-816, doi:10.1016/j.cell.2015.04.012 (2015).

51. Venkatesh, H. S. et al. Targeting neuronal activity-regulated neuroligin-3 dependency in high-grade glioma. Nature 549, 533-537, doi:10.1038/nature24014 (2017).

52. Venkatesh, H. S. et al. Electrical and synaptic integration of glioma into neural circuits. Nature 573, 539-545, doi:10.1038/s41586-019-1563-y (2019).

53. Venkataramani, V. et al. Glutamatergic synaptic input to glioma cells drives brain tumour progression. Nature 573, 532-538, doi:10.1038/s41586-019-1564-x (2019).

54. Zeng, Q. et al. Synaptic proximity enables NMDAR signalling to promote brain metastasis. Nature 573, 526-531, doi:10.1038/s41586-019-1576-6 (2019).

55. Qin, E. Y. et al. Neural Precursor-Derived Pleiotrophin Mediates Subventricular Zone Invasion by Glioma. Cell 170, 845-859 e819, doi:10.1016/j.cell.2017.07.016 (2017).

56. Sarkar, S. et al. Activation of NOTCH Signaling by Tenascin-C Promotes Growth of Human Brain Tumor-Initiating Cells. Cancer research 77, 3231-3243, doi:10.1158/0008-5472.CAN-16-2171 (2017).

57. Barnes, J. M. et al. A tension-mediated glycocalyx-integrin feedback loop promotes mesenchymal-like glioblastoma. Nat Cell Biol 20, 1203-1214, doi:10.1038/s41556-018-0183-3 (2018).

58. Shi, Y. et al. Tumour-associated macrophages secrete pleiotrophin to promote PTPRZ1 signalling in glioblastoma stem cells for tumour growth. Nature communications 8, 15080, doi:10.1038/ncomms15080 (2017).

59. Zhang, Y. et al. Macrophage-Associated PGK1 Phosphorylation Promotes Aerobic Glycolysis and Tumorigenesis. Mol Cell 71, 201-215 e207, doi:10.1016/j.molcel.2018.06.023 (2018).

60. Griveau, A. et al. A Glial Signature and Wnt7 Signaling Regulate Glioma-Vascular Interactions and Tumor Microenvironment. Cancer Cell 33, 874-889 e877, doi:10.1016/j.ccell.2018.03.020 (2018).

61. Krusche, B. et al. EphrinB2 drives perivascular invasion and proliferation of glioblastoma stem-like cells. eLife 5, doi:10.7554/eLife.14845 (2016).

62. Pietras, A. et al. Osteopontin-CD44 signaling in the glioma perivascular niche enhances cancer stem cell phenotypes and promotes aggressive tumor growth. Cell Stem Cell 14, 357-369, doi:10.1016/j.stem.2014.01.005 (2014).

63. Prager, B. C., Xie, Q., Bao, S. & Rich, J. N. Cancer Stem Cells: The Architects of the Tumor Ecosystem. Cell Stem Cell 24, 41-53, doi:10.1016/j.stem.2018.12.009 (2019).

64. Baier Leach, J., Bivens, K. A., Patrick, C. W., Jr. & Schmidt, C. E. Photocrosslinked hyaluronic acid hydrogels: natural, biodegradable tissue engineering scaffolds. Biotechnol Bioeng 82, 578-589, doi:10.1002/bit.10605 (2003).

65. Shirahama, H., Lee, B. H., Tan, L. P. & Cho, N. J. Precise Tuning of Facile One-Pot Gelatin Methacryloyl (GelMA) Synthesis. Sci Rep 6, 31036, doi:10.1038/srep31036 (2016).

66. Yanagimachi, M. D. et al. Robust and highly-efficient differentiation of functional monocytic cells from human pluripotent stem cells under serum- and feeder cell-free conditions. PLoS One 8, e59243, doi:10.1371/journal.pone.0059243 (2013).

67. Marchetto, M. C. et al. A model for neural development and treatment of Rett syndrome using human induced pluripotent stem cells. Cell 143, 527-539, doi:10.1016/j.cell.2010.10.016 (2010).

68. Ogasawara, D. et al. Selective blockade of the lyso-PS lipase ABHD12 stimulates immune responses in vivo. Nature chemical biology 14, 1099-1108, doi:10.1038/s41589-018-0155-8 (2018).

69. Patro, R., Duggal, G., Love, M. I., Irizarry, R. A. & Kingsford, C. Salmon provides fast and bias-aware quantification of transcript expression. Nat Methods 14, 417-419, doi:10.1038/nmeth.4197 (2017).

70. Frankish, A. et al. GENCODE reference annotation for the human and mouse genomes. Nucleic Acids Res 47, D766-D773, doi:10.1093/nar/gky955 (2019).

71. Soneson, C., Love, M. I. & Robinson, M. D. Differential analyses for RNA-seq: transcript-level estimates improve gene-level inferences. F1000Res 4, 1521, doi:10.12688/f1000research.7563.2 (2015).

72. Love, M. I., Huber, W. & Anders, S. Moderated estimation of fold change and dispersion for RNA-seq data with DESeq2. Genome Biol 15, 550, doi:10.1186/s13059-014-0550-8 (2014).

73. Suva, M. L. et al. Reconstructing and reprogramming the tumor-propagating potential of glioblastoma stem-like cells. Cell 157, 580-594, doi:10.1016/j.cell.2014.02.030 (2014).

74. Ritchie, M. E. et al. limma powers differential expression analyses for RNA-sequencing and microarray studies. Nucleic Acids Res 43, e47, doi:10.1093/nar/gkv007 (2015).

75. Subramanian, A. et al. Gene set enrichment analysis: a knowledge-based approach for interpreting genome-wide expression profiles. Proc Natl Acad Sci U S A 102, 15545-15550, doi:10.1073/pnas.0506580102 (2005).

76. Mootha, V. K. et al. PGC-1alpha-responsive genes involved in oxidative phosphorylation are coordinately downregulated in human diabetes. Nat Genet 34, 267-273, doi:10.1038/ng1180 (2003).

77. Merico, D., Isserlin, R., Stueker, O., Emili, A. & Bader, G. D. Enrichment map: a network-based method for gene-set enrichment visualization and interpretation. PLoS One 5, e13984, doi:10.1371/journal.pone.0013984 (2010).

78. Wang, Q. et al. Tumor Evolution of Glioma-Intrinsic Gene Expression Subtypes Associates with Immunological Changes in the Microenvironment. Cancer Cell 32, 42-56 e46, doi:10.1016/j.ccell.2017.06.003 (2017).

79. Doench, J. G. et al. Optimized sgRNA design to maximize activity and minimize off-target effects of CRISPR-Cas9. Nature biotechnology 34, 184-191, doi:10.1038/nbt.3437 (2016).

80. Li, W. et al. Quality control, modeling, and visualization of CRISPR screens with MAGeCK-VISPR. Genome Biol 16, 281, doi:10.1186/s13059-015-0843-6 (2015).

81. Li, W. *et al.* MAGeCK enables robust identification of essential genes from genome-scale CRISPR/Cas9 knockout screens. *Genome Biol* **15**, 554, doi:10.1186/s13059-014-0554-4 (2014).

CHAPTER 4 Investigating Drug Susceptibility and Cellular Transformations in Bioprinted Models

4.1 Abstract

TAMs are a heterogeneous population of major non-neoplastic cells in GBM known to be associated with various tumor progression events and drug responses, rendering them important therapeutic targets. TAMs originate from two distinct sources, the blood circulating myeloid cells, mainly the monocytes, and the brain-resident macrophage, the microglia. In this work, we developed a machine learning strategy to predict sensitivity of cells within the 3D bioprinted patient-derived GBM-TAM models fabricated with GBM-relevant biomaterials and matrix properties to 481 well-characterized small molecule drugs. We identified different therapeutic susceptibilities of GBM models composed of different myeloid types and validated representative drugs using the 3D models. Feature importance extracted from the machine learning models indicated important pathways related to drug sensitivity prediction. We next evaluated the microglia and monocyte's gene expression and cytokine release profiles in the 3D bioprinted GBM models and identified differential phenotypic transformation of the two myeloid cell types after 3D coculture. Microglia and monocytes both responded to the GBM microenvironment and acquired profound hypoxic signatures. Microglia-derived TAMs were more enriched in angiogenesis pathways, while monocytes-derived TAMs demonstrated increased inflammatory and cytokine activities. Microglia and monocytes exhibited similar transformation in the classic and proneural subtype GBM models, demonstrating the findings may be relatively conserved across the two subtypes.

4.2 Introduction

Glioblastoma remains the most common malignant central nervous system tumor with a patient 5-year survival of 6.8%.[1] Investigations based solely on molecular alterations driving

neoplastic events have translated into relatively limited survival advantages in clinical practice for glioblastoma (GBM), the most aggressive type of brain tumor. Tumor-associated macrophages (TAMs) originate from two distinct myeloid sources, the blood circulating monocytes and the brain-resident microglia, together forming a protumor stroma for GBM growth and progression.[2] TAMs are a heterogeneous and highly plastic population of non-neoplastic cells that account for a substantial part, ranging from 30% to 50%, of tumor mass and involved in GBM malignancy and drug resistance.[2,3] Therefore, targeting TAMs has obtained popularity as potential adjuvant intervention to improve the clinical outcomes. Different origins of the two myeloid cell types could lead to their different phenotypic transformation or consequent drug susceptibilities after being educated by the GBM microenvironment. These distinctions are yet to be investigated.

Studies on 3D models that enable crosstalk between tumor cells and stromal cells provide valuable insights into GBM cancer cell dependencies and phenotypic features of cancer cells such as growth and migration.[4,5] Transcriptional analysis results showed that 3D samples more closely resembled the patient transcriptome than traditional 2D-cultured cells, demonstrating importance of physiologically relevant 3D multicellular microenvironment. In addition, in vitro modeling also benefits from the development of tissue-relevant biomaterials and precise control of material localization and properties through advanced biofabrication technologies. The materials used to encapsulate cells not only serve as physical scaffolds for cell adherence and migration, but also provides essential biochemical cues and spatial gradient of nutrients and oxygen that further enhances the biomimicry of in vitro models.

Biofabrication techniques to construct 3D tumor models mainly include organoid self-assembly and 3D bioprinting. Cancer organoid systems including colorectal cancer, breast cancer, hepatocellular and cholangiocarcinomas, pancreatic cancers, and glioblastomas, have been

developed and employed to identify genomic alterations driving the cancer or as drug screening tools. While revealing profound insights into disease mechanisms, organoids are mainly focused on cancer cells with rare inclusion of stromal interactions. The process of self-assembly also provides limited control over material properties to mimic the ECM or cell positioning, leading to intrinsic variations among organoids. Creating clinically relevant GBM microenvironments demands precise control of the matrix properties and cellular compositions, which could be achieved with 3D bioprinting and biomaterials developed for each printing techniques. Natural material such as hyaluronic acid, gelatin, collagen, and synthetic polymers such as polyethylene-glycol diacrylate[26] and poly lactide-co-glycolide offer different biochemical and biophysical properties in favor of different tissue types. In cancer research, 3D bioprinting models have been used to investigate different events such as cellular interactions and drug sensitivities. Among different printing techniques, digital light processing (DLP)-based 3D bioprinting enables rapid fabrication of multicellular tissue models with good cell viability and high resolutions desired for mechanistic studies of multicellular models.

In this work, we developed a novel machine learning strategy to interrogate drug susceptibility of myeloid-infiltrated GBM, more specifically the microglia derived TAMs (mgTAMs), monocyte derived TAMs (moTAMs), as well as the tumor cells in the tumor. We explored the potential utility of DLP 3D bioprinted GBM models to investigate the gene expression profile and cytokine/chemokine secretion of microglia and monocyte educated by the 3D GBM microenvironment. Brain tumor-relevant biomaterials and matrix properties fostered a biomimetic microenvironment which enabled us to identify shared and distinct transformations of the two myeloid cell types in response to tumor microenvironment. To identify if the transformation was relatively conservative in all GBM or specific to a certain subtype, two GBM cell types

representing the classic and the proneural subtypes are used in the study. Several important tumor-associated pathways that were enriched in different TAMs were also the important features that contributed to the machine learning training. Potential compounds were identified for different groups, and representative drugs were validated using the 3D bioprinted patient-derived myeloid-infiltrated GBM models.

4.3 Results

4.3.1 Generation of myeloid-infiltrated GBM models and gene expression from RNAseq

We employed the DLP-based 3D bioprinting technique to develop myeloid-infiltrated GBM models with a dual molecular weight (MW) HA-based biomaterial to mimic the ECM heterogeneity of native tissues. HA serves as the primary ECM components and key regulator of glioblastoma processes.[16] While a diverse range of molecular weight of HAs are present in the brain, low molecular HA has been shown to promote GSC stemness and resistance.[33] GMHA synthesized from hyaluronic acid of 200 kDa and GelMA were used to enable the desired tissue stiffness. HA with a smaller MW range below 10 kDa, was incorporated to provide additional biochemical cues to support glioblastoma growth. We optimized the GBM model stiffness based on our previous GBM matrix property study which showed that stiffer matrix enhanced GBM stemness and drug resistance.[17]

Patient-derived classical subtype GSC CW468, proneural subtype cell line U251, human microglia cell line HMC3, and human monocyte cell line THP1 were used to generate different combination of myeloid-infiltrated models. Models were cultured 7 days in vitro to provide enough time for cells to transform inside the 3D microenvironments. For gene expression-related studies, mgTAM), moTAM, and tumor cells were isolated from the 3D models for further analysis.

4.3.2 A machine learning drug predictor generation based on 481 drugs and 636 cell lines

To identify potential drugs that could target the myeloid infiltrated tumors, we developed a machine learning workflow (**Figure 4.1**) to generate drug predictors based on two databases. We obtained drug response tabular data from the Cancer Therapeutics Response Portal (CTRP) which included 481 drugs and their corresponding drug sensitivity to 860 well characterized cancer cell lines in the form of area under curve (AUC). Each drug is trained as independent model in our workflow. Cancer Cell Line Encyclopedia (CCLE) is a database that contains 1,406 comprehensively characterized human cancer cell lines, including gene expression profiled by RNA-seq, and thus was utilized as our source of the cancer cell line gene expressions. 636 out of 860 cell lines in CTRP were fully characterized in CCLE and were selected to form our training group.

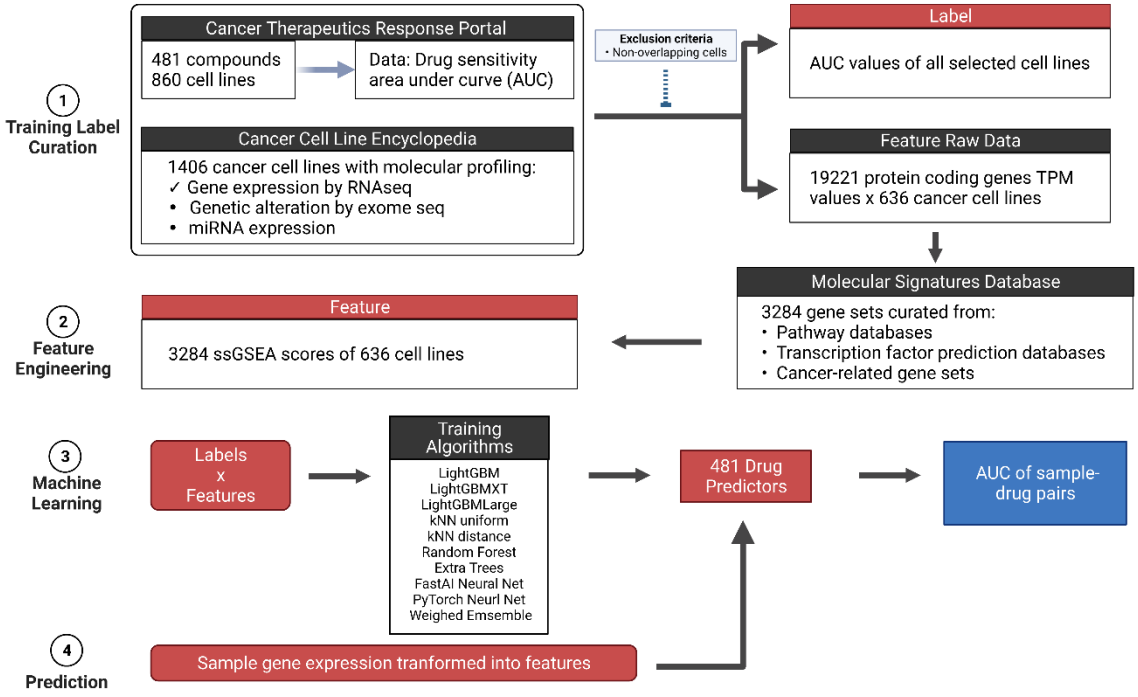

Figure 4.1 The machine learning workflow for drug response prediction based on gene expression.

To reduce batch variations in RNAseq workflow between CTRP and our experiment, which might impact the gene expression and prediction results, we generated features from the raw gene expression data based on a curated gene. Raw data from different experiment with different dimensions was flattened into the same dimensions for compatibility with machine learning training. Single-sample gene set enrichment analysis (ssGSEA) scores were generated using our formulated gene set lists which included canonical pathways, transcription factor binding sites, and oncogenic signature gene sets. The ssGSEA scores were used as the features for training, which reflected the degree of regulation of the genes within individual gene sets. The features for both training data and our sample data were further normalized and formatted to remove duplicated features before passing to the machine learning models. The AUC values for each pair of cell-drug were used as the label for this workflow. Pairs with missing labels were preprocessed to be excluded during the model training process.

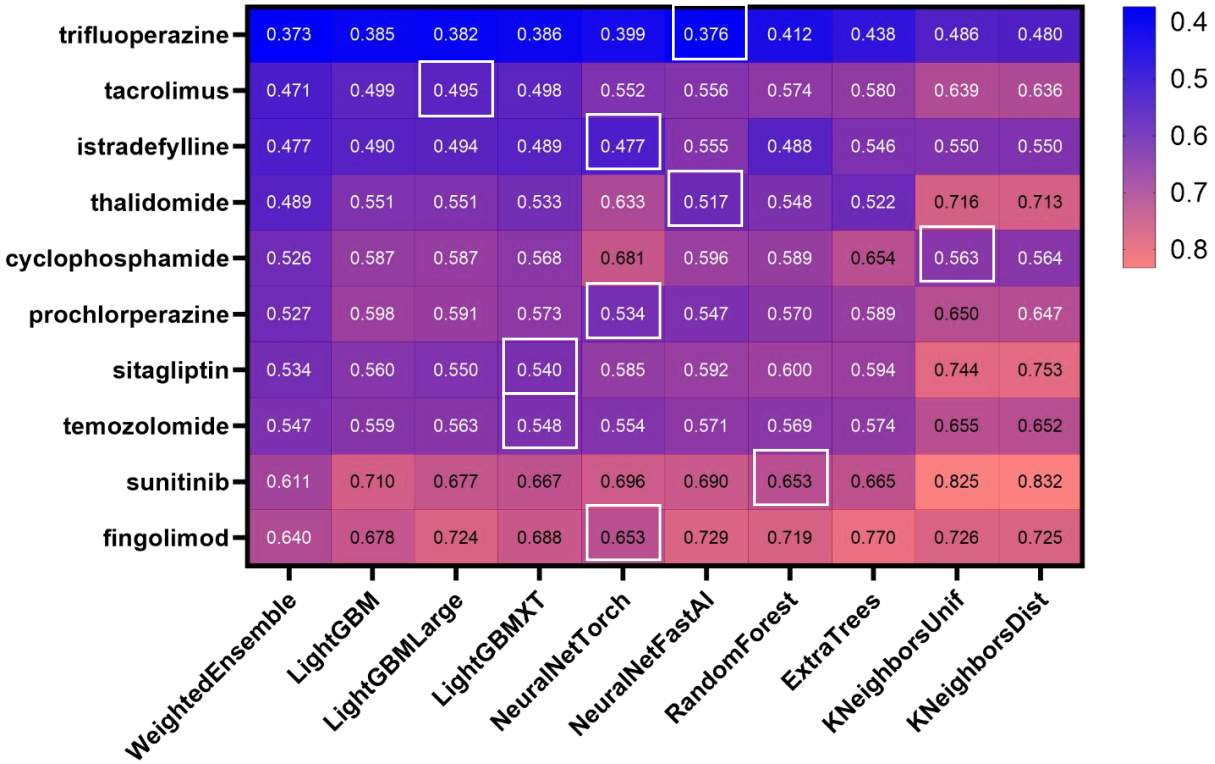

Figure 4.2 The validation score of 9 individual training algorithm and 1 weighted ensemble model for 10 drugs.

Four categories of machine learning algorithms were utilized in this study, including feature similarity K nearest neighbors (KNN), gradient-boosted decision tree (GBDT), randomized tree-based ensemble, and neural network. Specifically, 9 individual models and a weighed ensemble of all were used for training, including 2 KNN models (uniform/distance weight), 3 GBDT models (lightGBM, default/XT/large), 2 randomized trees (Random Forest, Extra Tree), and 2 neural network models (fastai, Pytorch).[6–10] Models within each categories were selected based on three criteria: accuracy, efficiency, and interpretability. For example, lightGBM algorithms were selected among the GBDT models because it could tackle the same data with only 1/20 time that traditional GBDT models will need.[6] We performed 5-fold cross-validation, specifically 5 random partitions of input data, with 3 replicates to improve predictive accuracy and reduce variation.

Each algorism-predictor pair generated a validation score based on the performance on the validation data. Drugs achieved the best scores through different models (**Figure 4.2**), indicating training them using multiple models was better than arbitrarily choosing one type of algorism. To further enhance the predictive power of the model, the output of the individual models was concatenated and trained again using stacker models. The output after this training step was weighted to maximize validation accuracy. For all 481 drug predictors, the further processed weighted ensemble model outperformed all individual models.

By extracting the features importance value of all the features for the drug predictors, we found that not all features contributed equally. We hypothesized that the most important features that contributed to the predictive power of a predictor might suggest pathways related to the mechanism of drug actions. Since TMZ is the current gold standard for GBM, we interrogated the feature importance of TMZ. The top important features of temozolomide included pathways were

related to interleukins, cytokine signaling, angiogenesis, and hypoxia. We next utilized the 3D bioprinted myeloid models to investigate the cellular transformation with a focus on these pathways.

4.3.3 Microglia activated by 3D GBM microenvironment acquired angiogenic states

Microglia infiltrated glioblastoma models were created by encapsulating microglia and GBM cells into the bioink mixture of 5% GelMA, 0.5% 200k-GMHA, and 0.25% 5k-HA. Following prior optimization for cell density,[4] the microglia GBM tissues were generated at a density of 2e7 tumor cells and 1e7 microglia/ml. Two subtypes of GBM models were constructed, CW468 representing the classical subtype and adherent GBM cell line U251 representing the proneural subtype.

To investigate how microglia responded to the 3D GBM microenvironment, RNA from mgTAM isolated from 3D GBM models cultured for 7 days and their 2D counterparts were extracted to perform RNAseq. Gene set analysis revealed that p53 pathway was highly enriched in the 3D cocultured microglia. Deregulated p53 pathway components were known to associate with GBM progression, and the accumulation of p53 could induce microglia activation with a pro-inflammatory phenotype.[18] In addition, pathways involved in GBM growth and progression, including hypoxia, angiogenesis, and interferon responses, were found to be upregulated in 3D cocultured microglia for both subtype models. Gene ontology showed that activities such as cell-cell adhesion, cytokine activities, axonogenesis, were also upregulated in 3D cocultured microglia. In the classical model, 6 hypoxia-related gene sets were enriched under a stringent false discovery rate (FDR) with q-value less than 0.5%, and an FWER-p value less than 0.05. Top hypoxic genes involved in the classical subtype included FOS, CP, SPP1, and IGFBP3, which were known to be regulated by the hypoxia-inducible factors (HIFs). Yet the transcriptional expression level of HIF genes exhibited no significant difference, with the 3D expressions slightly lower. Studies have

shown that HIF-1a could remain unaltered at mRNA level while upregulated at protein level under hypoxic conditions, and prolonged hypoxia could reduce HIF-1a at mRNA level.[19,20] Enrichment of angiogenic gene sets was also observed. Based on the leading-edge subset analysis, SPP1 gene also ranked high in the list, which had an expression level dramatically increased by 500 folds in 3D. Other proangiogenic genes, including CCND2, JAG1, STC1, VEGFA, and PDGFA were also significantly upregulated in 3D cocultured microglia.

Among all enriched pathways, hypoxia and angiogenesis genes were upregulated

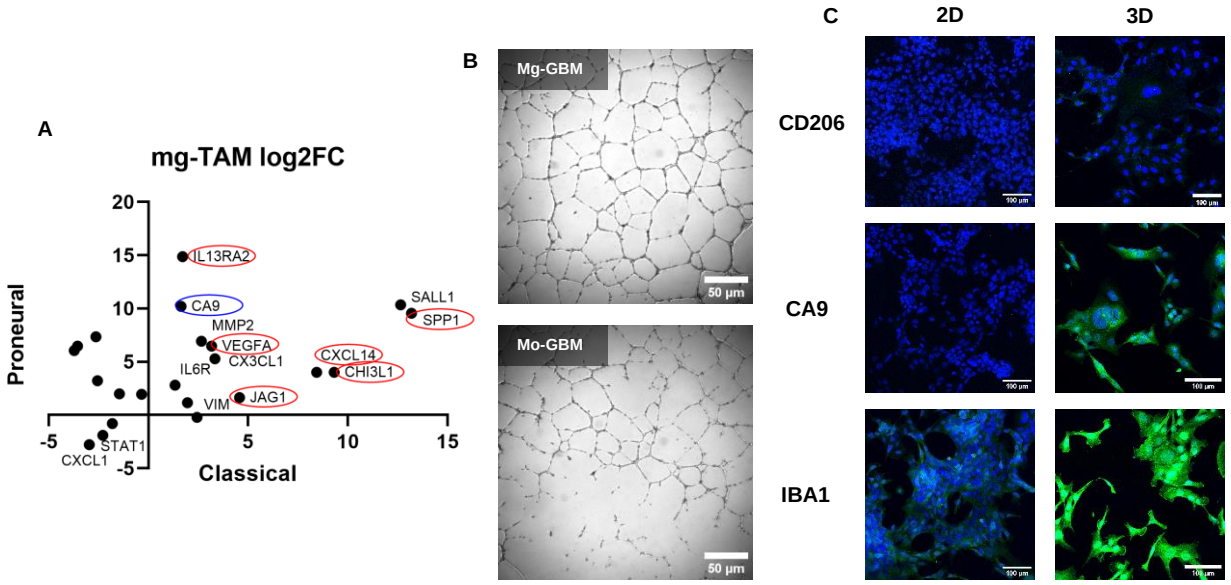

Figure 4.3 A) Representative genes upregulated and down regulated in both subtype models. Red circle: angiogenesis genes, blue circle: hypoxia gene. B) Endothelial cell cultured in supernatants collected from the 3D GBM-mgTAM or GBM-moTAM models. C) IF staining of 2D HMC3 and mgTAM in 3D models. Scale bar = 100 μm.

conservatively in both subtype models (**Figure 4.3A**). In the proneural model, the hypoxic gene CA9 showed an over 1000-fold increase. Expression of angiogenesis-related genes of the mgTAM were also significantly increased compared to 2D controls. For example, VEGFA, SPP1, and CXCL8 were increased by 89-fold, 751-fold, and 66-fold, respectively. In addition to these two categories that were similarly upregulated in the classical model, increased interferon activities were identified in 3D cocultured microglia from the proneural model. Single cell sequencing

results from clinical GBM samples have previously identified clusters of GBM-associated microglia with hypoxic and interferon-induced signatures.[3] The leading edge subset included genes such as IFI44L and SPP1 that were reported to be related to glioblastoma-associated microglia features.[21]

We generated conditioned medium using supernatants from the 3D microglia or monocyte GBM coculture to culture endothelial cells. Microglia-GBM conditioned medium supported endothelial cells to form more integral vascular networks than the monocyte-GBM conditioned medium, showing that the cytokines released by the 3D microglial models had higher angiogenic capacity (Figure 4.3B). Immunofluorescent staining of the 3D samples showed that while hypoxia marker CA9 was significantly elevated, the expression of the classic TAM marker CD206 did not differ from the 2D cultured cells (Figure 4.3C). Collectively, these results demonstrated that mgTAM in the 3D printed GBM models developed activated, hypoxic, and angiogenic features despite the molecular subtype, which could align with their prevalence in perivascular or hypoxic regions of clinical tumor samples.

4.3.4 Monocyte-derived cells exhibited TAM features and immunosuppressive signatures

Monocytes were investigated using 3D bioprinted coculture GBM models with the same material and printing parameters used for the microglia coculture models. RNAseq was performed on the moTAM isolated from the 3D coculture GBM models and their suspension-cultured control counterparts.

moTAMs showed different transformation on the mRNA level compared to the mgTAMs. Many of the shared upregulated genes in both subtype models have been found to correlate with immunosuppression in GBM and other cancer (Figure 4.4A).[22] In the classic subtype models, isolated monocytes exhibited significant enrichment of genes that were expressed by differentiated monocytes and TAMs and were associated with ECM remodeling, such as CXCL8, MMP9,

CD163, CD14, and VIM. In the proneural subtype models, hypoxia gene CA9, and immunosuppression-related genes such as CCL9, CD206, IFI44L, CD163, and CD14 were upregulated.

Hypoxia is similarly upregulated in both myeloid-GBM models, demonstrated at mRNA level and protein level. However, unlike the mgTAM were enriched in angiogenic pathways,

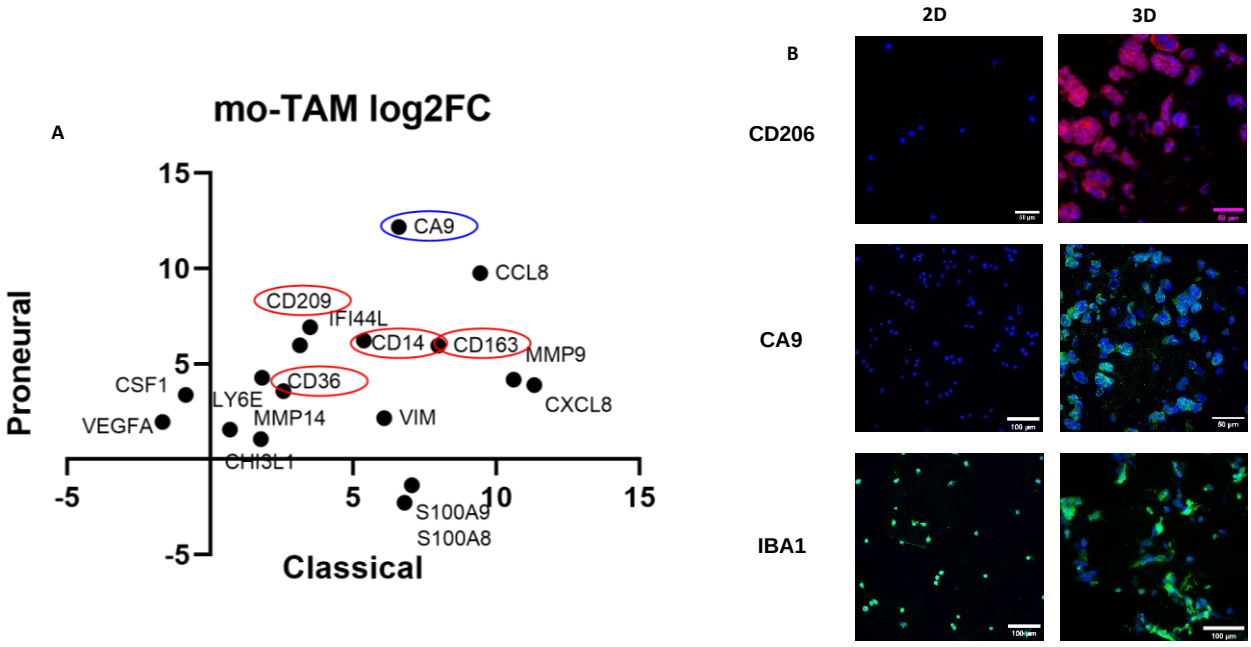

Figure 4.4 A) Representative genes upregulated and down regulated in the classical and pronerual subtype models. Red circle: TAM or monocyte differentiation genes, blue circle: hypoxia gene. C) IF staining of suspension THP1 and moTAM in 3D models. Scale bar = 100

moTAMs were more involved in the immune response related pathways including interferon activites and demonstrated upregulation of TAM and immunosuppressive signature genes. IF staining also showed the moTAM were positive for the TAM marker CD206, in contrast to the undetectable expression level of mgTAMs (Figure 4.4B). These findings suggested that the two myeloid with different origins experienced different transformations inside the 3D GBM microenvironments.

4.3.5 Microglia and monocyte-GBM models characterized by different cytokine releases

In addition to characterizing the transcription level changes of microglia and monocytes in the GBM microenvironment, we also profiled cytokines and chemokines, including 5 CC motif and 1 CXC motif chemokine ligands and 11 interleukins, released by the 3D printed myeloid-GBM tissues. Culture supernatants of printed samples were collected at 2 time points, 4 hours after the samples were printed (day 0) and day 7 after printing (**Figure 4.5**). We utilized a human 27-plex cytokine screening assay based on antibody-coated beads to detect pro-inflammatory cytokines, anti-inflammatory cytokines, and chemokine molecules that are important in cancer-immune responses.

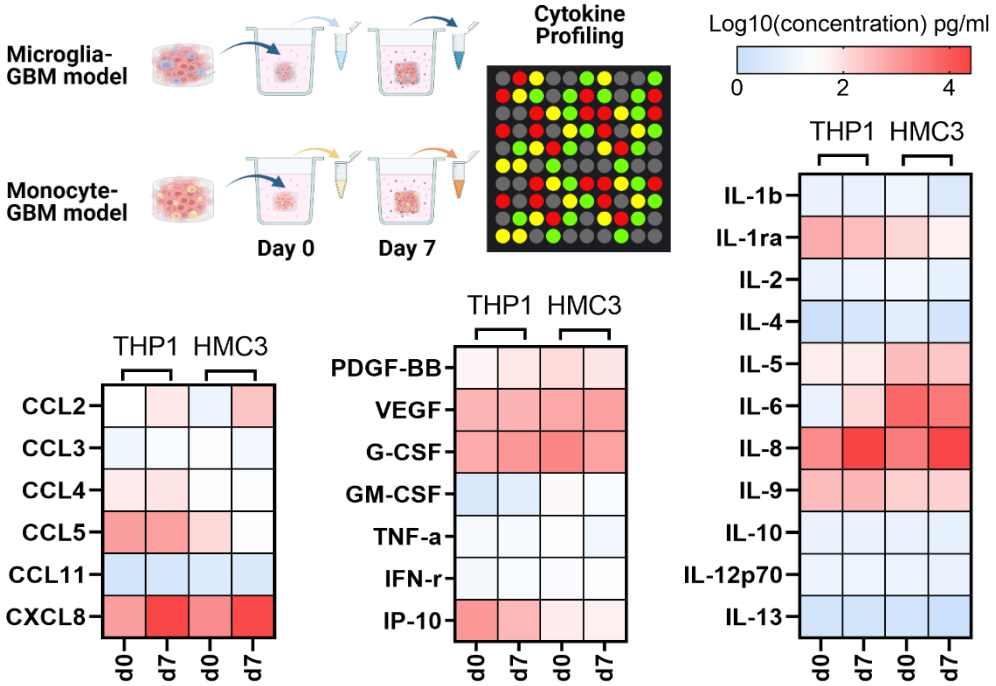

Figure 4.5 Illustration of the experiment schematics and the absolute concentrations of cytokine and chemokines measured in the supernatants.

In the microglia-GBM model, changes in secretion level of various chemokines were readily detected (**Figure 4.6A**). MCP-1 (CCL2) was significantly increased by 31 folds from 0.022 ng/ml to 0.69 ng/ml. CXCL8, also IL8, concentration was significantly increased from 3.5 ng/ml to 24 ng/ml on day 7. VEGF levels and interferon-γ (IFN-γ) levels respectively increased from 0.64 ng/ml to 0.86 ng/ml and from 0.021 ng/ml to 0.032ng/ml, consistent with the transcriptional enrichment in angiogenesis and interferon pathways. Concentrations of MIP-1b (CCL3) and RANTES (CCL5) in day 7 supernatants were reduced to 1/3 of its day 0 concentrations. G-CSF level was reduced from 2.1 ng/ml to 0.81 ng/ml. Low G-CSF (encoded by CSF3 gene) expression was shown to be related to higher inhibitory potential of myeloid cell and correlated with poorer patient prognosis.[23] All other chemokines and cytokines were measured to be slightly decreased on day 7.

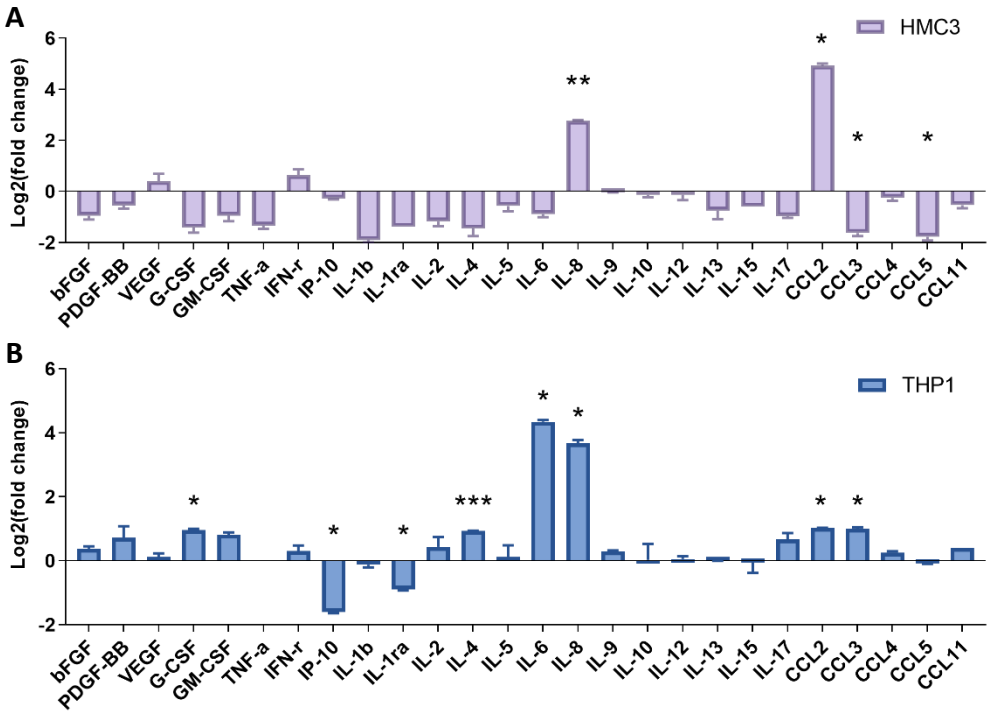

Figure 4.6 Cytokine expression changes in the A) microglia group and B) monocyte group.

In the monocyte-GBM models, chemokines including CCL2, CCL3, and CXCL8 were significantly increased by 2-fold, 2-fold, and 13-fold, respectively in day 7 supernatants (Figure 4.6B). CCL4, CCL5, and CCL11 levels remained constant. IP-10 (CXCL10) was reduced by 3-fold. In terms of cytokines, IL4 and IL6 were significantly increased by 2-fold and 20-fold, while IL1-ra was decreased to ½, exhibiting more immune responses than the microglia models. The CCL2/IL6 axis was previously found to be associated with TAM-GBM crosstalk that could promote GBM invasiveness[2]. Other cytokine levels were mostly constant between day 0 and day 7.

Different pathways regulate the chemokines and cytokines.[24] Classical activation is usually characterized by proinflammatory cytokines such as TNF-α, IL1, IL6, IL12, CXCL8, the NF-κB dependent chemokines including CCL2, 3, 4, 5 and CCL11, and the IFN-γ dependent expression of CXCL10 and CCL5. Alternative activation is usually associated with expression of IL1-ra, IL4, IL10, IL13, CCL1. While in steady state, myeloid cells are unresponsive to IL8, increasing levels of IL4 and IL13 could dramatically sensitize them to IL8 coupling.

Cytokine profiling of the two types of models also supported the different characteristics revealed by the transcriptional analysis. While the microglia model favored angiogenesis activities, the monocyte model exhibited more complex inflammatory activities.

4.3.6 Transcriptional analysis of tumor cells in the multicellular systems

Before implementing the machine learning workflow to predict drug susceptibilities, we analyzed the gene expression of the GSCs in the 3D multicellular models with microglia, monocyte, or both cell types, with the regular sphere culture served as baseline control. Principal component analysis showed that while microglia and monocyte coculture transformed the tumor cells at transcriptional level, the GSCs experienced most significant changes when both cell types were present (**Figure 4.7**).

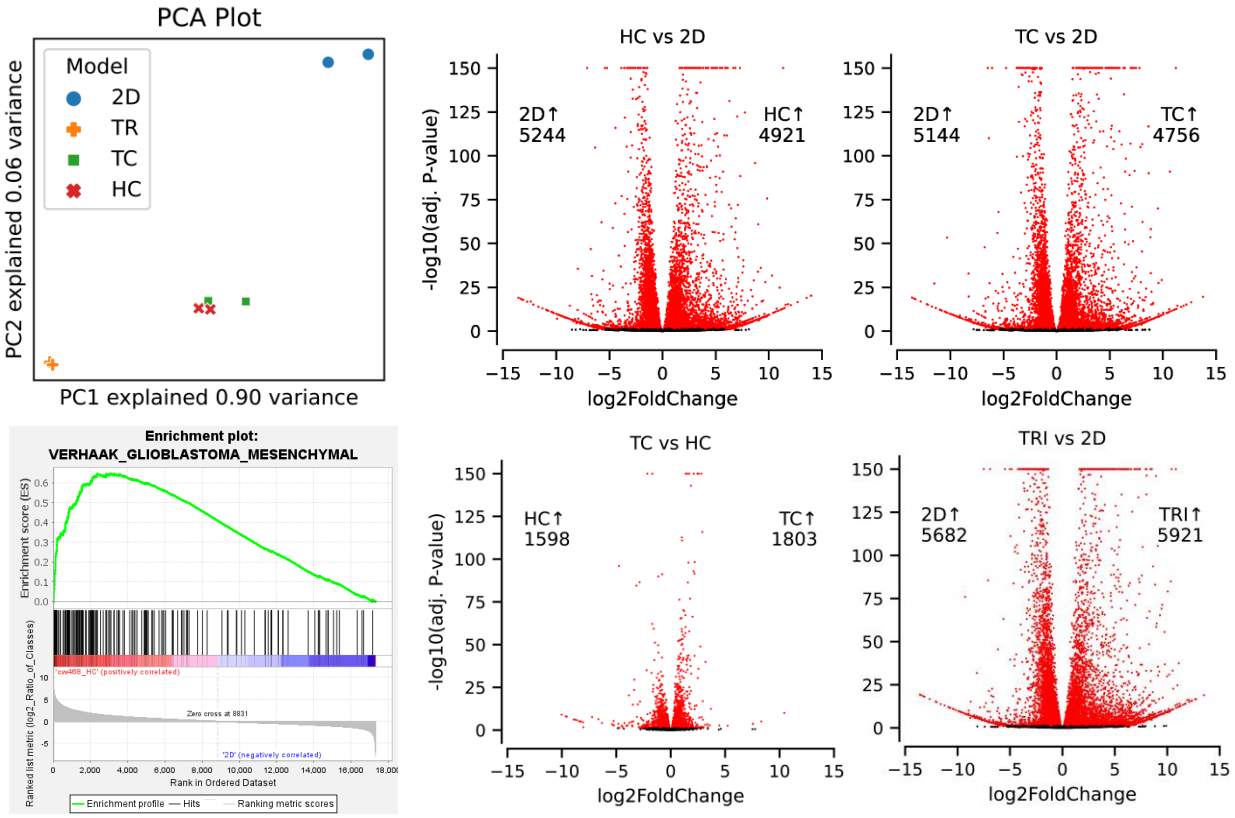

Figure 4.7 Transcriptional changes of GSCs in microglia coculture (HC), monocyte coculture (TC), and triculture (TRI) conditions.

Interestingly, the number of differentially expressed genes of GSCs isolated from the microglia and monocyte groups was relatively little compared to the other pairs. GSCs in both co-culture conditions favored mesenchymal transition and exhibited significantly enhanced hypoxic status. Specifically, various hypoxic signatures were increased, such as STC2, CSGALNACT1, SERPINE1, CAV1, FOS, ADM, ANGPLT4, SCNN1B, and S100A6 in the microglia model, and CP, SERPINE1, CAV1, HMOX1, IL6, FOS, ANGPLT4, and ADM in the monocyte models. Gene sets related to ECM remodeling and organization, as well as collagen biosynthesis, trimerization, formation, degradation, and enzyme modifications, were also upregulated in both conditions. In addition, GSCs exposed to microglia 3D coculture showed elevation of pathways associated with cancer invasiveness, cytokine activities, and integrin binding. Enriched binding activities of growth factors and ECM components including proteoglycan, fibronectin, and glycosaminoglycan

were identified. In the monocyte coculture models, GSCs are enriched in pathways involved with interferon signaling and responses, TNF-α signaling via NF-κB, IL6-STAT3 signaling, and inflammatory responses. In terms of ECM remodeling, genes that contribute to the tensile strength and ECM integrity were significantly elevated.

4.3.7 Machine learning drug sensitivity prediction and drug response validation

Gene expression data of 16 samples including GSCs, mgTAMs, and moTAMs isolated from 3D GBM models and 6 traditional cultured control samples were translated into ssGSEA scores and passed into the generated 481 drug predictors. The predictors generated an AUC value for each sample-drug pair, with low AUC corresponding to drug sensitivity and high AUC corresponding to drug resistance.

We observed that for the tumor cells, the top drug, one with the lowest AUC for the sample, had a much smaller value for traditional culture (AUC = 1.97) compared to all 3D groups. Among the 3D groups, microglia group (AUC = 5.71) and monocyte group (AUC = 5.89) had comparable values, and the triculture group with both myeloid cells demonstrated least drug sensitivity (AUC = 6.88). The prediction indicated that in general traditional cultured tumor cells had much lower drug resistance compared to 3D cultured cells, and the triculture model lead to highest drug resistance of tumor cells. Top candidates predicted by our predictors included drugs that are currently being evaluated in clinical trial, such as trametinib, suggesting promising clinical relevance of the prediction results.

We first evaluated the prediction accuracy of the predictors using traditional cultured GSCs. Several representative drugs with predicted AUC across the span, including dasatinib, lovastatin, TGX-221, and JW-55, and the gold standard drug currently used in clinical settings, TMZ, were selected. (**Figure 4.8A**). The measured IC50 values and predicted AUC showed a linear relationship, suggesting a relatively strong predictive power of the machine learning trained predictors.

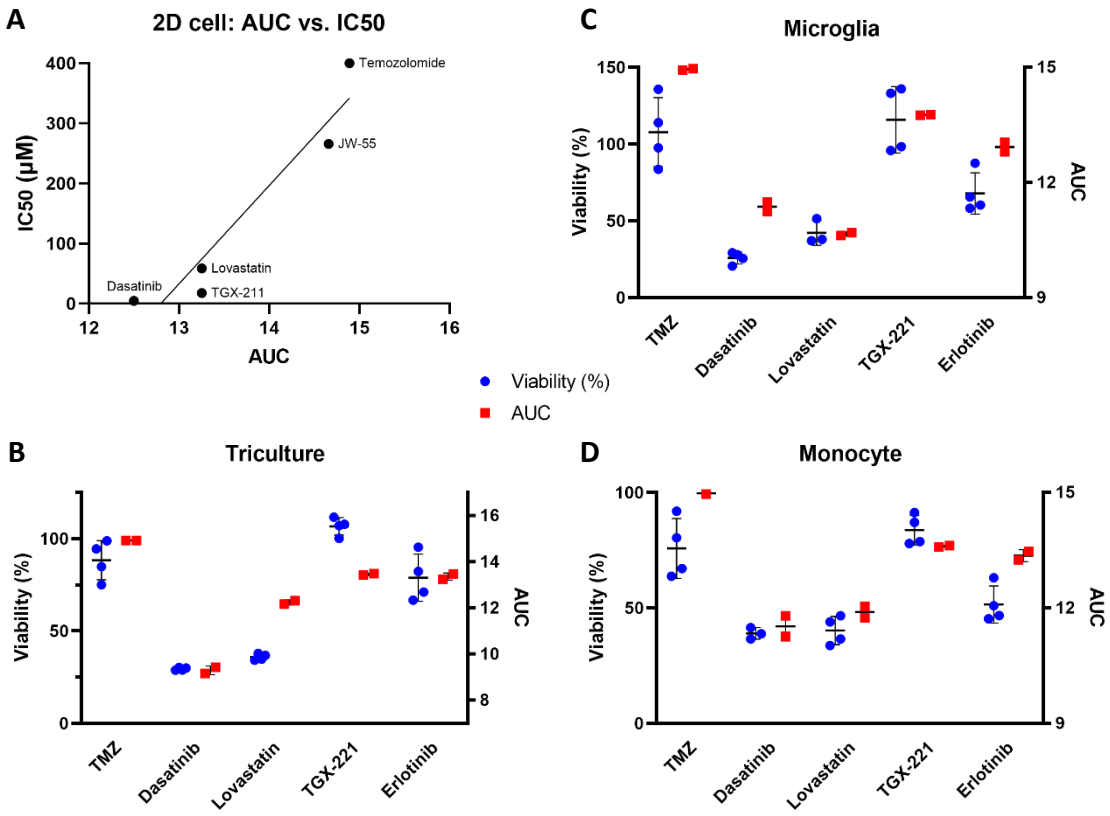

Figure 4.8 A) Drug prediction AUC and measured IC50 value of sphere cultured GSCs. B) Cell viability vs. AUC in 3D microglia-GBM models. C) Cell viability vs. AUC in 3D monocyte-GBM models. D) Cell viability vs. AUC in 3D triculture GBM models.

3D GBM models with different myeloid compositions, microglia group, monocyte group, and both-myeloid group were first generated and cultured for 3 days on shaker to allow for cell state transformation to occur. All samples were dosed with different drugs at 10 μM/ml and 100

μM/ml. Samples were collected at 72 hours of dosing to test for overall cell viability using ATP-based Celltiter-Glo assay and tumor cell viability using luciferase assay.

Dasatinib demonstrated best tumor eliminating effects, eliminating about 2/3 of the cells at 10 μM/ml and achieving complete elimination at 100 μM/ml. The viability of cells post treatment aligned relatively well with our predicted AUCs (Figure 4.8B-D). While Dasatinib failed to meet the criteria to continue in a phase II clinical trial, it demonstrated effective tumor killing effects in several other studies.[11–13] Failure to pass the blood-brain barrier (BBB) in vivo may be a critical reason of failure in clinical trials, since Dasatinib is a substrate to the efflux transporter and has been shown to have less BBB penetration or brain-plasma concentrations compared to another tyrosine kinase inhibitor.[14] Bioprinted models might better resemble the mesenchymal subtype or type II glioma subtype than the other subtypes which were less sensitive to Dasatinib treatment.[13,15]

The viability of cells after dosing by different drugs in general followed a similar trend to the predicted AUCs for corresponding pairs, validating the prediction accuracy of our machine learning generated predictors. Cells also demonstrated sensitivity to Lovastatin, but to a lesser extent compared to Dasatinib. Erlotinib and TGX-211 demonstrated mediocre responses. Cells in all our model systems exhibited strong resistance to Temozolomide and JW-55. JW-55 was predicted to be among the top sensitive drugs in our previously established correlation methods, the machine learning method developed in this work was able to predict it with relatively high AUCs (range from 14.5 to 14.9 for 3D model). The rank of this drug was among the bottom 1/3 as the relatively insensitive drugs. These findings suggest that machine learning workflow developed in this work could be a more realistic tool for drug sensitivity prediction in GBM.

4.4 Conclusions

In conclusion, we have developed an unbiased machine learning workflow that generated relatively reliable drug sensitivity prediction for both the traditional cultured cells as well as the 3D bioprinted myeloid-infiltrated GBM models. The machine learning model revealed important pathways related to the drug action which were found to be enriched in mgTAM or moTAM, including the angiogenesis pathways, immune responses, and hypoxia. The predictors were able to suggest a few potential compounds that could be effective in myeloid-infiltrated GBM.

Microglia and monocytes both exhibited activated or polarized phenotypes after cultured in the 3D GBM microenvironment. Hypoxia state was significantly increased in both myeloid models. In addition, we demonstrated that mgTAM and moTAM experience different transformation in the tumor microenvironment in both classical subtype models and proneural subtype models, suggesting the findings were conservative in these two models. Clinical outcomes may benefit from targeting the two types of myeloid cells independently during treatment.

Acknowledgements

Chapter 4, in part is currently being prepared for submission for publication. The dissertation author was the primary investigator and author of this paper.

References

1. Ostrom, Q. T., Cioffi, G., Waite, K., Kruchko, C. & Barnholtz-Sloan, J. S. CBTRUS Statistical Report: Primary Brain and Other Central Nervous System Tumors Diagnosed in the United States in 2014–2018. *Neuro-Oncol.* **23**, iii1–iii105 (2021).

2. Hambardzumyan, D., Gutmann, D. H. & Kettenmann, H. The role of microglia and macrophages in glioma maintenance and progression. *Nat. Neurosci.* **19**, 20–27 (2016).

3. Pombo Antunes, A. R. *et al.* Single-cell profiling of myeloid cells in glioblastoma across species and disease stage reveals macrophage competition and specialization. *Nat. Neurosci.* **24**, 595–610 (2021).

4. Tang, M. *et al.* Three-dimensional bioprinted glioblastoma microenvironments model cellular dependencies and immune interactions. *Cell Res.* 1–21 (2020) doi:10.1038/s41422-020-0338-1.

5. Heinrich, M. A. *et al.* 3D-Bioprinted Mini-Brain: A Glioblastoma Model to Study Cellular Interactions and Therapeutics. *Adv. Mater.* **31**, 1806590 (2019).

6. Ke, G. *et al.* LightGBM: A Highly Efficient Gradient Boosting Decision Tree. in *Advances in Neural Information Processing Systems* vol. 30 (Curran Associates, Inc., 2017).

7. Geurts, P., Ernst, D. & Wehenkel, L. Extremely randomized trees. *Mach. Learn.* **63**, 3–42 (2006).

8. Howard, J. & Gugger, S. Fastai: A Layered API for Deep Learning. *Information* **11**, 108 (2020).

9. Breiman, L. Random Forests. *Mach. Learn.* **45**, 5–32 (2001).

10. Altman, N. S. An Introduction to Kernel and Nearest-Neighbor Nonparametric Regression. *Am. Stat.* **46**, 175–185 (1992).

11. Schiff, D. & Sarkaria, J. Dasatinib in recurrent glioblastoma: failure as a teacher. *Neuro-Oncol.* **17**, 910–911 (2015).

12. National Cancer Institute (NCI). *Phase II Trial of Dasatinib in Patients With Recurrent Glioblastoma Multiforme*. https://clinicaltrials.gov/ct2/show/study/NCT00423735 (2019).

13. Wang, Z. *et al.* Cell Lineage-Based Stratification for Glioblastoma. *Cancer Cell* **38**, 366-379.e8 (2020).

14. Ravi, K. *et al.* Comparative pharmacokinetic analysis of the blood-brain barrier penetration of dasatinib and ponatinib in mice. *Leuk. Lymphoma* **62**, 1990–1994 (2021).

15. Alhalabi, O. T. *et al.* A novel patient stratification strategy to enhance the therapeutic efficacy of dasatinib in glioblastoma. *Neuro-Oncol.* **24**, 39–51 (2022).

16. Wolf, K. J., Chen, J., Coombes, J. D., Aghi, M. K. & Kumar, S. Dissecting and rebuilding the glioblastoma microenvironment with engineered materials. *Nat. Rev. Mater.* **4**, 651–668 (2019).

17. Tang, M. *et al.* Rapid 3D Bioprinting of Glioblastoma Model Mimicking Native Biophysical Heterogeneity. *Small* 2006050 (2021) doi:10.1002/smll.202006050.

18. Jayadev, S. *et al.* The Transcription Factor p53 Influences Microglial Activation Phenotype. *Glia* **59**, 1402–1413 (2011).

19. Chamboredon, S. *et al.* Hypoxia-inducible factor-1α mRNA: a new target for destabilization by tristetraprolin in endothelial cells. *Mol. Biol. Cell* **22**, 3366–3378 (2011).

20. Kallio, P. J., Pongratz, I., Gradin, K., McGuire, J. & Poellinger, L. Activation of hypoxia-inducible factor 1α: Posttranscriptional regulation and conformational change by recruitment of the Arnt transcription factor. *Proc. Natl. Acad. Sci.* **94**, 5667–5672 (1997).

21. Arrieta, V. A. *et al.* The Eclectic Nature of Glioma-Infiltrating Macrophages and Microglia. *Int. J. Mol. Sci.* **22**, 13382 (2021).

22. Han, M.-H. *et al.* High DKK3 expression related to immunosuppression was associated with poor prognosis in glioblastoma: machine learning approach. *Cancer Immunol. Immunother. CII* (2022) doi:10.1007/s00262-022-03222-4.

23. Alghamri, M. S. *et al.* G-CSF secreted by mutant IDH1 glioma stem cells abolishes myeloid cell immunosuppression and enhances the efficacy of immunotherapy. *Sci. Adv.* **7**, eabh3243 (2021).

24. Mantovani, A. *et al.* The chemokine system in diverse forms of macrophage activation and polarization. *Trends Immunol.* **25**, 677–686 (2004).

CHAPTER 5 Conclusions and Future Perspectives

5.1 Conclusions

Complex microenvironments of GBM in the aspect of extracellular matrix and cellular component have been developed using DLP-based 3D bioprinting techniques. Drug response prediction and screening methods was also developed to facilitate the drug development process.

In Chapter 2, ECM microenvironment of GBM was modeled using HA-based biomaterial to resemble the brain and GBM with tissue-matching properties. Intra-sample matrix property heterogeneity was established, and subtype-specific tumor phenotypes and gene expressions induced by local matrix stiffness was demonstrated.

In Chapter 3, multicellular glioblastoma models with the inclusion of tumor cells, immune cells, and brain stromal cells with spatial patterning was established. The 3D multicellular GBM resembled the patient transcriptome better than traditional cultured GSCs. Spontaneous cellular transformations including the tumor cells and immune cells were observed within 3D samples. Novel cellular dependencies were identified with the integration of CRISPR-Cas9 gene editing technology.

In Chapter 4, an unbiased machine learning-based drug sensitivity prediction tool to predict drug susceptibility in GBM was developed. We showed both myeloid cell types, microglia and monocyte, can be activated and transformed to TAM through cellular interactions in 3D GBM models. Different pathways enriched in microglia/monocyte-derived TAMs were identified.

The progresses on modeling GBM with 3D bioprinting and proof of concept interrogations with different techniques discussed in this thesis laid a foundation for more in-depth investigation for the fatal disease.

5.2 Future Perspectives

While progresses have been demonstrated by the 3D bioprinted GBM models, such as better resemblance to patient samples compared to traditional models, the attempts are still insufficient to fully recapitulate the complexity of GBM. Delivery of therapeutic agents to GBM tumor sites is especially challenging compared to other solid tumors due to the restricted drug and cellular transport across the unique vascular barrier of the brain, the BBB. The BBB serves as a barrier between the circulating blood and the brain parenchyma to prevent entry of blood-borne pathogens or toxic substances into CNS and to maintain CNS homeostasis.[1] The BBB excludes over 98% of small molecule drugs and tightly regulates lymphocyte extravasation, limiting accumulation of chemotherapies and effector T-cells in the GBM tissue.[2] Regulation of the BBB or circumvention of the barriers facilitates some brain tumor therapies, suggesting that the presence of a functional BBB may be essential to accurately evaluate GBM treatments.[3–5] Growing interest in repurposing FDA-approved cancer drugs with enhanced BBB penetration for GBM treatments also demonstrates the potential role of BBB in GBM therapeutic efficacy.[5]

Treatment failure in GBM result from numerous factors, including high genetic heterogeneity of GBM microenvironment, fast progression and inherent drug resistance of GBM, and insufficient delivery of therapeutic agents to the GBM sites due to the barrier properties of the BBB. The currently stagnant drug development process for GBM could be improved by reducing the attrition rate of novel compounds during clinical trials and developing drugs or treatment plans specific to different GBM subtypes. The latter requires more profound understanding of the molecular mechanisms of the GBM subtypes. High attrition rate of drugs indicate that the current preclinical models are insufficient to provide clinically relevant evaluations. For *in vivo* GBM models, lack of species-matched cellular interactions reduces their validity in predicting therapeutic outcomes in clinical trials. For *in vitro* 3D GBM models, functional BBBs have not

been reproducibly incorporated yet, and thus limiting their capacity to evaluate the penetration efficiency of compounds, which also impacts therapeutic outcomes. Advances in 3D bioprinting technologies and engineered biomaterials offer clinically relevant modeling capacity to develop integrative, biomimetic, and human-based model systems. These model systems potentially recapitulate species-matched and tissue-specific features, such as dimensionality, organization, cell-cell interactions, and cell-matrix interactions of their physiologic counterparts. 3D-bioprinted GBM models customized to recapitulate cellular and ECM microenvironments of patient tumors will help elucidate pathways involved in the GBM subtypes. Integrated GBM-BBB systems can potentially eliminate compounds that will fail the clinical trials but demonstrate success in static 2D cultures, stand-alone *in vitro* models, or animal models. Models incorporating the BBB and other stromal components of GBM into ECM-derived biomaterials will enable simultaneous evaluation of therapeutic efficacy of drugs to tumor cells, the efficiency of drug penetration across the BBB, as well as the drug toxicity to stromal cells within the tumor microenvironment. Moreover, an integrative model could recreate the non-homogeneous barrier properties of the BBB within and around the tumor tissue to mimic the native physiologic features, including compromised vessels near the necrotic tumor core and intact BBB near the invasive boundaries. The integrity of the BBB along the proliferative boundaries protects the highly invasive and stem-like GSCs from effective drug delivery. Characterization not applicable to current *in vitro* models but can potentially be considered with integrated models include: the tissue-to-blood ratio (TBR) that shows the delivery of a compound that reaches the tumor compared to the amount in blood, the brain efflux index (BEI) that shows how likely the drugs will be pumped back into the blood, and the penetration of compounds into different regions of the tumor after passing through the BBB.[6] Assessments based on an integrated GBM-BBB system will also empower optimization

strategies to bypass the BBB and enhance delivery and efficacy of novel compounds. In conclusion, 3D-bioprinted models have great potentials to facilitate mechanistic studies and clinical applications to eventually accelerate GBM therapeutic advances.

However, further advancements in bioink development and printing technologies are necessary to enable broader applications of bioprinting, despite its various advantages including versatility, precise control, biocompatibility, reproducibility, and high throughputness. Many 3D-bioprinted GBM models have been developed with alginate, gelatin, and GelMA hydrogels due to their good printibility, despite HA being the most abundant ECM component in the GBM microenvironment. It remains challenging for extrusion-based or inkjet-based bioprinting to print HA constructs with high resolution or structural integrity due to poor mechanical properties of HA. Encouragingly, DLP-based bioprinting has recently demonstrated success in fabricating an HA-rich multicellular GBM model, and many studies have showed that chemical modifications can improve the rheological properties of HA-based bioinks for printing. Development of novel bioinks or modification methods to existing biomaterials to improve their printability, including but not limited to the viscosity and the crosslinking mechanism, to accommodate bioprinting modalities will expand the material diversity for bioprinting and eventually enhance the material biomimicry of 3D models. For BBB modeling, 3D bioprinting improves the customizability and throughput of traditional microfluidic systems, and 3D-bioprinted BBB exhibits improved barrier properties. To date, the technology has mainly been used to facilitate device fabrication with cells seeded afterwards. While micron-scale structures, perfusable structures, and cell alignments have been achieved separately using bioprinting, the consolidation of these features are necessary for a successful cell-encapsulation printing of the BBB. In addition, proper molecular interventions with growth factors or small-molecule inhibitors that are often utilized in organoid development may

also be introduced to post-printing cellular constructs to facilitate desired cellular activites, such as BBB tight junction formation.

Lastly, we believe that a benchmark, including the standardized data analysis and the evaluation of model properties, should be established for 3D-bioprinted models to ensure their clinical relevance and provide guidance for future model designs. 3D models are perceived as promising alternatives to traditional 2D models and animal models, with advantages including well-defined structures and compositions, shorter time frame of production, and species-matched modeling which provides more reliable pre-clinical data. Theoretically, to include as many components as possible and assemble them in a way comparable to the native physiology can generate a structurally similar construct to the original tissue. However, whether the structural resemblance gives rise to functional resemblance requires more strict functional evaluations. Both qualitative and quantitative standards, such as percentage of matching and correlation to the clinical data, should be established for functional parameters used to evaluate the validity and the extent of clinical relevance of individual model. Examples of functional parameters are genomic and transcriptional profiles, drug responses, and specific features of each individual tissue, such as barrier properties of the BBB and invasiveness or tumorigenesis capcity of GBM. With the collective data, it may be possible and beneficial for the research community to determine the minimal components and aspects that can reliably approximate the physiological environments, thus reducing the cost and time for building a highly complex *in vitro* model.

Acknowledgements

Chapter 5, in part, is adapted from the published article, “Biomaterials and 3D Bioprinting Strategies to Model Glioblastoma and the Blood–Brain Barrier”, M. Tang, J. Rich, S. Chen.

Advanced Materials, 2020. The dissertation author was the primary investigator and author of this paper.

We thank our funding sources: CA253615 and EB021857 (to S.C.), CA197718, CA154130, CA169117, CA171652, NS087913, NS089272, and NS103434 (to J.N.R.). The authors thank Jiayi Wang for assistance on the digital illustration of tissue microenvironments.

References

1. Sarkaria, J. N. *et al.* Is the blood–brain barrier really disrupted in all glioblastomas? A critical assessment of existing clinical data. *Neuro-Oncology* **20**, 184 (2018).

2. Bhowmik, A., Khan, R. & Ghosh, M. K. Blood Brain Barrier: A Challenge for Effectual Therapy of Brain Tumors. *BioMed Research International* https://www.hindawi.com/journals/bmri/2015/320941/ (2015) doi:https://doi.org/10.1155/2015/320941.

3. Zhao, X. *et al.* Remodeling the blood-brain barrier microenvironment by natural products for brain tumor therapy. *Acta Pharm Sin B* **7**, 541–553 (2017).

4. van Tellingen, O. *et al.* Overcoming the blood–brain tumor barrier for effective glioblastoma treatment. *Drug Resistance Updates* **19**, 1–12 (2015).

5. Harder, B. G. *et al.* Developments in Blood-Brain Barrier Penetrance and Drug Repurposing for Improved Treatment of Glioblastoma. *Front Oncol* **8**, (2018).

6. Kakee, A., Terasaki, T. & Sugiyama, Y. Brain efflux index as a novel method of analyzing efflux transport at the blood-brain barrier. *J Pharmacol Exp Ther* **277**, 1550–1559 (1996).